②

Technical Report 1428
July 1991

# The Application of Canonical Eigenvalues to Two-Layer, Bounded, Underwater Acoustic Ducts

M. A. Pedersen
D. F. Gordon
F. Hosmer

**NAVAL OCEAN SYSTEMS CENTER**
**San Diego, California 92152-5000**

**J. D. FONTANA, CAPT, USN**
**Commander**

**R. T. SHEARER, Acting**
**Technical Director**

## ADMINISTRATIVE INFORMATION

The study, covered by this document, was conducted from September 1988 to April 1991 under funding from the Naval Ocean Systems Center Independent Research Program in a project entitled, "Canonical Eigenvalues in Acoustic Ducts." Melvin A. Pedersen contributed to this project as a private individual, with the exception of the work reported in appendix B. This work was carried out by Pedersen as an employee of Computer Sciences Corporation under contract to NOSC, Code 541. Appendix B is adapted from the deliverable under Contract N66001-87-D-0074, Task 92. This contract was funded under program element 63704N (NOSC 541 MA60), "Bistatic Reverberation Model," as sponsored by Code 211, Naval Oceanographic and Atmospheric Research Laboratory, Stennis Space Center, MS 39529-5004.

The present work follows up on earlier work sponsored jointly by the Office of Naval Research, Code 4250, and the Chief of Naval Material Laboratory Participation Special Focus Program in FY 1984-86.

Released by
E. F. Rynne, Head
Acoustic Analysis Branch

Under authority of
T. F. Ball, Head
Acoustic Systems and
Technology Division

MA

# SUMMARY

This report applies the method of canonical eigenvalues to double-duct propagation of underwater acoustics. The class of all two-layer bounded profiles with free- or rigid-boundary conditions is treated. The canonical eigenvalue equation contains two parameters. (The conventional approach has six parameters.) Eigenvalue solutions are presented for 23 sets of parameters and boundary conditions. These solutions can be applied to any equivalent wave problem in any discipline of physics. Physical results are presented for six sound-speed profiles. These include plots versus frequency of phase velocity, group velocity, and eigenfunction normalization coefficients. Eleven examples of eigenfunctions (standing waves) are presented. At the critical frequencies of maximum coupling between ducts, the phase velocities of adjacent modes are pinched toward each other, the group velocity and eigenvalue normalization curves for adjacent modes cross each other, and the eigenfunction amplitudes of adjacent modes strongly resemble each other. The report develops an unexpected example in which two radically different profiles have identical plots of phase and group velocity as a function of frequency. Special configurations, predicted by ray theory as degenerate, do not lead to degenerate eigenvalues. The theory is extended to treat sound-speed discontinuities and layers with different constant densities.

# CONTENTS

APPENDICES

## CONTENTS (continued)

**FIGURES**

# CONTENTS (continued)

**FIGURES (continued)**

## CONTENTS (continued)

**FIGURES (continued)**

# CONTENTS (continued)

**FIGURES (continued)**

# 1. INTRODUCTION

This report applies the general theory of canonical eigenvalues of reference 1 to the case of two-layer, bounded, underwater acoustic ducts. The general canonical eigenvalue equation is expressed in terms of two mathematical variables, x and y, and a set of profile-related parameters, $\rho_i$ and $S_{i+1}$. Reference 2 treated several simple sound-speed profile classes for which there are only one mathematical variable (x or y) and either one ($\rho_1$) or no parameters. Reference 3 treated the class of one-layer bounded ducts for which there are the two mathematical variables, x and y, and no parameters.

The canonical eigenvalue equation for the profile classes of this article contains the two mathematical variables and the two profile-related parameters $\rho_1$ and $S_2$. These classes of profile are of particular interest because they represent the simplest configuration, which exhibits the coupling characteristics of double-duct propagation. Our first extensive treatment of double ducts is presented in reference 4, which involved an eigenvalue matrix of rank nine. The canonical eigenvalue approach was developed to simplify the analysis of double-duct propagation. Thus, the present report represents our first application of the method to the problem for which it was developed.

Appendix B extends the general theory of reference 1 to include the treatment of sound-speed discontinuities at layer interfaces and the treatment of layers of different constant density. Specific computing forms are given for the two-layer profile bounded above by a free surface and below by a rigid surface. However, this theory has not been programmed as it is beyond the scope of the present effort. The number of canonical parameters increases to four, which is twice the number for continuous profiles and no treatment of density.

# 2. THEORY

This major section and the appendices contain most of the theoretical treatment of this report. The equations, which follow directly from the application of reference 1 to the profile class of figure 1, represent a minor part of the treatment. The equations necessary to generate the numerical examples of this report are presented as well as the analysis thereof. Some of this theory may appear arcane on first exposure. However, it will become clearer when examined later in the context of the relevant numerical examples as presented in section 3.

## A. PROFILE REPRESENTATION

The sound-speed profile consists of two layers. The sound speed in each of these layers is expressed as

$$[C_i/C(Z)]^2 = 1 - 2\gamma_i(Z - Z_i)/C_i \tag{1}$$

where $C_i$, $Z_i$, and $\gamma_1$ are the sound speed, depth, and sound-speed gradient, respectively at the top of layer *i*.

A TWO-LAYER, BOUNDED, CANONICAL PROFILE

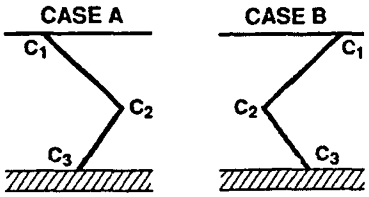

Figure 1. Schematic of the profile class.

Figure 1 presents a schematic of the profile class. The profile class is characterized by two parameters, $\rho_1$ and $S_2$, related to the parameters of eq. 1 by

$$\rho_i = (-\gamma_{10}/\gamma_2)^{1/3} \tag{2}$$

and

$$S_2 = [(C_1/C_3)^2 - 1]/[(C_1/C_2)^2 - 1] \ . \tag{3}$$

Here, $C_1$ is the surface sound speed, $C_2$ is the sound speed at the interface between the two layers, and $C_3$ is the bottom sound speed. In eq. 2, $\gamma_2$ is the gradient at the top of layer 2; whereas $\gamma_{10}$ is the gradient at the bottom of layer 1 as given by

$$\gamma_{10} = C_2{}^3\gamma_1/C_1{}^3 \tag{4}$$

where $\gamma_1$ is the gradient at the surface.

As demonstrated in reference 1, the parameterization of eqs. 2 and 3 is uniquely determined by the condition that the frequency and the phase velocity do not appear in the canonical eigenvalue equation.

The sound-speed profile is completely determined by give profile parameters. These are $C_1$, $C_2$, $C_3$, $\gamma_1$, and $\gamma_2$. However, the customary eigenvalue equation usually replaces $\gamma_2$ by the dimensionless parameter $\rho_1$. Here, $\gamma_2$ can be related to $\rho_1$, $C_1$, $C_2$, and $\gamma_1$ through eqs. 2 and 4.

In the canonical eigenvalue approach, the eigenvalue solutions are obtained for a fixed pair of values of the parameters $\rho$ and S. (From this point on we will drop the subscripts on $\rho_1$ and $S_2$ to simplify the notation). Each point in the $\rho$, S plane represents a different profile class. To translate the canonical eigenvalues from mathematical space to physical space, we must specify a particular sound-speed profile of the class. Here, we are at liberty to select $C_1$, $C_2$, and $\gamma_1$. The parameter $C_3$ may then be determined from

$$C_3 = C_1\{[(C_1/C_2)^2 - 1]S + 1\}^{-1/2} . \tag{5}$$

Thus, the profile is completely specified by the three selected parameters, eq. 5, and $\rho$.

Cases A and case B are distinguished in figure 1, because the canonical eigenvalue equation yields two sets of modes. The set of modes corresponding to case A are of most interest because they exhibit the coupling between double ducts. For case A, $\gamma_1$ is positive and $C_2$ is greater than $C_1$. The set of modes corresponding to case B does not exhibit any coupling phenomenon. For case B, $\gamma_1$ is negative and $C_2$ is smaller than $C_1$.

Next we examine $\rho$ and S in the context of figure 1. Our interest is this article is limited to the base of $\rho$ positive. This means that the gradient of the two layers has opposite signs. If $\rho$ is negative, then there is no double-duct configuration, because $C_3$ of case A is larger than $C_2$.

Next, consider the allowable range of values on S for which there are double ducts in case A. When $C_1 = C_3$, $S = 0$. When $C_2 = C_3$, $S = 1$. When $C_3 = 0$, $S_2 = -\infty$. Our primary interest is in $0 \leq S \leq 1$ for which $C_1 \leq C_3 \leq C_2$ and in modestly negative values of S for which $C_3$ is somewhat less than $C_1$.

We examined alternative representations for S in terms of $Z_1$ and $Z_2$, where $Z_1$ and $Z_2$ is the thickness of layers 1 and 2 respectively. We obtained

$$S = (C_2/C_3)^2\,(1 - \rho^{-3} Z_2/Z_1) . \tag{6}$$

This does not appear a particularly useful, with the exception of the case where S = 0. Here, eq. 6 reduces to

$$Z_2 = \rho^3 Z_1 \, . \tag{7}$$

Our main interest is in the free surface, rigid-bottom boundary condition in figure 1. However, we shall also consider free-free and rigid-rigid boundary conditions as they illustrate certain features of interest in the solution. (We need not consider the rigid-free boundary condition because this can be obtained by inverting the free-rigid condition.) We note that the analysis of the sound-speed profile presented here applies equally well to all boundary conditions. The boundary conditions determine the particular form of the eigenvalue equation, but have nothing to do with the parameters ρ and *S* and their relation to the profile parameters.

## B. CANONICAL EIGENVALUE FORMULATION

First, consider the eigenvalue formulation for the free-rigid boundary condition. The eigenvalue equation may be expressed as

$$\begin{vmatrix} Ai(-\zeta_{11}) & Bi(-\zeta_{11}) & 0 & 0 \\ Ai(-\zeta_{10}) & Bi(-\zeta_{10}) & -Ai(-\rho^2\zeta_{10}) & -Bi(-\rho^2\zeta_{10}) \\ \rho Ai'(-\zeta_{10}) & \rho Bi'(-\zeta_{10}) & Ai'(-\rho^2\zeta_{10}) & Bi'(-\rho^2\zeta_{10}) \\ 0 & 0 & Ai'(-\zeta_{20}) & Bi'(-\zeta_{20}) \end{vmatrix} = 0 \, . \tag{8}$$

Rows 1 to 4 of the matrix follow respectively from eqs. 23, 18, 22, and 24 of reference 2.

We now consider the transformations into the canonical variables of reference 1 given by

$$\zeta_{11} = x \tag{9}$$

and

$$\zeta_{10} = y \, . \tag{10}$$

One of the canonical parameters is ρ. The other, S, enters the eigenvalue equation through

$$\zeta_{20} = \rho^2(1 - S)x + \rho^2 Sy \tag{11}$$

which follows from eqs. 32 and 37 of reference 1.

Next, we introduce various sets of equations that facilitate the expansion of the matrix of eq. 8 and its solution by Newton's method. Certain combinations of Airy functions associated withe the interface between layers 1 and 2 are common to the solution for any combination of boundary conditions. We define these combinations as $G_1$ to $G_4$ where

$$G_1 = \mathrm{Ai}(-y)\mathrm{Ai}'(-\rho^2 y) + \rho \mathrm{Ai}'(-y)\mathrm{Ai}(-\rho^2 y) \tag{12}$$

$$G_2 = \mathrm{Bi}(-y)\mathrm{Ai}'(-\rho^2 y) + \rho \mathrm{Bi}'(-y)\mathrm{Ai}(-\rho^2 y) \tag{13}$$

$$G_3 = \mathrm{Ai}(-y)\mathrm{Bi}'(-\rho^2 y) + \rho \mathrm{Ai}'(-y)\mathrm{Bi}(-\rho^2 y) \tag{14}$$

and

$$G_4 = \mathrm{Bi}(-y)\mathrm{Bi}'(-\rho^2 y) + \rho \mathrm{Bi}'(-y)\mathrm{Bi}(-\rho^2 y)\ . \tag{15}$$

We shall also need the derivative of these functions with respect to *y*, holding ρ fixed. These derivations are

$$G_1' = -(1+\rho^3)[\mathrm{Ai}'(-y)\mathrm{Ai}'(-\rho^2 y) - \rho y\, \mathrm{Ai}(-y)\mathrm{Ai}(-\rho^2 y)] \tag{16}$$

$$G_2' = -(1+\rho^3)[\mathrm{Bi}'(-y)\mathrm{Ai}'(-\rho^2 y) - \rho y\, \mathrm{Bi}(-y)\mathrm{Ai}(-\rho^2 y)] \tag{17}$$

$$G_3' = -(1+\rho^3)[\mathrm{Ai}'(-y)\mathrm{Bi}'(-\rho^2 y) - \rho y\, \mathrm{Ai}(-y)\mathrm{Bi}(-\rho^2 y)] \tag{18}$$

and

$$G_4' = -(1+\rho^3)[\mathrm{Bi}'(-y)\mathrm{Bi}'(-\rho^2 y) - \rho y\, \mathrm{Bi}(-y)\mathrm{Bi}(-\rho^2 y)]\ . \tag{19}$$

We note in passing the $G_1$ and $G_1'$ appear in eqs. 79 and 84 of reference 2 as the solution to the unbounded refractive duct. Moreover, $G_2$ appears in eq. 105 of reference 2 as part of the the canonical eigenvalue equation for a refractive duct bounded above by a free surface.

Next, we define certain combinations of $G_1$ to $G_4$ as given by

$$G_{11} = \mathrm{Bi}'(-\zeta_{20})\, G_2 - \mathrm{Ai}'(-\zeta_{20})\, G_4 \tag{20}$$

$$G_{12} = \mathrm{Bi}'(-\zeta_{20})\, G_1 - \mathrm{Ai}'(-\zeta_{20})\, G_3 \tag{21}$$

$$G_{13} = \mathrm{Bi}(-\zeta_{20})\, G_2 - \mathrm{Ai}(-\zeta_{20})\, G_4 \tag{22}$$

and

$$G_{14} = \mathrm{Bi}(-\zeta_{20})\, G_2 - \mathrm{Ai}(-\zeta_{20})\, G_4\ . \tag{23}$$

We note that $\zeta_{20}$ is given in terms of x and y by eq. 11. However, we retain the use of $\zeta_{20}$ here to simplify the manner of writing the expressions.

Next, we define certain combination of $G_{11}$ to $G_{14}$ as given by

$$G_{15} = Ai(-x)\ G_{11} - Bi(-x)\ G_{12} \tag{24}$$

$$G_{16} = Ai'(-x)\ G_{11} - Bi'(-x)\ G_{12} \tag{25}$$

$$G_{17} = Ai(-x)\ G_{13} - Bi(-x)\ G_{14} \tag{26}$$

and

$$G_{18} = Ai'(-x)\ G_{13} - Bi'(-x)\ G_{14}\ . \tag{27}$$

We also require the quantities $G_{15}'$, $G_{16}'$, and $G_{17}'$, which are defined respectively as $G_{15}$, $G_{16}$, and $G_{17}$ with $G_1$, $G_2$, $G_3$, and $G_4$ replaced respectively by $G_1'$, $G_2'$, $G_3'$, and $G_4'$.

We are now ready to present the eigenvalue equation and other expressions used in the solution. The canonical eigenvalue equation for the free-rigid boundary is given by

$$G_{15} = 0\ . \tag{28}$$

Equation 28 can be obtained by expanding the matrix of eq. 8 by the elements of the first row. Equation 28 is solved by Newton's method similar to that used in reference 3 for one-layer bounded ducts. This method requires one of the two derivatives

$$\delta\, G_{15}/\delta\, x = -G_{16} + \zeta_{20}\rho^2(1 - S)\ G_{17} \tag{29}$$

or

$$\delta\, G_{15}/\delta\, y = -G'_{15} + \zeta_{20}\rho^2\ S\ G_{17}\ . \tag{30}$$

Item $G_{16}$ arises from the Airy function with a $-x$ argument. Item $G'_{15}$ arises from the Airy functions with a $-y$ or $-\rho^2 y$ argument. Item $G_{17}$ arises from the Airy function with a $-\zeta_{20}$ argument. One solves eq. 28 by either selecting a fixed value of y and iterating to determine x by eq. 29 or by selecting a fixed value of x and iterating to determine y by eq. 30.

Next, consider the free-free boundary condition. For this case, the Airy function derivatives of row 4 of eq. 8 are replaced by the Airy functions. The eigenvalue equation is given by

$$G_{17} = 0\ . \tag{31}$$

with derivatives given by

$$\delta G_{17}/\delta x = -G_{18} - \rho^2(1-S)\, G_{15} \tag{32}$$

and

$$\delta G_{17}/\delta y = -G_{17}' - \rho^2\, S\, G_{15}\ . \tag{33}$$

In the case of the rigid-rigid boundary condition, the Airy functions of row 1 of eq. 8 are replaced by the Airy function derivatives. The eigenvalue equation is given by

$$G_{16} = 0\ . \tag{34}$$

with derivatives given by

$$\delta G_{16}/\delta x = -G_{15} + \zeta_{20}\, \rho^2(1-S)\, G_{18} \tag{35}$$

and

$$\delta G_{16}/\delta y = -G'_{16} + \zeta_{20}\rho^2\, S\, G_{18}\ . \tag{36}$$

We note that it is relatively easy to include the other boundary conditions in the analysis for $G_{17}$ and $G_{16}$, the eigenvalue expressions for the free-free and rigid-rigid conditions are also required in eq. 29 for use in solving eq. 28 for the free-rigid condition. Our computer implementation consists of implementing eqs. 12 to 27 in a general program and using them as needed in eqs. 28 to 30 or their other boundary condition counterparts.

## C. ASYMPTOTIC SOLUTIONS

This section is concerned with the eigenvalue solutions for infinite negative y or infinite negative x.

First, we consider the behavior for large negative values of y. For all three boundary conditions, the dominant term is $G_4$ of eq. 15 because it contains products of Airy functions, both factors of which become infinite. If we now divide the eigenvalue equation through by $G_4$, all of the terms will go to zero except the one that contained $G_4$ before the division. It follows then, that the eigenvalue can be reduced to

$$\mathrm{Ai}(-x)\ \mathrm{Ai}'(-\zeta_{20}) = 0 \tag{37}$$

$$\mathrm{Ai}(-x)\ \mathrm{Ai}(-\zeta_{20}) = 0 \tag{38}$$

and

$$\mathrm{Ai}'(-x)\,\mathrm{Ai}'(-\zeta_{20}) = 0 \tag{39}$$

for the free-rigid, free-free, and rigid-rigid conditions respectively.

Let the negatives of the zeroes of Ai and Ai′ be given by $a_n$ and $a'_n$. These zeroes are tabulated in reference 5. In the case of a free surface, there are vertical asymptotes in an x,y plot at $y = -\infty$ for

$$x = a_n\ . \tag{40}$$

In the case of a rigid surface, there are vertical asymptotes at $y = -\infty$ for

$$x = a'_n\ . \tag{41}$$

In the case of a rigid bottom, the variable y is asymptotic to the lines

$$y = (1 - S^{-1})x + a'_n/\rho^2 S,\ \ S \neq 0\ . \tag{42}$$

In the case of $S = 0$, there are vertical asymptotes for

$$x = a'_n/\rho^2\ . \tag{43}$$

In the case of a free bottom, the counterparts of eqs. 42 and 43 are

$$y = (1 - S^{-1})x + a_n/\rho^2 S,\ \ S \neq 0 \tag{44}$$

and

$$x = a_n/\rho^2\ . \tag{45}$$

As will be demonstrated in section 3, the curves with negative values of y correspond to the case A modes of figure 1. The asymptotic solutions of eqs. 40 to 45 are of particular importance because they provide a first approximation to the critical frequencies of double-duct propagation. The asymptotic solutions are also important as a starting point for the iterative solutions of the eigenvalue equation.

Next, consider the behavior for large negative values of x. In the case of eq. 28, the dominant term is $-\mathrm{Bi}(-x)\,\mathrm{Bi}'(-\zeta_{20})\,G_1$. Here, the first two factors both become infinite when $S<1$. If we divide the eigenvalue equation by these factors, all terms go to zero with the exception of $G_1$. Thus, here there are horizontal asymptotes at $x = -\infty$ for the values of y which satisfy

$$G_1 = 0 \,. \tag{46}$$

Table 3 and figure 6 of reference 2 gives the solutions of y as a function of ρ. If we examine the other boundary conditions, we find that the dominant term is again $G_1$ multiplied by a product of Bi or Bi′. The result is that eq. 46 applies to all of the boundary conditions.

We note that x equal to minus infinity corresponds to infinite frequency for the case B modes of figure 1. We also note that eq. 46 is identical to the solution for an unbounded refractive duct as given by eq. 79 of reference 2. At sufficiently high frequencies, the solution for case B of figure 1 is independent of the boundary conditions and approaches the solution for the unbounded refractive duct as a limit.

## D. LATTICE POINTS

In the case of the ducts of reference 3, certain finite roots of the eigenvalue equation could be related to the zeros of the various Airy functions. These zeros formed sets of lattice points through which the eigenvalue curves pass. Next, we examine the possibility for our two-layer ducts. First, consider the case of $S = 0$ and $\rho = 1$. For these values, eq. 31, for the free-free boundary, is satisfied if both Ai(−x) and $G_1(y) = 0$. Thus, here the eigenvalue curves go through the lattice points given by

$$x = a_n; \;\; y = a_m \text{ or } y = a'_m \,. \tag{47}$$

This notation means that the zero Ai(−y) or Ai′(−y) can be of a different order than that of Ai(−x).

We note that Ai(−x) and Ai(−y) or Ai′(−y) also go to zero at x or $y = -\infty$. Thus, these points at infinity are also lattice points of eq. 47. They take the form of horizontal asymptotes for $x \to -\infty$ and vertical asymptotes for $y \to -\infty$.

Our previous analysis leading to eq. 46, resulted in the same conclusion. The difference is that eq. 46 applies to all cases, whereas eq. 47 applies only to the case of $S = 0$ and $\rho = 1$ for the free-free boundary condition.

We find that eq. 31 is also satisfied if both $\mathrm{Bi}(-x) = 0$ and $G_4 = 0$. Here, the eigenvalue curves go through the lattice points given by

$$x = b_n; \;\; y = b_m \text{ or } y = b'_m \,. \tag{48}$$

where $b_n$ and $b'_n$ represent the negative of zeros of Bi and Bi′. We note that this set of lattice points does not contain the points at x or $y = -\infty$ because Bi or Bi′ do not go to zero.

Next, consider the case of the rigid-rigid boundary conditions as applies to eq. 34 for $S = 0$ and $\rho = 1$. The counterparts of eqs. 47 and 48 are

$$x = a'_n; \quad y = a_m \text{ or } y = a'_m \,. \tag{49}$$

and

$$x = b'_n; \quad y = b_m \text{ or } y = b'_m \,. \tag{50}$$

Consider now what happens if we set $S = 0$ and $\rho = 1$ in eq. 28 for the free-rigid boundary condition. The combination of functions corresponding to eq. 47 is

$$x = a_n; \quad y = y_n \tag{51}$$

where $y_n$ is a solution of

$$Bi'(-a_n)\, G_1(y) - Ai'(-a_n)\, G_3(y) \,. \tag{52}$$

The problem here is that the zeros depend on $a_n$. The solution of eq. 52 only gives us one point in the x,y plane rather than the lattice of points given by eqs. 47 to 50. The same thing happens if we take $S \neq 0$ or $\rho \neq 1$ for any of the boundary conditions. We can simplify the equation somewhat for $x = a_n$, $b_n$, $a'_n$, or $b'_n$. However, this leads to an equation in y which contains functions of $a_n$, $b_n$, $a'_n$, or $b'_n$ and there is no significant simplification.

For the free-free and rigid-rigid ducts of reference 3, the line $y = x$ was a solution to the eigenvalue equation. If we substitute $y = x$, $\zeta_{20}$ reduces to $\rho^2 x$ and $G_{17}$ of eq. 26 and $G_{16}$ of eq. 25 both identically go to zero. As we shall see later, this solution plays a role in the eigenvalue plots.

## E. EXPRESSIONS FOR FREQUENCY AND PHASE AND GROUP VELOCITY

It is convenient now to introduce expressions that convert the canonical variables into physical quantities of interest. As discussed in the derivation of eq. 14 of reference 1, the frequency may be written as

$$f = K\, f_{ca} \tag{53}$$

where

$$f_{ca} = |y - x|^{3/2} \tag{54}$$

and

$$K = |C_1^2\ C_2^{-2}\ - 1|^{-3/2}\ |\gamma_1|\pi^{-1}\ . \tag{55}$$

Here, $f_{ca}$ of eq. 54 is known as the canonical frequency. It is related to the physical frequency by the scale constant K of eq. 55. As expressed in reference 1 for the case A profile y–x and $C_1^2C_2^{-2} - 1$ are both positive while both are negative for the case B profile. This is how the two sets of eigenvalues are related to their respective profiles. In any case, the use of absolute value signs in eqs. 54 and 55, allows us to treat both cases A and B modes.

Equation 53 gives the frequency as a function of x, since the eigenvalue solutions gives y as a function of x. The phase velocity may now be determined from

$$C_p = C_1[1\ -\ f^{-2/3}\pi^{-2/3}|\gamma_1|^{2/3}x]^{-1/2}\ . \tag{56}$$

This equation follows from the discussion of eq. 17 of reference 1. Equation 56 gives the phase velocity as a function of frequency.

The expression for group velocity is given by

$$C_g = C_p[1\ +\ (C_p^2\ - C_1^2\ )/3C_1^2\ \ +\ C_p^2\ (C_2^{-2}\ - C_1^{-2}\ )L/3]^{-1} \tag{57}$$

where

$$L = (1 - dy/dx)^{-1}\ . \tag{58}$$

The deviation of eq. 57 is given in the discussion of eq. 69 in reference 1. Here, dy/dx is the slope of the eigenvalue curves and is evaluated as

$$dy/dx = -\ (\delta G/\delta x)/(\delta G/\delta y) \tag{59}$$

with the use of partial derivatives of section 2B.

Equations 53 to 59 can be applied to all canonical eigenvalue problems. Our application to two-layer bounded ducts only enters the equation through x and y and the particular form used in eq. 59.

## F. ESTIMATE OF CRITICAL FREQUENCIES

An important aspect of the coupling between double ducts are the critical frequencies. These are the frequencies where the difference in phase velocities between adjacent modes form a relative minimum. At these frequencies, the eigenfunctions for adjacent modes display a similarity associated with strong coupling between the ducts.

Exact evaluation of the critical frequencies requires a detailed evaluation of the mode eigenvalues. However, certain relatively simple approximations to these critical frequencies are available from conventional eigenvalue approaches. This section reviews the results of the conventional approach, develops approximations for the canonical eigenvalue approach, and compares the results for the two approaches.

In the case of conventional mode theory, we consider plots of phase velocity versus frequency for each of the idealized single ducts of the double-duct profile. The frequencies where these plots intersect are an estimate of the critical frequencies of the double duct. For over 20 years we have used the phase-integral method of reference 2 to obtain these estimates. However, the work of reference 2 has demonstrated that the exact normal mode solutions for the idealized single ducts lead to better estimates than does the phase-integral method.

Consider this approach for the free-rigid boundary condition in figure 1. From eq. 54 of reference 2, the phase velocities in the upper duct may be written as

$$C_p = C_1[1 - f^{-2/3}\pi^{-2/3}|\gamma_1|^{2/3}a_n]^{-1/2} \tag{60}$$

and those of the lower duct as

$$C_p = C_3[1 - f^{-2/3}\pi^{-2/3}|\gamma_{20}|^{2/3}a'_m]^{-1/2} \tag{61}$$

where $\gamma_{20}$ is the gradient at the bottom interface. If we equate eq. 60 to 61 and solve for f, we obtain

$$f = \pi^{-1}|\gamma_1|(\rho^{-2}a'_m - a_n)^{3/2}\,(C_1^2 C_3^{-2} - 1)^{3/2}. \tag{62}$$

To obtain eq. 62 we make use of

$$(\gamma_{20}/\gamma_1)^{2/3} = (\gamma_2/\gamma_{10})^{2/3} = \rho^{-2}\ . \tag{63}$$

Equation 63 follows from eq. 5 of reference 1. For f to be real

$$\rho^{-2}\,a'_m > a_n \text{ for } C_1 > C_3 \tag{64}$$

and

$$\rho^{-2}\,a_m' < a_n \text{ for } C_1 < C_3\ . \tag{65}$$

Here, m and n are independent and may be any mode numbers provided eqs. 64 or 65 are satisfied.

Note that eq. 62 breaks down when $C_1 = C_3$. This means that the curves of eqs. 60 and 61 do not intersect but run parallel to each other in a manner similar to the curves for different mode numbers in a single duct. When $C_1 = C_3$, two cases can occur. When

$$|\gamma_1|^{2/3} a_n \neq |\gamma_{20}|^{2/3} a'_m \tag{67}$$

i.e., when

$$\rho^2 = a'_m/a_n , \tag{68}$$

the curves for modes m and n are superimposed.

Equations 60 to 68 apply to the free-rigid boundary condition. However, they also apply to the free-free or rigid-rigid boundary conditions if we replace $a'_m$ by $a_m$ or $a_n$ by $a'_n$, respectively.

Two subcases of eq. 68 occur. One subcase is $\rho = 1$ for the free-free or rigid-rigid boundary condition. Here, the counterparts of eq. 68 are satisfied for m = n. This is a case of symmetry in which the curves of eq. 60 are identical to those of eq. 61. Each curve of eq. 60 lies on the corresponding curve of eq. 61. This subcase cannot occur for the free-rigid boundary condition because the mixed boundary condition breaks the profile symmetry.

The second subcase occurs when there is no profile symmetry and the gradients are constructed to satisfy eq. 68 or its free-free or rigid-rigid counterparts for a particular choice of m and n. Here, mode n of the upper duct is superimposed on mode m of the lower duct. In the case of the free-rigid boundary condition, m may be equal to n.

Equations 62 and 68 apply to the double-duct configuration of figure 1. However, these equations have similar counterparts for any double-duct configuration. There is an equivalent to eq. 62 so long as the minimum sound speed for each of the two ducts is not the same. Here, critical frequencies are formed. An example of this case is presented in reference 2 with more detail presented in reference 4. Here, the double-duct configuration is formed by two refractive ducts, each with its own axial sound speed. There are also counterpart equations to eqs. 66 and 68 when the minimum sound speed of the two ducts is the same.

An example of the situation, illustrated by eq. 68, has been investigated by conventional mode approaches in an unpublished manuscript. Some limited results on the sound-speed profile and phase and group velocity are published in reference 6. This investigation was carried out because we anticipated that superimposed phase velocity curves would represent a case of "supercoupling," since strong coupling effects were present in the usual case where the phase velocity curves intersected at a single point.

The profile configuration chosen for this investigation was a positive-gradient surface duct overlaying a symmetric refractive duct. Here, eq. 60 applies as is. Equation 61 is modified to accommodate a symmetric refractive duct with axial gradients of $\pm \gamma_a$. In eq. 64, $C_3$ the axial sound speed is equal to $C_1$ and $\gamma_{20}$ is replaced by $\gamma_a$. From eq. 82 of reference 2, we find that that $a'_m$ applies for the odd modes, but $a_m$ applies for the even modes. We wished to superimpose mode 1 of the upper duct on mode 1 of the lower duct. The equivalent to eq. 68 then becomes

$$\gamma_1 = \gamma_a (a'_1/a_1)^{3/2} = \gamma_a \times 0.2876287023 \,. \tag{69}$$

The numerical results obtained for this profile will be discussed in section 3 when an example of the application of eq. 68 is presented.

Now, consider the canonical eigenvalue approach. As will be demonstrated later, the canonical eigenvalue plots indicate that the critical frequencies are approximated by the intersection of the vertical asymptotes of eqs. 40 or 41 with the slant asymptotes of eqs. 42 or 44. In the case of the free-rigid boundary condition at the point of intersection, eqs. 40 and 42 lead to

$$y - x = S^{-1}(\rho^{-2} a'_m - a_n) \,. \tag{70}$$

Our interest is in the case A modes for which $y < x$ and $C_1 < C_2$. The condition that $y < x$ (corresponding to real frequencies) leads to the same conditions as eqs. 64 and 65. If we substitute eq. 70 into eq. 53, we obtain eq. 62. Thus, the intersection of asymptotes in the canonical approach leads to the same approximations for the critical frequencies obtained from customary mode theory by the intersection of the phase velocity versus frequency curves for the two single ducts.

Next, consider the case of $S = 0$. Here, the two asymptotes are vertical as given by eqs. 40 and 43. These asymptotes are superimposed when

$$\rho^2 = a'_m/a_n \,, \tag{71}$$

which is the same condition as eq. 68. For the free-free, or rigid-rigid cases, eqs. 70 and 71 apply with the replacement of $a'_m$ by $a_m$, respectively. For these cases, eq. 71 is satisfied for $m = n$ and $\rho = 1$, which is the same circumstances as discussed in connection with eq. 68 in the conventional approach.

Thus, the canonical approximation gives the same result as the conventional approximation for conditions under which the mode eigenvalues are separated or not separated for the case of $S = 0$. However, there is a significant difference between the two approximations when we consider frequency. As will be demonstrated later, two canonical eigenvalue curves have the common asymptote of eq. 71 or its equivalent for the other boundary conditions. These two curves only intersect at $y = -\infty$ and finite x. From eqs. 53 and 54, this corresponds to infinite frequency. Thus, the canonical approximation yields the same phase velocity for these paired modes only at infinite frequency; whereas the conventional approximation states that the paired modes have the same phase velocity for all frequencies.

## G. EIGENFUNCTIONS

This section treats the eigenfunctions. Eigenfunctions are defined here as solutions that satisfy the Helmholtz equation and the boundary and interface conditions.

The eigenfunction in layer i is given by

$$F_1(Z) = D_i\, A_i(-\zeta_i) + E_i\, Bi(-\zeta_i)\ . \tag{72}$$

Equation 72 is the general solution to the Helmholtz equation which for the profile of eq. 1 reduces to Airy's differential equation. Here

$$\zeta_1 = x - a_1 Z \tag{73}$$

$$\zeta_2 = \rho^2 y - \rho^{-1} a_1 (Z - Z_2) \tag{74}$$

and

$$a_1^3 = -2\gamma_1 \omega^2 / C_1^3\ . \tag{75}$$

The remaining task is to specify $D_i$ and $E_i$ so that the boundary and interface conditions are satisfied. First, consider the case of a free surface. Here,

$$D_1 = Bi(-x) \text{ and } E_1 = -Ai(-x) \tag{76}$$

satisfy the surface boundary condition. We now define $F_1(-y)$ as eq. 72 evaluated at the bottom of layer 1.

$$F_1(-y) = Bi(-x)\, Ai(-y) - Ai(-x)\, Bi(-y)\ . \tag{77}$$

Next, we define

$$F_1' = dF/D\zeta\ . \tag{78}$$

Hence,

$$F_1'(-y) = -Bi(-x)\ Ai'(-y) + Ai(-x)\ Bi'(-y)\ . \tag{79}$$

Equations 79 and 80 of reference 1 give the solutions for $D_2$ and $E_2$ as

$$D_2 = \pi\,[F_1(-y)\ B_i'(-\rho^2 y) - \rho F_1'(-y)\ Bi(-\rho^2 y)]\ . \tag{80}$$

and

$$E_1 = -\pi\ [F_1(-y)\ A_i'(-\rho^2 y) - \rho F_1'(-y)\ Ai(-\rho^2 y)]\ . \tag{81}$$

Equations 80 and 81 satisfy the continuity conditions at the interface between layers 1 and 2. The boundary condition at the bottom is satisfied by the eigenvalue equation, since eqs. 76, 80, and 81 only satisfy the surface and interface conditions.

Now, consider the case of a rigid surface. Here, we replace Ai(-x) and Bi(-x) in eqs. 76, 77, and 79 by Ai'(-x) and Bi'(-x), respectively.

## H. MODE DEPTH FUNCTIONS

The normalized mode depth functions are given by

$$U_n(Z_0)\ U_n(Z) = F_n(Z_0\ F_n(Z)/D_n \tag{82}$$

where n is the mode number, $Z_0$ is the source depth, and Z is the receiver depth. The $F_n(Z_0)$ or $F_n(Z)$ is the $F_i$ of eq. 72 for the layer in which the source or receiver respectively are located, as evaluated for mode n.

The major objective of this section is to provide expressions for $D_n$, the normalization factor. Reference 1 defines a canonical normalization factor $D_c$ related to $D_n$ by

$$D_n = a_1^{-1}\ D_c\ . \tag{83}$$

The significant feature of $D_c$ is that it can be expressed in terms of canonical variables.

However, in the preparation of this report, we found an improved method of treatment. If we substitute eq. 53 for the frequency dependence in $a_1$, eq. 83 may be written as

$$D_n = J\ D_{ca} \tag{84}$$

where

$$D_{ca} = |y - x|^{-1}|D_c| \tag{85}$$

and

$$J = C_1|C_1^2\ C_2^{-2}\ - 1|\ |2\gamma_1|^{-1}\ . \tag{86}$$

Equation 85 defines a new canonical normalization factor that can be converted to $D_n$ by the scale factor of eq. 86. The original normalization factor required two plots such as presented in reference 3. The first was a plot of $D_c$ versus x and the second was $D_n$ versus frequency. However, these two plots may be replaced by a single plot in which we plot $D_{ca}$ versus $f_{ca}$. The application of the scale factor J to the ordinate and the scale factor K to the abscissa gives $D_n$ as a function of frequency. Numerical examples of this will be presented later.

If one solves eq. 1 for $Z_2$, one obtains the right side of eq. 86. Thus, the scale factor J is the thickness of layer 1. This was not recognized in the original deviation until we observed that the numerical values of J and $Z_2$ were the same for a particular example.

The next step is to present the various expressions for $D_c$ for use in eq. 85. From eq. 90 of reference 1, $D_c$ may be expressed as

$$D_c = D_s + D_b + D_{n1} \tag{87}$$

where $D_s$ and $D_b$ are contributions at the upper and lower boundaries respectively and $D_n$ is a contribution at the interface between layers 1 and 2. From eqs. 93 and 97 of reference 1

$$D_{n1} = (1 + \rho^3)[y\ F_1^2(-y) +\ F_1'^2(-y)]\ . \tag{88}$$

Here, $F_1$ and $F_1'$ are given by eqs. 77 and 79 or their rigid surface counterparts.

In eq. 87, $D_s$ and $D_b$ depend on the surface and bottom boundary conditions. For a free or rigid surface,

$$D_s = -\pi^{-2} \tag{89}$$

or

$$D_s = -x\pi^{-2}\ . \tag{90}$$

For a free or rigid bottom,

$$D_b = -\rho \; F_2'^2(-\zeta_{20}) \tag{91}$$

or

$$D_b = -\rho \, \zeta_{20} \, F_2^2(-\gamma_{20}) \tag{92}$$

where

$$F_2'(-\zeta_{20}) = -D_2 \, Ai'(-\zeta_{20}) - E_2 Bi'(-\zeta_{20}) \tag{93}$$

$$F_2(-\zeta_{20}) = D_2 \, Ai(-\zeta_{20}) + E_2 Bi'(-\zeta_{20}) \tag{94}$$

and $\zeta_{20}$ is given by eq. 11. Equations 89 to 94 follow respectively from eqs. 94, 95, 98, 99, 76, and 73 of reference 1.

## I. DETERMINATION OF EIGENVALUES FOR A GIVEN FREQUENCY

Consider the case where one wants to determine the eigenvalues for a given frequency, $f_o$. For example, we may wish to sum up the modes at a given frequency to determine the field or we may wish to compare the standing wave patterns of modes at a given frequency. This requires a special computer routine because the points at which the canonical eigenvalues are available will lead to different frequencies for the different modes. We cannot rely upon some simple interpolation routine because the sensitivity of the mode evaluation at or near the critical frequencies require a high degree of accuracy.

From eqs. 53 and 54, we note that

$$f_o = |y_o - x_o|^{3/2} \, K \, . \tag{95}$$

Here, $f_o$ is the given frequency and K is known from the profile parameters. Our task is to determine $y_o$ and $x_o$. From eq. 95 it follows that

$$y_o = x_o + (K f_o^{-1})^{2/3} \tag{96}$$

We now solve the eigenvalue equation

$$G(x, y) = 0 \tag{97}$$

under the constraint of eq. 96. We iterate eq. 97 to determine $x_o$ by substituting eq. 96 for y in eq. 97. The derivative of eq. 97 is given by

$$dG/dx = \delta G/\delta x + (\delta G/\delta y) \; (dy_o/dx_o) \; . \tag{98}$$

From eq. 96 it follows that $dy_o/dx_o = 1$. Thus, eq. 98 reduces to

$$dG/dx = \delta G/\delta x + \delta G/\delta y \ . \tag{99}$$

Starting estimates of $x_o$ are obtained from the plots of canonical frequency versus x. The expressions for G(x,y), $\delta G/\delta x$, and $\delta G/\delta y$, appropriate to the boundary conditions, are used in the iteration, where eq. 96 is always substituted for y throughout the evaluation.

## J. ESTIMATES OF EIGENVALUE DIFFERENCES AT THE CRITICAL FREQUENCIES

Section 2F presented estimates of the critical frequencies in terms of the parameters, S, ρ, and Airy function zeros. In this section, we present approximations to the eigenvalue differences at the estimate of critical frequencies. These differences are important because they are a measure of the amount of coupling between the two modes associated with the critical frequency.

Appendix A derives expression for approximate eigenvalues based on a Taylor series expression about $x_o$ for fixed $y_o$. Here, $x_o$ and $y_o$ represent a point of intersection of the vertical asymptotes of eqs. 40 or 41 with the slant asymptotes of eqs. 42 or 44. This expression is

$$(x - x_o)^2 + b(x - x_o) + c = 0 \ . \tag{100}$$

The two values of x for this quadratic equation represent an approximation to the eigenvalues for the two modes associated with the intersection of asymptotes. These values of x correspond to $y = y_o$.

First, consider the case of the free-rigid boundary condition. Here,

$$b = K_n \rho^{-2}(1 - S)^{-1}(G_2/G_4) + L_m(G_3/G_4) \tag{101}$$

and

$$c = M_{mn} \rho^{-2}(1 - S)^{-1}(G_1/G_4) \ . \tag{102}$$

The coefficients $K_n$, $L_m$, and $M_{mn}$ are constants that depend upon the particular intersection point. The coefficients have no connection with the factors K and L previously given. They are given by

$$K_n = -[\pi a'_n \mathrm{Ai}^2(a'_n)]^{-1} \tag{103}$$

$$L_m = -[\pi \mathrm{Ai}'^2(a_m)]^{-1} \tag{104}$$

$$M_{mn} = L_m K_n \ . \tag{105}$$

Here, $a_m$ is the negative of the m'th zero of Ai and $a'_n$ is the negative of the n'th zero of Ai'. Here,

$$x_o = a_m \tag{106}$$

and

$$y_o = (1 - S^{-1})a_m + a'_n/\rho^2 S \ . \tag{107}$$

For the free-free boundary condition, eqs. 101, 102, 104, and 105 apply with

$$K_n = L_n \tag{108}$$

and

$$M_{mn} = L_m L_n \ . \tag{109}$$

Equation 107 is replaced by

$$y_o = (1 - S^{-1})a_m + a_n/\rho^2 S \ . \tag{110}$$

For the rigid-rigid boundary condition, eqs. 101, 102, and 103 apply with

$$L_m = K_m \tag{111}$$

and

$$M_{mn} = K_m K_n \ . \tag{112}$$

Equations 106 and 107 are replaced by

$$x_o = a'_n \ . \tag{113}$$

and

$$y_o = (1 - S^{-1})a'_m + a'_n/\rho^2 S \ . \tag{114}$$

## K. PHASE VELOCITY DIFFERENCES AND MODE INTERFERENCE RANGES

First, we develop an expression for the difference in phase velocity between the adjacent modes at the critical frequency. Let $x_{n+1}$, $y_{n+1}$ and $x_n$, $y_n$ be the eigenvalues for mode n + 1 and mode n at the critical frequency. If one expands eq. 55 by the binomial expression for mode n + 1 and for mode n and subtracts, one obtains

$$C_{p,n+1} - C_{p,n} = C_1 f^{-2/3} \pi^{-2/3} |\gamma_1|^{2/3} \, 2^{-1} (x_{n+1} - x_n) \ . \tag{115}$$

The substitution of eq. 53 into eq. 115 leads to

$$C_{p,n+1} - C_{p,n} = C_2 (1 - C_1^2 \, C_2^{-2}) 2^{-1} (x - y)^{-1} (x_{n+1} - x_n) \ . \tag{116}$$

Since the frequency is the same for both modes, x – y may be evaluated from either eigenvalue.

Estimates of the phase velocity differences corresponding to the estimates of section 2J are readily obtained with the use of eq. 116. Here, $(x_{n+1} - x_n)$ is given by the discriminate of eq. 100. In the case of the free-rigid boundary condition, x and y are estimated by eqs. 106 and 107. In the case of the free-free boundary condition, y is estimated from eq. 107; and in the case of the rigid-rigid boundary condition, x and y are estimated from eqs. 113 and 114.

Reference 4 discusses the mode interference distance. Since modes have slightly different phase velocities, the phase relationship between modes changes with range. The mode interference distances is the difference between successive range points where the modes are in (or out) of phase. The mode interference distance may be expressed as

$$R_{n+1} = f^{-1} \, C_{p,n} \, C_{p,n+1} \, [C_{p,n+1} - C_{p,n}]^{-1} \ . \tag{117}$$

If we substitute eqs. 53 and 116 into eq. 117 and simplify, we obtain

$$R_{n+1} = 2 C_2 \pi |\gamma_1|^{-1} |C_1^2 \ C_2^{-2} \ - 1|^{1/2} (x - y)^{-1/2} (x_{n+1} - x_n)^{-1} \ . \tag{118}$$

One may estimate $R_{n+1}$, based on the estimates of section 2J, as just discussed for estimates of the phase velocity differences.

# 3. NUMERICAL EXAMPLES

This section presents numerical examples of two different types of functions, i.e., the canonical and physical functions. The canonical functions are those which are completely determined by the parameters $\rho$ and S and the boundary conditions. These include the canonical eigenvalues, the canonical frequency, the canonical group velocity factor, and canonical eigenfunction normalization coefficient. The physical functions are those which are determined from the canonical functions and a particular choice of the sound-speed profile parameters. The first of these functions relates acoustic frequency to the eigenvalue solutions. Three other physical functions are plots of phase velocity, group velocity, and eigenfunction normalization coefficients, all given as functions of frequency. The last of the physical functions are plots of the eigenfunctions. Here, the eigenfunctions (standing waves) are plotted as a function of receiver depth for a particular choice of frequency and source depth.

## A. FREE-RIGID BOUNDARY, $\rho = 1, S = 0$

This particular case was chosen for first presentation because this case is the simplest double duct with no coupling effects between the ducts. For $S = 0$, the surface and bottom sound speeds of figure 1 are the same. For $\rho = 1$, the slopes at the interface between layers are equal but of opposite sign. Thus, this is the class of all two-layer profiles that are symmetric about an axis of minimum or maximum sound speed and with free-rigid boundary conditions.

Figure 2 presents the canonical eigenvalues for this case. We point out some features common to all canonical eigenvalue plots of this report. Each plot contains one set of horizontal asymptotes. These are the solid horizontal grid lines, and are solutions to eq. 46. For the case of $\rho = 1$, this reduces to $y = a_n$ or $a'_n$. Each plot contains two sets of asymptotes for $y = -\infty$, shown by the vertical dotted lines. One set of these asymptotes is always vertical and independent of the values of $\rho$ and S. For the free surface, these asymptotes are given by $x = a_n$. The second set of asymptotes is usually a slant set except for the special case of $S = 0$. Here, they are vertical and for $\rho = 1$, the solution for a rigid bottom is $x = a'_n$. Since the critical frequencies are associated with the intersection of the vertical and slant asymptotes, there are no critical frequencies for $S = 0$ because the slant asymptote became vertical for this special case.

Next, we point out various properties that apply to all of the eigenvalue plots of this report. These properties also apply to figures 2 to 4 of reference 3 for single ducts. Indeed, these properties are fundamental to the canonical approach. We state these properties without justification because such justification may be found in reference 3.

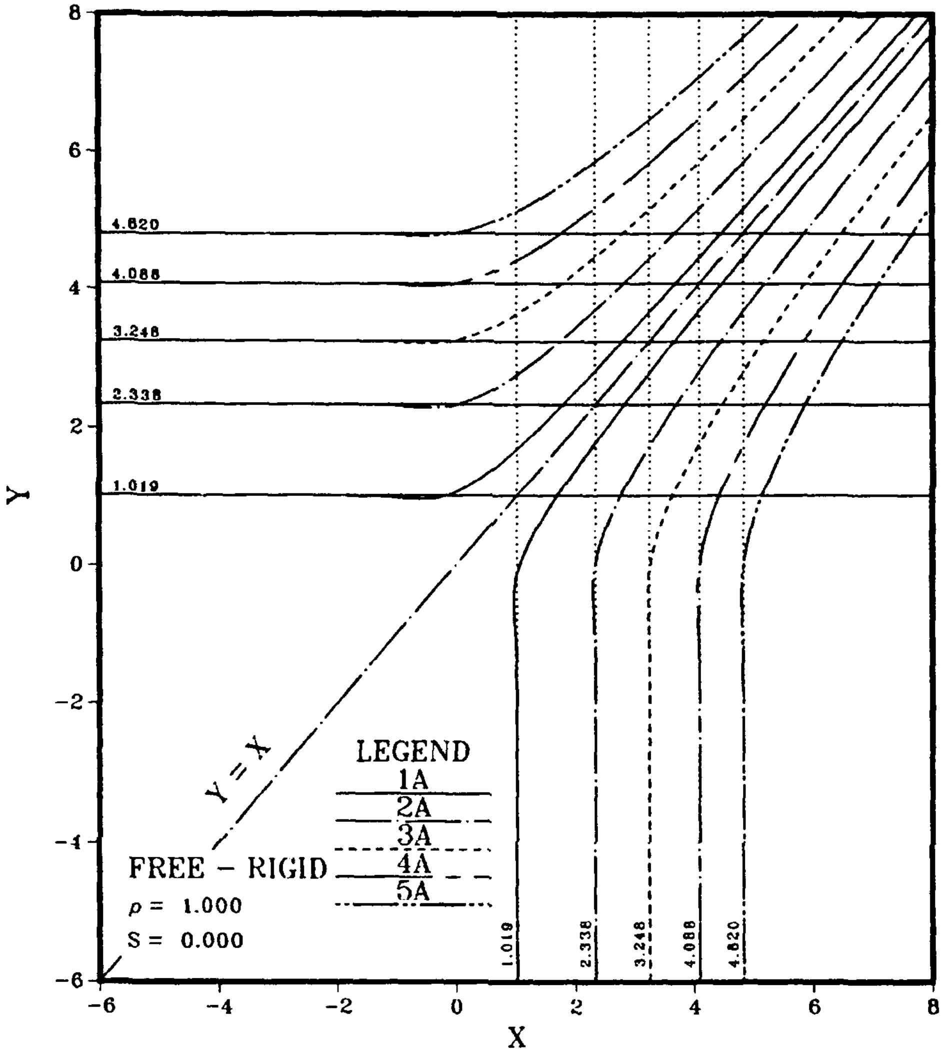

Figure 2. Eigenvalues for S = 0, ρ = 1, free-rigid boundary.

Observe the line y = x. This line is given in all eigenvalue plots because it divides the modes into two families, with the modes below and above the line associated with cases A and B respectively of figure 1. The mode count increases as each family member moves away from the line y = x. To be more specific, the modes are ordered by their displacement from the line y = x for fixed y. Unless otherwise specified, we will present the first five modes of each family. The same method of coding will be used to associate the eigenvalues and other curves with a particular mode number. Mode 1 curves will be solid. Mode 2 curves will consist of long dashes separated by a dot. Mode 3 curves will consist of short dashes, Mode 4 curves will consist of short and long dashes. Mode 5 curves will consist of long dashes separated by two dots.

The large negative values of y or x correspond to high frequencies. The frequency decreases as we move along a given case A mode to larger values of y or along a given case B mode to larger values of x. For large positive values of y or x, the curves approach the line y = x as an asymptote. These values correspond to low frequencies because the frequency is zero for the line y = x.

For the A set of modes, the point where the curves cross y = 0 corresponds to the ray with phase velocity equal to the interface sound speed. Thus, the eigenvalues with positive y correspond to rays reflecting from both boundaries. The eigenvalues with negative y correspond to modes trapped in the upper or lower duct. In this case, the odd modes correspond to rays reflecting from the bottom and form a refractive apex in layer 2 while the even modes correspond to rays reflecting from the surface and form a refractive nadir in layer 1. This association is made because the odd asymptotes are determined by $x = a'_n$ for the rigid bottom while the even asymptotes are determined by $x = a_n$ for the free surface.

For the B set of modes, the point where the curves cross x = 0 corresponds to the ray with phase velocity equal to the surface sound speed. Thus, positive values of x correspond to modes reflecting from the ocean surface (and also from the bottom for this case of S = 0), while negative values of x correspond to rays that form an apex in layer 1. For this case of S = 0, they also form a nadir in layer 2.

Note that the spacing between the eigenvalues of a given family is relatively uniform. This is not surprising for the case B modes because this is a characteristic property of all single ducts. As we shall see presently, this is also true for the case A modes reflecting from both boundaries (y > 0), but is not generally true for case A modes for y < 0. We note that for y somewhat greater then 0, the spacing between mode 1 of case A and mode 1 of case B is also comparable to the spacing between modes 1 and 2 of cases A or B. This property will take on more significance when we investigate the other two-boundary conditions.

The case of figure 2 is unique in that the cases A and B eigenvalues are symmetric about the line y = x. This may be demonstrated by simplifying eq. 28 for the case of $\rho = 1$ and S = 0, and noting that it remains the same eigenvalue equation when x or y are interchanged.

The same general approach was used to generate all eigenvalue curves of this report, such as those of figure 2. Newton's method was applied using eq. 29 (or eq. 32 or 35 for the other boundary conditions) for fixed values of y for the case A modes. Equation 30 (also 33 or 36) was used for fixed values of y for the case B modes. The reason for this choice is that Newton's method, using eq. 29, fails for the case A modes when the slope is vertical and Newton's method, using eq. 30, fails for the case B modes when the slope is horizontal. The iterative process for the cases A and B modes is commenced at large negative values of y and x respectively as given by the asymptotic solutions.

Although we will present three other canonical functions that depend only on ρ and S and are independent of the specific profile parameters, it is onvenient to introduce specific parameters at this point. For all of the case A examples of this report, we choose $C_1 = 1480$ m/s, $C_2 = 1482$ m/s, and $\gamma_1 = 0.02\ s^{-1}$. These are the same parameters used in reference 3 for one-layer ducts. From eq. 1, we determine that $Z_2 = 99.797661$ m and from eq. 3 that $\gamma_{10} = 0.020081186\ s^{-1}$. This gives all of the useful parameters of the first layer. The parameters of the second layer may then be determined from these first layer parameters and the values of ρ and S.

For our values of ρ and S, it follows that $C_3 = C_1$, $Z_3 = 2\ Z_2$, $\gamma_2 = -\gamma_{10}$, and $\gamma_{20} = -\gamma_1$. The left panel of figure 3 is a plot of sound-speed profile used for the case A modes.

The left scale of figure 4 presents the canonical frequency, plotted as a function of x. The right scale gives the acoustic frequency as determined by eq. 84. The scale factor J is given by eq. 86 and is equal to 45.45 for the profile of figure 3. This same value applies to all of the case A modes of this report.

Figure 5 presents the phase velocity as determined by eq. 56. Figure 5 displays a typical behavior for a single duct with a relatively uniform spacing between modes. At high frequencies, all curves asymptotically approach 1480 m/s, the sound speed at the two boundaries. At low frequencies, the curves of figure 5 form vertical asymptotes at the cut-off frequencies of the duct. The evaluation of these cut-off frequencies is very involved and will not be attempted here. Reference 3 presents such an evaluation for a one-layer duct.

Figure 6 presents the canonical group velocity factor of eq. 58 as evaluated using eq. 59. Figure 7 presents the group velocity as a function of frequency. This was evaluated by eq. 57 with the use of L of figure 6. At high frequencies, all curves asymptotically approach 1480 m/s, the sound speed at the two boundaries. As the frequency is decreased to low values, all curves go rapidly toward small values of group velocity corresponding to steep rays reflecting off both boundaries. At intermediate frequencies, the group velocity forms a relative maximum (point of Airy phase). Our previous work with a positive-gradient surface duct overlaying a negative-gradient half space yields results very similar to this. We found that at high frequencies the relative maximum goes to the ray theory value for the ray which grazes the bottom of the surface layer. This is a group velocity one-third of the distance between the surface sound speed and the sound speed at the bottom of the surface layer. For the profile of figure 3, this is a value of 1480.67 m/s, plotted as a horizontal line in figure 7. We see that the same limit appears to apply here.

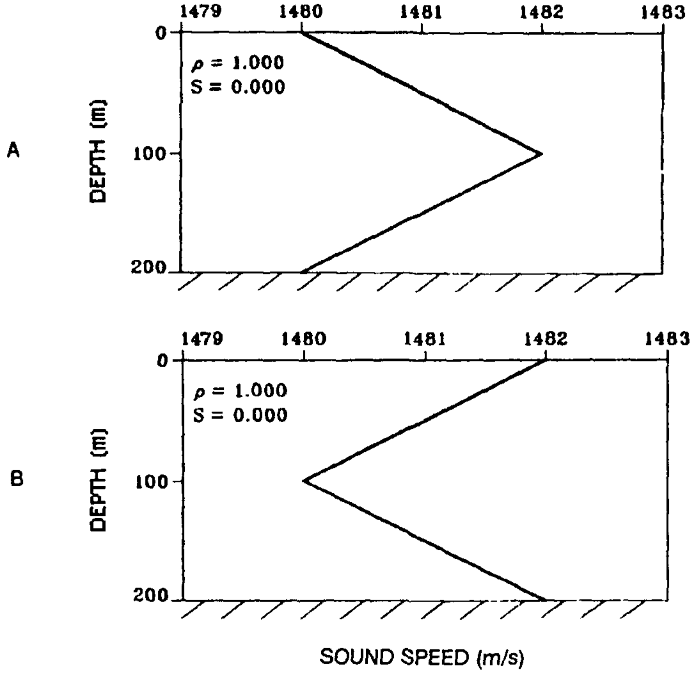

Figure 3. Sound-speed profiles used in the analysis of A and B modes of figure 2.

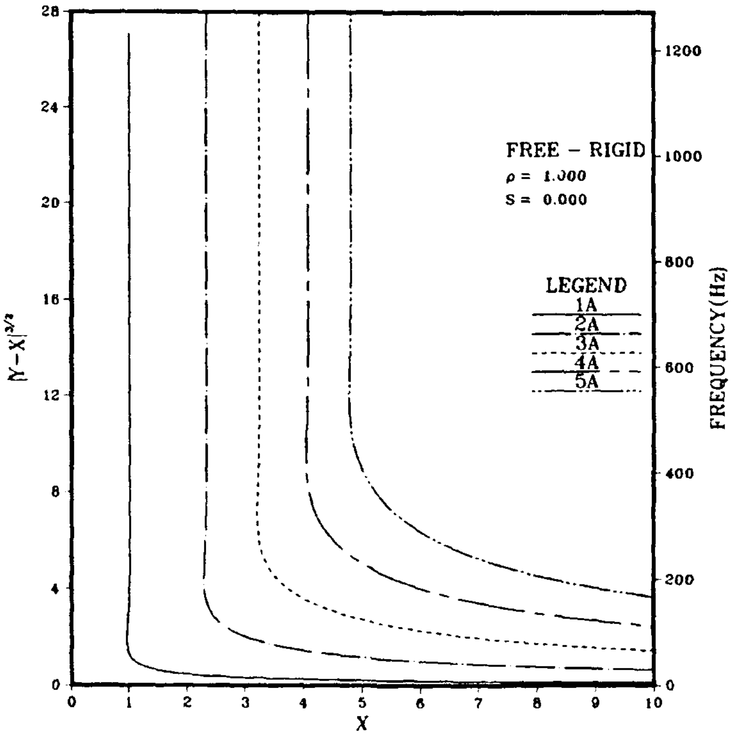

Figure 4. Canonical or acoustic frequencies for the A modes of figures 2 or 3.

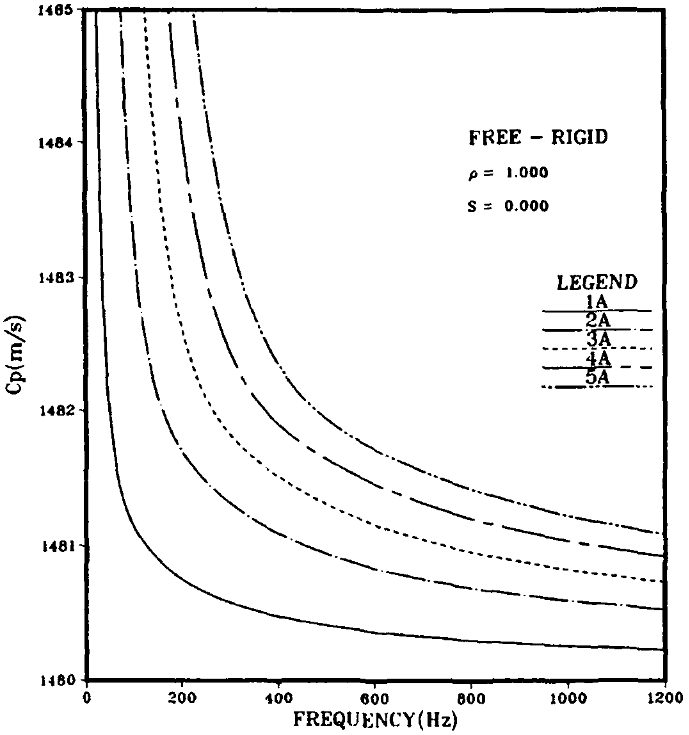

Figure 5. Phase velocities for the A modes of figure 3.

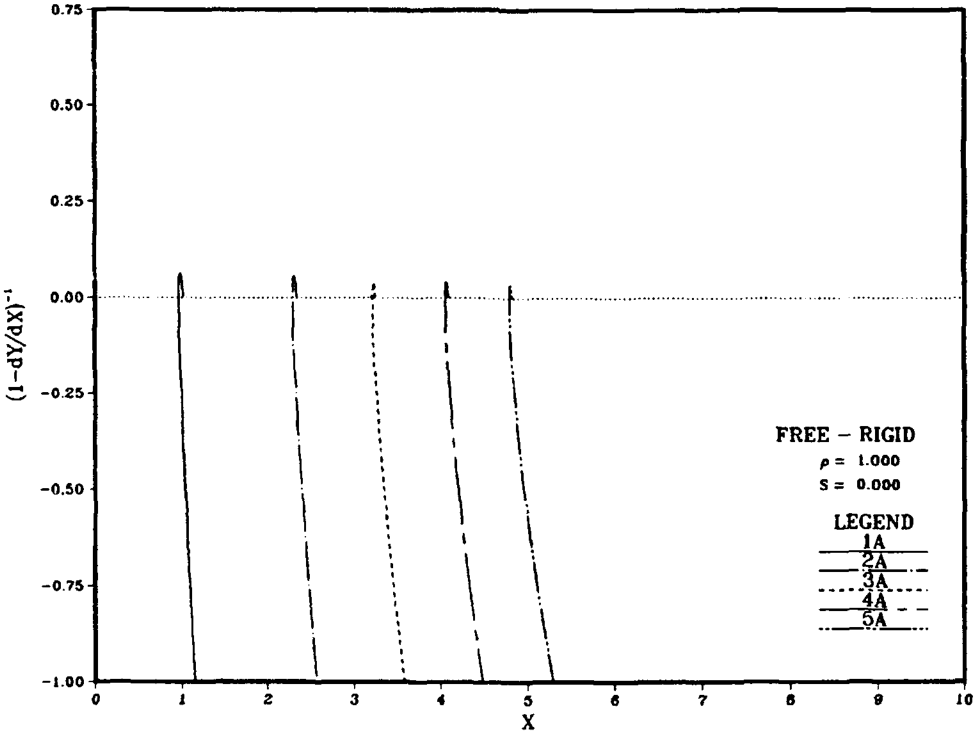

Figure 6. Group velocity factor for the A modes of figure 2.

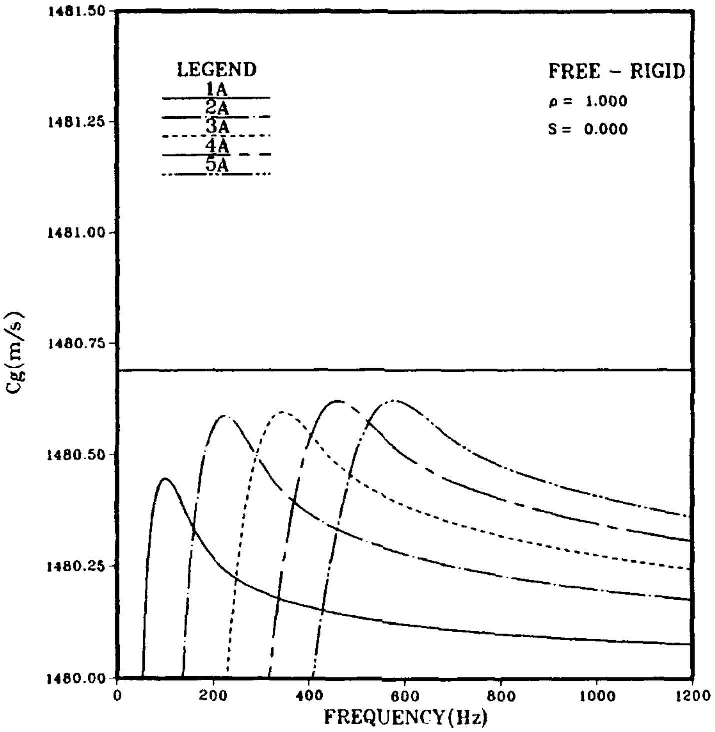

Figure 7. Group velocities for the A modes of figure 3.

The left scale of figure 8 gives the canonical normalization factor of eq. 85 as evaluated by eq. 87 to 94. The right scale gives the customary eigenvalue normalization coefficient as defined by eq. 84. The factor J is the thickness of layer 1 or 99.8 m for the profile of figure 3. The bottom scale is the canonical frequency, whereas the top scale is the acoustic frequency of eq. 53. The curves for modes 2 and 4 (modes trapped in the upper duct) are well behaved. However, the curves for modes 1, 3, and 5 rapidly grow rather large. The dominant terms of $D_c$ lie in eq. 88 and are y $Bi^2(-y)$ and $Bi'^2(-y)$. Both terms diverge as $\pi^{-1}(-y)^{1/2}$ exp $[4(-y)^{3/2}/3]$ for large negative y, i.e., for large frequency. The coefficient for these terms is $Ai^2(-x)$ as can be seen from eqs. 77 and 79. This coefficient is zero for the even modes and the divergent terms drop out. However, the coefficient is not zero for the even modes and $D_c$ diverges for high frequency. We note that for the case of $\rho = 1$, eqs. 80 and 81 reduce to $D_2 = Bi(-x)$ and $E_2 = Ai(-x)$. Thus, the term of eq. 92 poses no problem.

As we shall see later, there are cases for which the $D_n$ for odd modes do not diverge, but form a relative maximum. From eq. 85 we note that even though $D_c$ diverges, $D_{ca}$ and $D_n$ could converge because $(y-x)^{-1}$ goes to zero in the high-frequency limit. We evaluated the $D_{ca}$ of figure 8 using double-precision routines. However, the $D_{ca}$ for odd modes appeared to diverge rather than form a relative maximum.

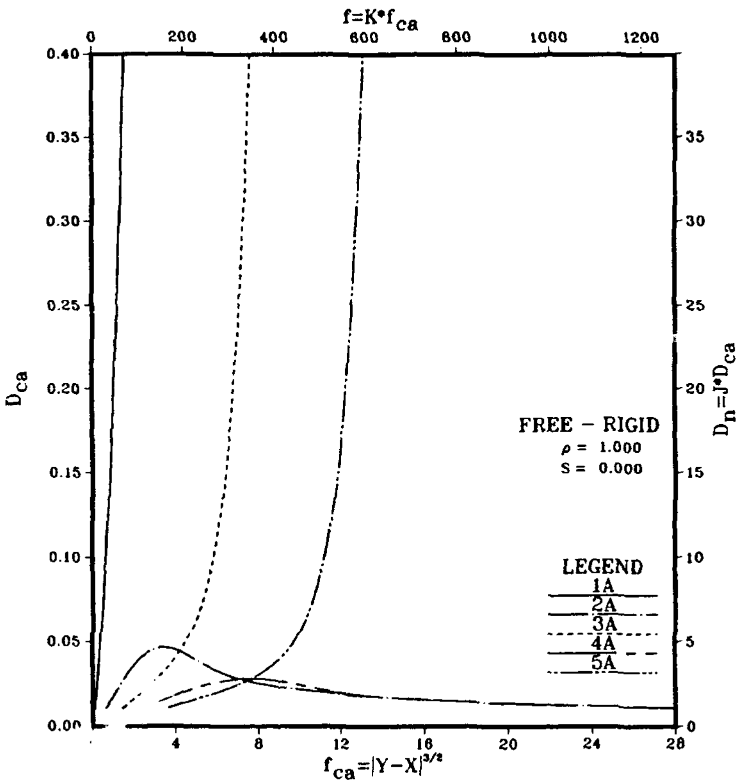

Figure 8. Canonical or customary eigenvalue normalization coefficients for the A modes of figures 2 or 3.

The physical explanation for the different behavior of $D_n$ for even and odd modes lies in the fact that in eq. 76 we have chosen the unnormalized depth function to satisfy the boundary condition at the surface. This is not a good choice for modes highly trapped in the lower duct. We could choose the unnormalized depth function to satisfy the bottom boundary condition. This was the technique used to resolve a similar problem for the single-layer ducts of reference 3. However, in this approach the even modes would then diverge.

Huge or divergent values of $D_n$ do not pose a problem mathematically, because $D_n$ grows large with increasing frequency to compensate for the large growth in the unnormalized depth functions. The only problem this poses is in the presentation of $D_n$ for both upper and lower duct modes on the same scale.

We are not completely satisfied with our present approach, which yields too large a range of values for $D_n$. However, one can multiply the unnormalized eigenfunction by any constant (i.e., a value independent of depth) and this constant will appear squared in $D_n$ to yield the normalized depth function. Thus, $D_n$ is by no means unique but depends on how the unnormalized eigenfunctions are defined. For example, an alternative approach to that illustrated in figure 8 is to divide the present unnormalized eigenfunction of eq. 72 for odd modes by the term Bi′ (-y) and carry out the normalization process in the same manner as before.

We will point out some other interesting properties of the normalization coefficient after we have presented other numerical examples. There appear to be many aspects of $D_n$ that are of further interest. However, the scope of the present report will not permit a thorough analysis.

Figure 9 presents the normalized depth functions at 500 Hz for A modes 1 to 5 as a function of receiver depth for a fixed source depth for a given mode. These curves are generated from eq. 82 with the use of the appropriate normalization values, associated with figure 8. The eigenvalues at 500 Hz, used in this evaluation, were determined by the approach discussed in section 2I. The source depth is 170, 27, 153, 60, and 125 m for modes 1 to 5 respectively. These depths were chosen to enhance the particular mode so that the behavior of the curve for small amplitudes could be determined. The dotted horizontal line represents the interface between layers at 99.8 m. The bottom of the channel is at twice this depth or 199.6 m. The dotted vertical line is the zero origin for the depth functions.

All of the curves go to zero at the surface and have zero slope (form an end point maximum) at the bottom.

There is one method of mode identification from depth function plots that always gives the correct mode number. The mode number is one more than the number of zero crossings. This rule obviously gives the mode number for modes 3 to 5, but it is not quite so obvious for modes 1 and 2. However, an examination of detailed computer printouts reveals that mode 1 values are always positive and that mode 2 values turn negative toward the bottom of layer 2. In this particular example, the mode number is also equal to the number of nodes (zeros) or the number of antinodes (relative or end point maxima). However, later we will present other examples where these criteria for mode identification fail.

Recall that in the discussion of figure 2, we associated odd modes with the lower duct and even modes with the upper duct. In figure 9, modes 1 and 3 are clearly trapped in the lower duct and modes 2 and 4 in the upper duct. Mode 5 has a phase velocity slightly above 1482 m and is not trapped in either duct, although the amplitudes are somewhat larger in the lower layer. Later on, we will see some more impressive examples of how the eigenvalue plots may be used to predict the duct in which the mode is trapped, i.e., the mode has large eigenfunction amplitudes.

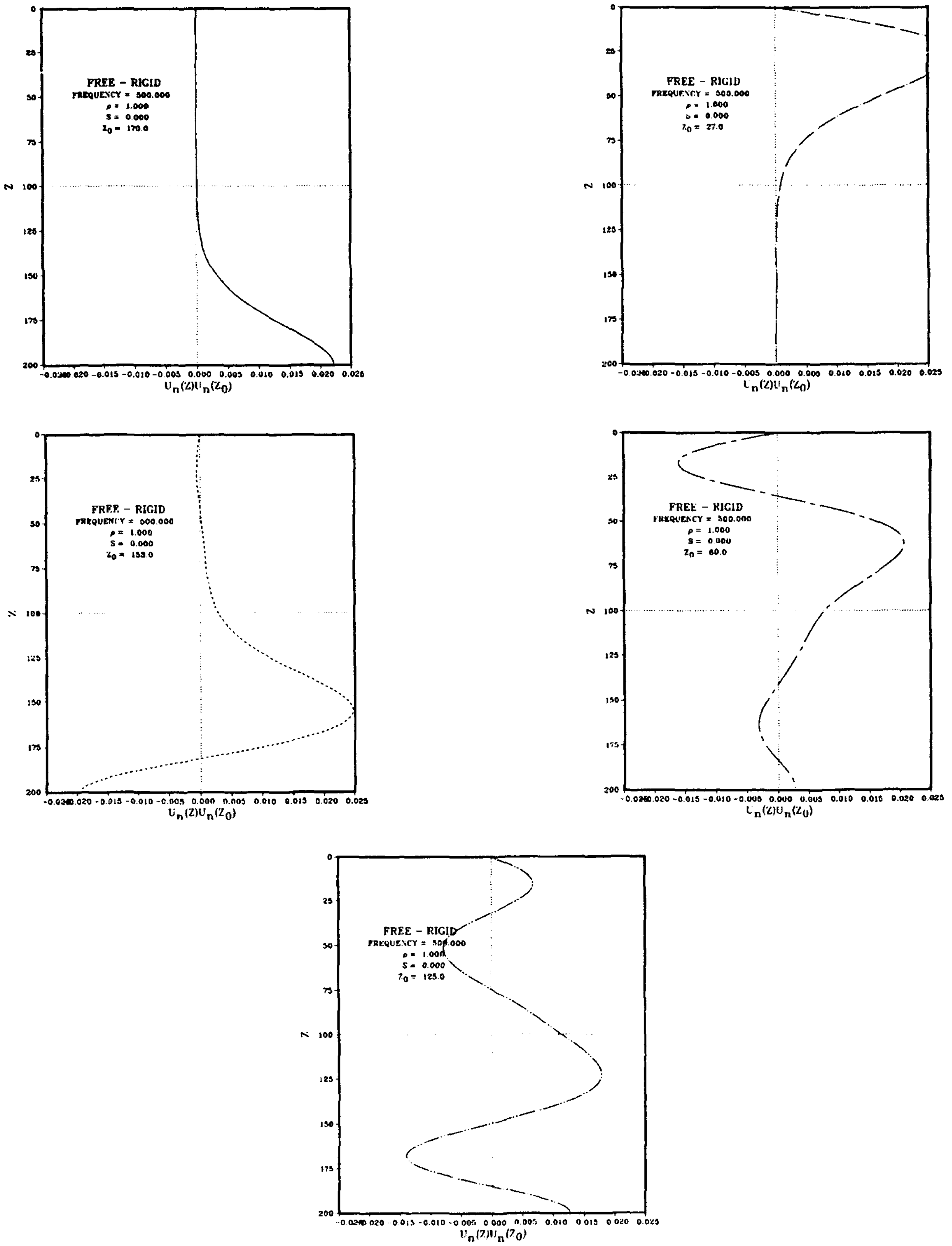

Figure 9. Eigenfunctions at 500 Hz for the A modes of figure 3.

For the most part, we have little interest in the case B modes because they represent propagation in a bounded refractive duct with none of the characteristics of double duct propagation. However, the symmetry about the line y = x in figure 2 makes the case B modes of interest for this special case. We evaluate these modes for the profile parameters given by $C_1$ = 1482 m/s, $C_2$ = 1480 m/s, and $\gamma_1 = -0.02(C_1/C_2)^3 = -0.020081186\ s^{-1}$. This is the profile shown in the right panel of figure 3. These parameters are chosen so as to have a particular relationship with the parameters of the left panel. Let the unbarred values be the parameters for the case A profile and barred values be those for the case B profile. Then, the following relationship holds: $\overline{C}_1 = C_2$, $\overline{C}_2 = C_1$, $\overline{C}_3 = C_2$, $\bar{\gamma}_1 = -\gamma_{10}$, $\bar{\gamma}_{10} = -\gamma_1$, $\bar{\gamma}_2 = \gamma_1$ and $\bar{\gamma}_{20} = \gamma_{10}$. Furthermore, from the symmetry properties $\bar{x} = y$ and $\bar{y} = x$. It follows then from eq. 53 to 55 that

$$\bar{f}_{ca} = f_{ca},\ \overline{K} = K,\ \text{and}\ \bar{f} = f\ ,$$

i.e., the frequency corresponding to the point x, y for case A is the same as that to the point $\bar{x}, \bar{y}$ for case B.

Figure 10 presents the counterpart of figure 4 for the case B modes. The dependent variable is the same in figure 10 as in figure 4. Indeed, if we had plotted the dependent variable as a function of y rather than x in figure 10, it would be identical to the plots of figure 4.

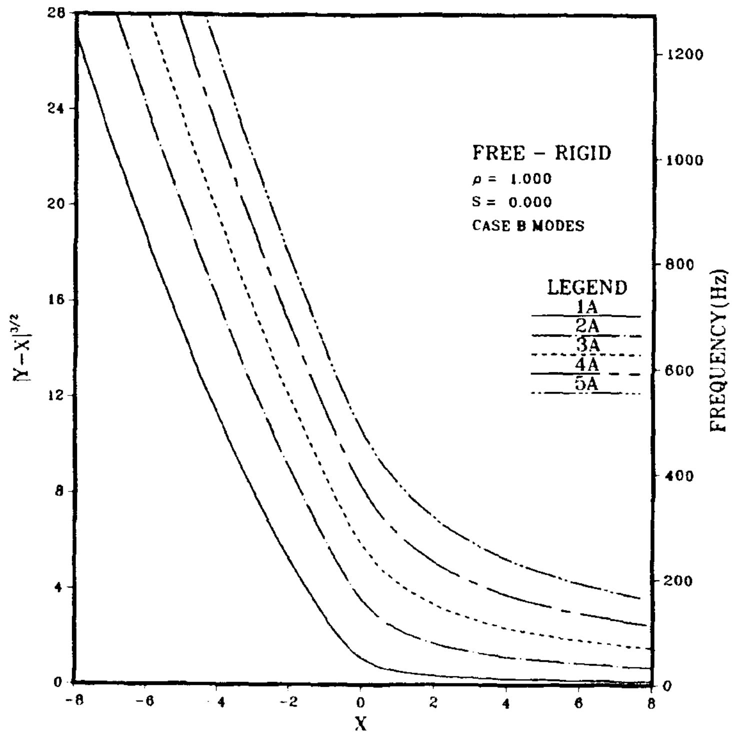

Figure 10. Canonical or acoustic frequencies for the B modes of figures 2 or 3.

The phase velocity counterpart of figure 5 for the case B modes was evaluated and is identical to figure 5. To demonstrate this, we compare the result of eq. 56 as evaluated for the B modes with that of eq. 30 of reference 3 as evaluated for the A modes. These expressions are identical because $\overline{C}_1 = C_2$, $f = f$, $|\hat{\gamma}_1| = |\gamma_{10}|$, and $\overline{x} = y$ .

Figure 11 is the counterpart of figure 6 for the case B modes. The results of figure 11 were used to evaluate the group velocity for the case B modes. This plot was identical to that of figure 7 for the A modes. This property could be demonstrated by comparing the two evaluations of eq. 57. However a much easier demonstration follows from eq. 63 of reference 1. Since the phase velocity is the identical function of frequency for the two cases, eq. 63 easily demonstrates that the group velocities are also identical functions of frequency.

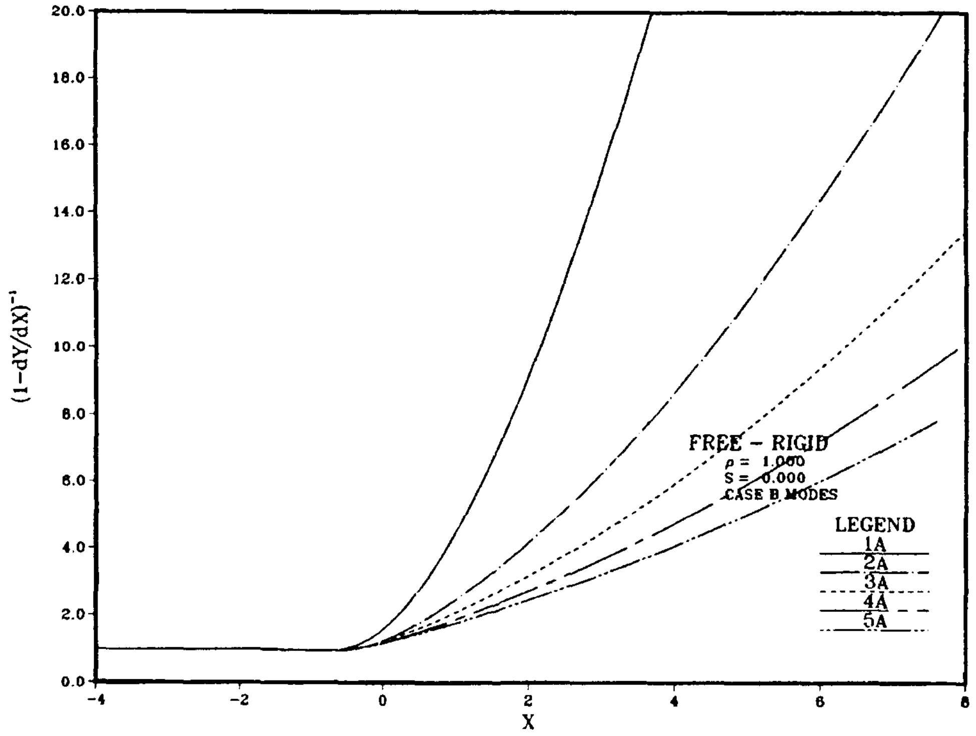

Figure 11. Group velocity factor for the B modes of figure 3.

Figure 12 is the B mode counterpart of figure 8. In contrast to figure 8, $D_n$ diverges with increasing frequency for both even and odd modes. Here the dominant terms of $D_n$, in eq. 88 involves $Bi'^2(-x)$. The coefficient of this term is $Ai'^2(-y)$ in eq. 77 and $[Ai'(-y)]^2$ in eq. 79. Here, $Ai(-y)$ and $Ai'(-y)$ cannot both be zero. Thus, $D_c$ diverges for both A and B modes for large frequency. We note that $D_c$ of eq. 92 reduces to a term containing $-x\ Bi^2(-x)\ Ai^2(-x)$, that has a finite limit for large negative x and poses no problem.

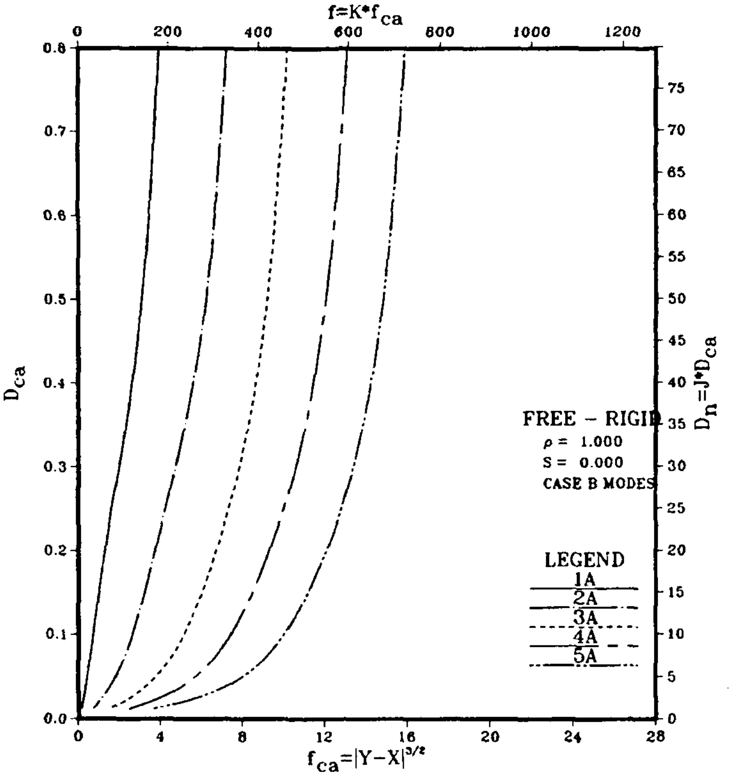

Figure 12. Canonical or customary eigenvalue normalization coefficients for the B modes of figures 2 or 3.

Two other approaches might result in a nondivergent form for $D_n$. One is to choose the unnormalized depth functions so as to automatically satisfy one of the continuity conditions at the axis. The other approach is to divide the eigenfunctions of eq. 72 by the term $B_i(-x)$. A similar approach has already been discussed for the A modes.

Figure 13 is the B counterpart of figure 9. The source depths are 100, 75, 60, 40, and 30 m for modes 1 to 5 respectively. In contrast to case A, the mode amplitudes are comparable in the upper and lower layers. This is the case of a single refractive duct with symmetric sound speeds about the axis. The odd modes have a node near the axis while the even modes have an antinode near the axis. These features do not occur exactly at the axis because the free-rigid boundary conditions break the symmetry.

To further compare the results of modes A and B, we note from eq. 75 that $\bar{a}_1$ for the B modes is $-a_1$ for the A modes. Moreover, it follows from eq. 73 that $\bar{\zeta}_1 = \zeta_2$. This means that the Airy function arguments in layer 2 of figure 9, as a function of depth from the axis, is the same as these arguments in layer 1 of figure 13 as a function of depth from the surface. This property shows up for mode 1 in figures 9 and 13 but to little degree in modes 2 to 5. There are two reasons for this lack of comparison.

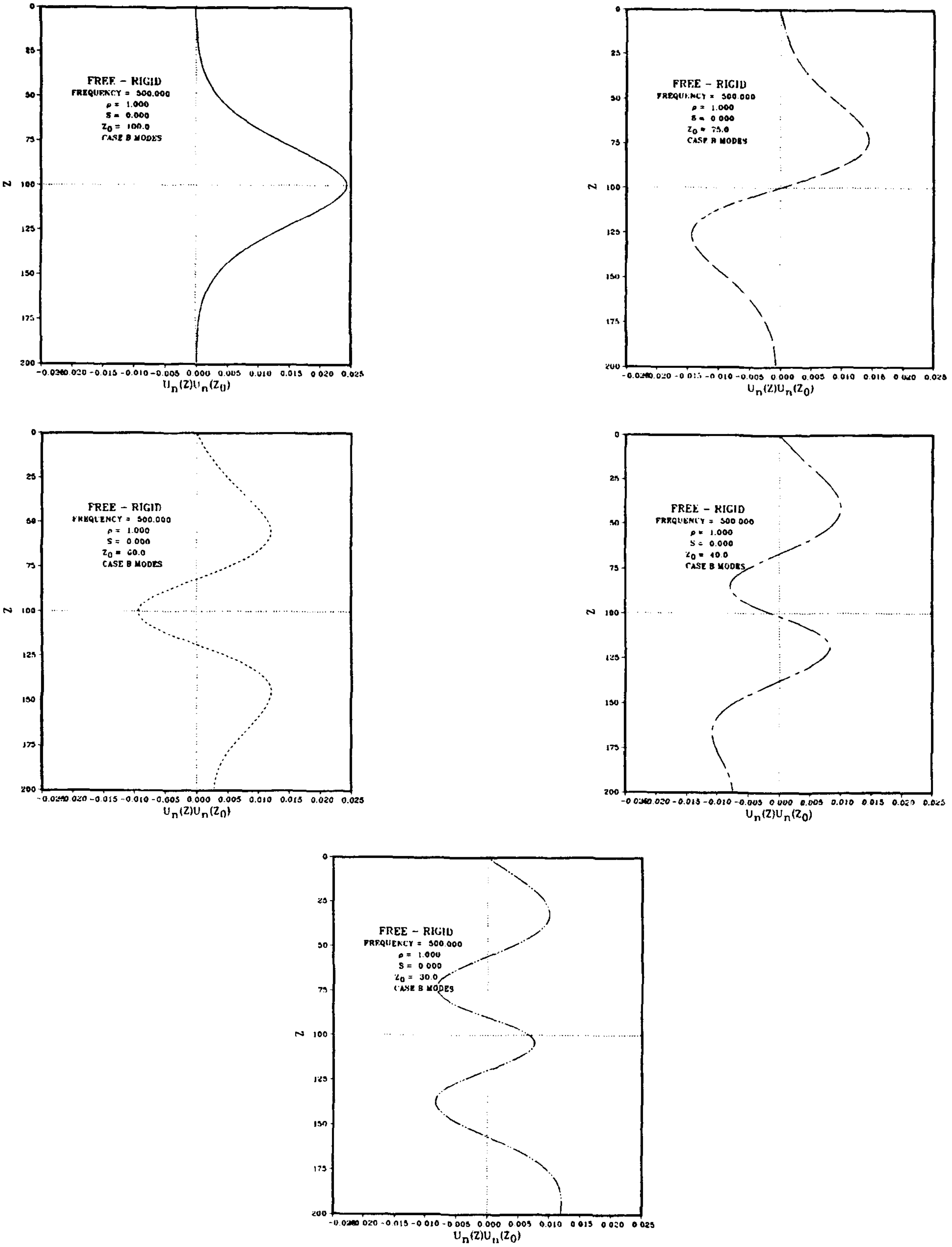

Figure 13. Eigenfunctions at 500 Hz for the B modes of figure 3.

The most important reason is that the coefficients $D_i$ and $E_i$ are different due to different requirements at the surface and axis. These coefficients weight the contribution of $Ai(-\zeta)$ and $Bi(-\zeta)$ in a different manner and produce a different response even though $\zeta$ is the same. A second reason is that the source depths are not the same for the A and B modes. This scales the amplitudes by a multiplication factor, but would not affect the shape as a function of depth.

One may also show that $\zeta_2 = \zeta_1$. Here, even mode 1 in the upper layer of figure 9 shows little resemblance to mode 1 in the lower layer of figure 13 because of radically different weighting of $D_i$ and $E_i$.

The important feature to note is that the eigenfunctions are radically different in figure 9 than those of figure 13. This occurs even though the eigenvalues are identical.

Our interest in comparing the cases A and B results stems from a classical mathematics problem that was the subject of a film produced by the American Mathematical Society entitled "Can You Hear the Shape of a Drum?" The film discussed the extent to which the environment could be inferred from the eigenvalues. This is related to the inversion problem in which physical properties of the environment are determined from acoustic field measurements of travel time.

Our example demonstrates that the eigenvalues (phase velocity versus frequency) do not uniquely determine the environment nor do the group velocity characteristics. On the other hand, the eigenfunctions (pressure field versus depth) are markedly different for the two environments. The problem of whether the eigenfunctions uniquely determine the environment will not be addressed here.

Our example of two radically different environments that produce identical group velocity characteristics suggests that measurements of travel time differences alone may not suffice to uniquely define the environment. This would be most likely in the case of long-range measurements where travel time differences are dominated by the group velocity characteristics.

## B. FREE-RIGID BOUNDARY, $\rho = 1.2$, $S = 0.5$

This case was chosen to illustrate the coupling phenomenon between double ducts. This case was presented at the 120th Meeting of the Acoustical Society of America described in reference 7.

Figure 14 presents the canonical eigenvalues. The B modes have horizontal asymptotes given by the solution to eq. 46. The A modes have two sets of asymptotes. The vertical asymptotes are given by eq. 40 and the slant asymptotes by eq. 42. The eigenvalue equation, eq. 28, is solved by iteration, using eq. 29 and iterating on x for the A modes and using eq. 30 and iterating on y for the B modes. The iteration is started at the horizontal asymptotes for large values of minus x for the B modes and at the vertical asymptotes for large values of minus y for the A modes.

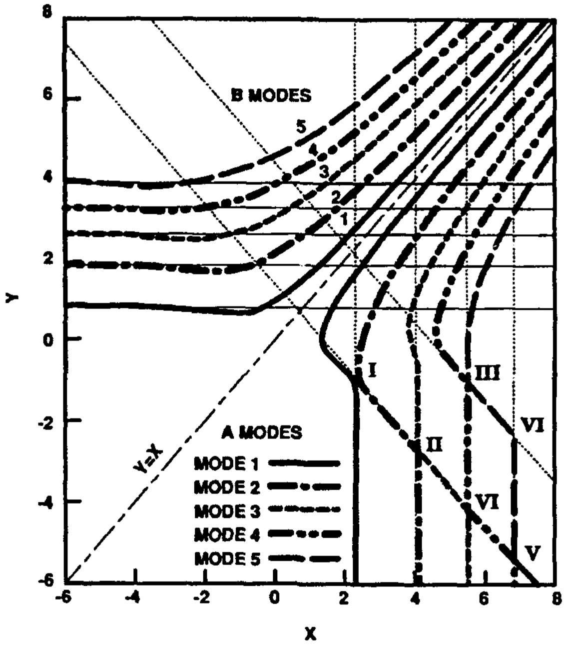

Figure 14. Eigenvalues for S = 0.5, ρ = 1.2, free-rigid boundary.

Consider now the A modes with y > 0. These are modes with phase velocities larger than the barrier sound speed. These modes correspond to rays reflecting off both the upper and lower boundaries. There are no coupling effects for these modes. We observe that here, the eigenvalues appear to be about evenly spaced as is the case with single ducts with no coupling. The eigenvalues for the B modes also show even spacing characteristics of modes in a single refractive duct with boundaries.

Our main interest here is in the A modes with y < 0. These modes correspond to modes trapped in either the upper or lower ducts. Modes trapped in the upper duct reflect from the surface and form a refractive nadir in the upper duct. These modes may be identified in figure 14 as those that follow the vertical asymptotes. Modes trapped in the lower duct reflect from the rigid bottom and form a refractive apex in the lower duct. These modes may be identified in figure 14 as those that follow the slant asymptotes.

Observe that in contrast to the B modes or the A modes with y > 0, the A modes for y < 0 have a highly variable spacing. This variability represents the main reason why the determination of modes in a double duct is so complicated as compared to that for regularly spaced modes in a single-duct configuration.

The intersection of the vertical with the slant asymptotes correspond to the critical frequencies. At or near these points the adjacent modes are transitioning from being trapped in the upper duct to being trapped in the lower duct and vice versa. The maximum coupling between upper and lower ducts occurs near these points. For ease of identification, these intersections have been identified by Roman numerals.

We note that the eigenvalue curves in figure 14 never cross each other. They come very close to each other near the intersection points. In general, the more negative the y of the intersection point, the closer the adjoining modes come together. Not all intersection points lead to critical frequencies. Critical frequencies do not occur when the y of the intersection point is positive. Examples in figure 14 are the intersection of slant asymptote two with vertical asymptotes one or two.

A higher order mode may have many critical frequencies associated with it. Consider for example mode 4 in figure 14. At large negative y, this is on upper duct mode. At critical point V, it transitions to a lower duct mode. At IV, it transitions back to an upper duct mode. At III, it transitions again to a lower duct mode.

We note that for sufficiently large negative y (high frequency) all modes start out as lower duct modes, i.e., start out on the vertical asymptotes. Since S is positive, $C_1$ in figure 1 is less than $C_3$. At sufficiently high frequency, the phase velocity for all modes goes to $C_1$ since it is less than $C_3$. Thus, at sufficiently high frequencies, any mode is an upper duct mode.

The eigenvalue solutions of figure 14 are not exclusive to underwater acoustics. They represent the solution to all equivalent physical problems with the same boundary conditions and canonical parameters. This plot could apply for example to air acoustics, seismic propagation, electromagnetics, solid state physics, and perhaps to quantum mechanics. The particular physical application only comes into play when we convert canonical functions into the physical solutions.

Figure 15 presents the sound-speed profile used in the evaluation of the various physical quantities of this section. The layer 1 parameters are the same as those discussed for the left panel of figure 3. These parameters and the values of $\rho$ and S completely determine the sound-speed profile.

Figure 16 presents the canonical frequency versus x corresponding to the eigenvalues of figure 14. The conversion to acoustical frequency is for the profile parameters of figure 15. Later on, eigenfunctions will be presented for the critical frequencies I, II, and III as well as for the frequencies of 500 and 900 Hz. The vertical portions of these curves correspond to modes trapped in the upper duct. Thus, modes 1 and 3 at 500 Hz and modes 1, 2, and 4 at 900 Hz are trapped in the upper duct. Portions of

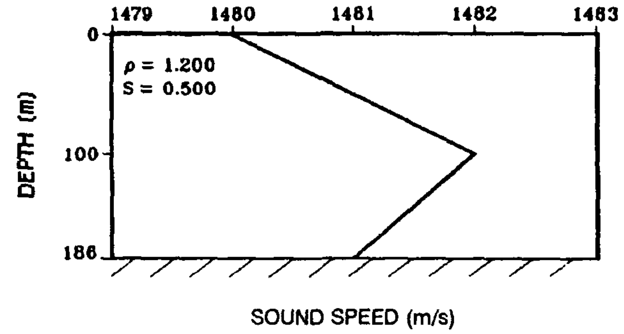

Figure 15. Sound-speed profile used in the analysis of the A modes of figure 14.

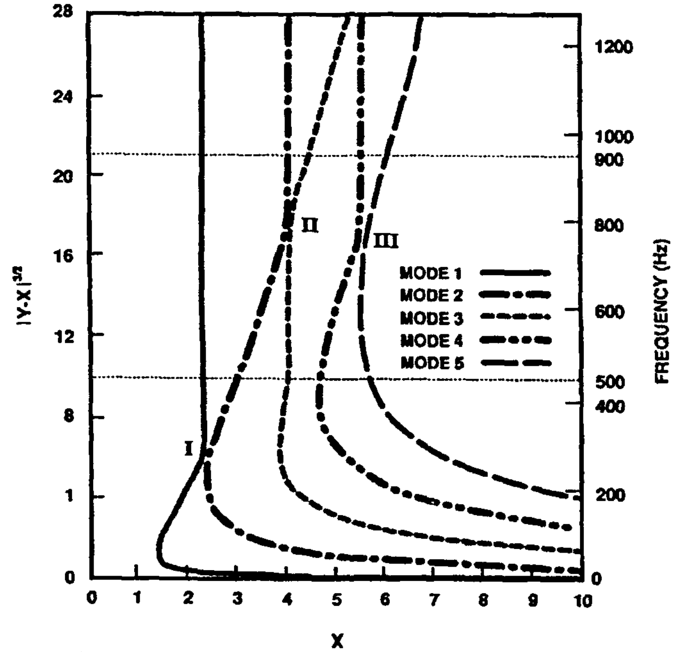

Figure 16. Canonical or acoustic frequencies for the A modes of figures 14 or 15.

the curves slanting from left to right correspond to modes trapped in the lower duct. Examples are modes 2 and 4 at 500 Hz and modes 3 and 5 at 900 Hz. Mode 5 at 500 Hz as well as other modes below the knee in the curves generally correspond to rays reflecting from both interfaces.

Figure 17 presents the phase velocity versus frequency. The modes with phase velocity less than the dotted line at 1482 m/s correspond to modes trapped in the upper or lower ducts. The phase velocities exhibit the characteristic pinching together at the critical frequencies I, II, and III. At sufficiently high frequencies, all modes will be trapped in the upper duct and will go to 1480 m/s as a limit. Modes trapped in the lower duct tend to a limit toward 1481 m/s, which is the bottom sound speed. Examples are mode 2 between frequency I and II and mode 3 beyond frequency II.

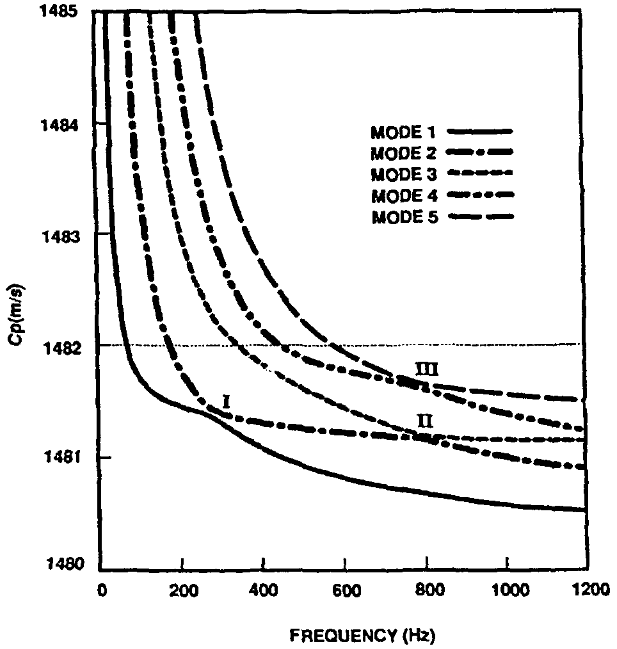

Figure 17. Phase velocities for the A modes of figure 15.

Figure 18 presents the canonical group velocity factor of eq. 58. It appears rather messy, but is just what is required to generate the group velocity curves about to be presented. The segments with near-constant value of 0.5 near the top of the plot are associated with the slant asymptotes of figure 14 having a constant slope of -1.

Figure 19 presents group velocity versus frequency. *At the critical frequencies, the* group velocities of adjacent modes cross each other. Group velocity is a much more sensitive indicator of the nature of the modes than is the phase velocity. Modes trapped in the upper duct tend toward 1480 m/s, the surface sound speed. Modes trapped in the lower duct have group velocities exceeding 1481 m/s, the bottom sound speed. The rapid drop in group velocities at the lower frequency end of the plot represents modes corresponding to rays reflecting from both boundaries. We note that figure 19 exhibits many points of Airy phase (extremes in the group velocity). The significance of the Airy phase as related to double-duct propagation is discussed on pages 41 and 42 of reference 4.

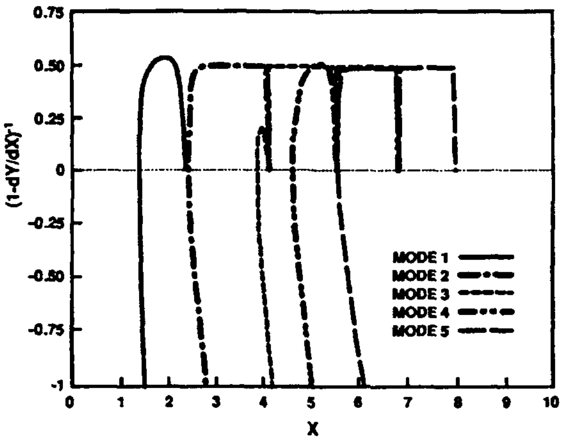

Figure 18. Group velocity factor for the A modes of figure 14.

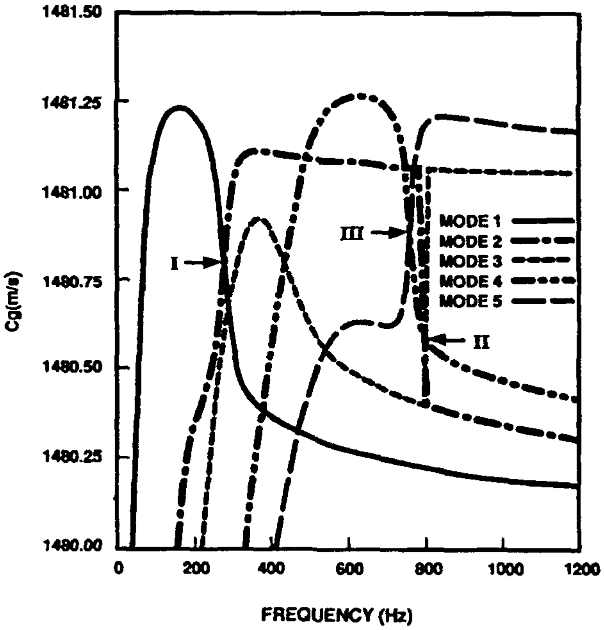

Figure 19. Group velocities for the A modes of figure 15.

Figure 20 presents the mode normalization coefficient. The left scale presents the canonical normalization factor. The right scale presents the normalization coefficients as obtained by scaling with the constant J of eq. 86. The bottom scale presents the canonical frequency. The top scale presents the acoustic frequency obtained with the use of the scale constant K of eq. 55. Observe that the curve for mode 2 goes off the top scale at a frequency of about 300 Hz and returns at a frequency of about 800 Hz. In this interval, this curve forms a relative maximum with $D_n = 8.9 \times 10^5$. This interval corresponds to the interval in figure 14 where the second mode is trapped in the lower duct. In our approach, we have chosen the unnormalized depth functions to automatically satisfy the boundary condition at the surface. This choice results in huge values for the normalization coefficient for modes when they are trapped in the lower duct. This does not present a problem with evaluating mode amplitudes, but only with the presentation of $D_n$ versus frequency on a single scale.

The curves go off scale for each mode when it is trapped in the lower duct. For example, the curve for mode 3 goes off scale near 800 Hz. Similarly, the curve for mode 5 is off scale between 800 and 1250 Hz. Aside from these relative maxima the curves have a consistent behavior. The normalization curves for all modes tend to zero at low frequencies. At high frequencies, all modes trapped in the upper duct appear to merge together in a common curve with a small negative slope.

The curves for adjacent modes cross each other at the critical frequencies. Thus, in figure 20 modes 1 and 2 cross at frequency I and modes 4 and 5 cross at frequency III.

Figure 21 presents the eigenfunctions at 500 Hz for modes 1 to 5. These are the normalized mode amplitude functions plotted as a function of receiver depth from the surface to the bottom at 186 m. The source depth is 45.4 m for modes 1, 3, and 5. Corresponding values for modes 2 and 4 are 185.9 and 140 m. The dotted horizontal line represents the interface between ducts at 99.8 m. The dotted vertical line is the zero axis for the amplitudes.

All mode amplitudes shown here and in similar figures to follow in this section have certain features in common. Because of the boundary conditions, all mode amplitudes have a node at the surface and a relative maximum at the bottom boundary. Moreover, the modes of order n all have n-1 zero crossings. These features are usually apparent in Figs. 21 and others to follow. In a few cases, the amplitudes are too small to see their features. In these cases, they have been verified by examining computer printouts of the numerical values.

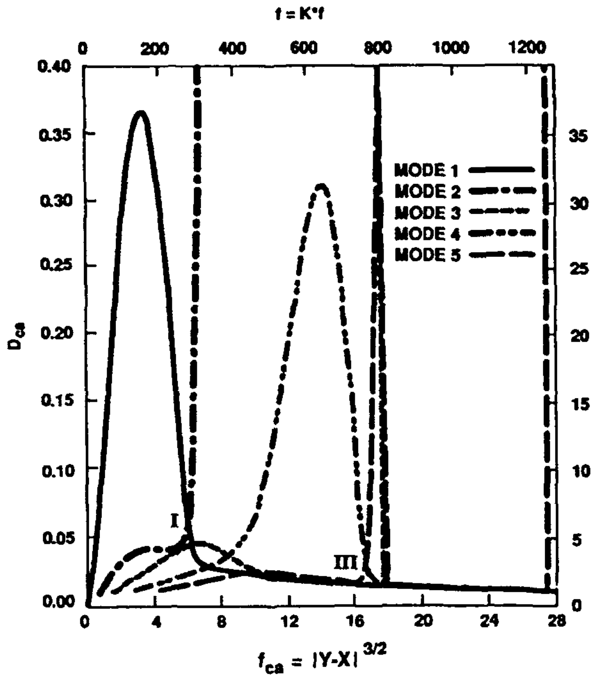

Figure 20. Canonical or customary eigenvalue normalization coefficients for the A modes of figures 14 or 15.

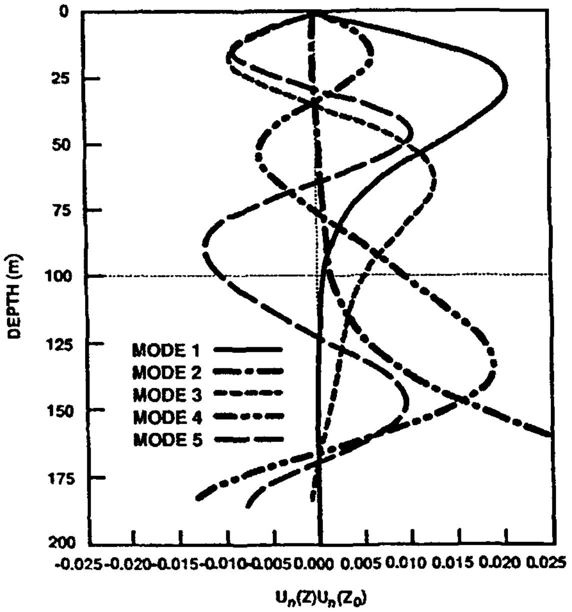

Figure 21. Eigenfunctions at 500 Hz for the A modes of figure 3.

Clearly, Figure 21 shows that modes 1 and 3 are trapped in the upper duct, whereas modes 2 and 4 are trapped in the lower duct. (We note that these results were predicted in the discussion of Figs. 16 and 14.) In this example, mode 5 has comparable amplitudes in both ducts. The y eigenvalue for mode 5 is positive. Thus, this mode corresponds to rays reflecting from both interfaces. This is of no particular interest in this paper. Our chief interest is in comparable amplitudes in the two ducts resulting from barrier penetration at the critical frequencies by the modes normally trapped in the individual ducts.

Figure 22 presents the eigenfunctions at 900 Hz for modes 2 to 5. We have not treated mode 1 highly trapped in the upper duct because of a problem with inadequate precision in the numerical evaluation. The source depths for modes 2 to 5 were respectively 45.4, 185.9, 60.0, and 185.9 m. These depths were chosen to enhance the mode amplitudes so that the features of the lower amplitudes could be shown. Clearly, modes 2 and 4 are upper duct modes, whereas modes 3 and 5 are lower duct modes as predicted in the discussion of figures 16 and 14. We note in all cases of trapped modes, the amplitudes are large in one duct but not in the other. Thus, the response for a source in one duct and receiver in the other duct is poor for trapped modes.

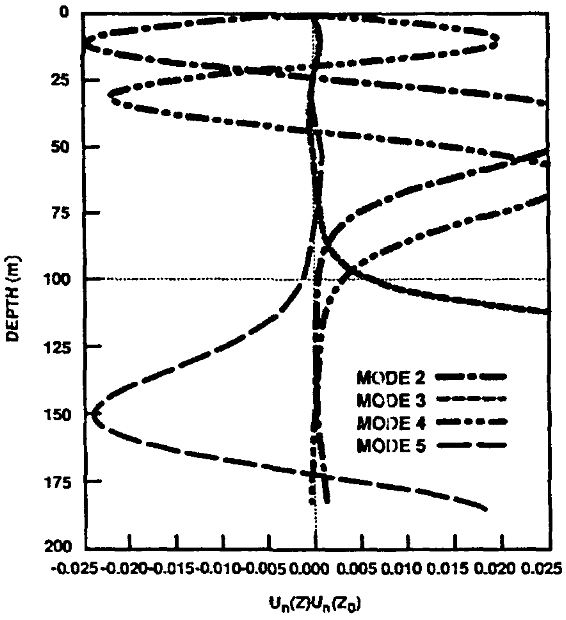

Figure 22. Eigenfunctions at 900 Hz for the A modes of figure 3.

We will now look at the mode amplitudes at the critical frequencies. These are frequencies where mode pairs are transitioning from being trapped in one duct to being trapped in the other duct. For these frequencies the amplitudes are comparable for the two ducts, even though the mode phase velocity is well below the barrier sound speed.

Figure 23 presents the eigenfunctions for modes 1 and 2 at 269 Hz, as associated with critical frequency I. The source depth is 39.4 m. The frequency of 269 Hz was determined empirically so as to match the amplitudes in the upper duct. The dashed curve is the result of folding over the negative portion of mode 2. In this example, there is a reasonably good match between the amplitudes of modes 1 and 2.

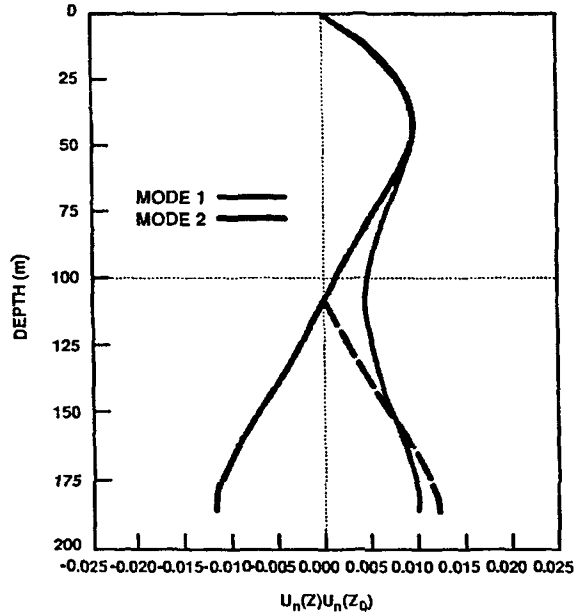

Figure 23. Eigenfunctions at 269 Hz (critical frequency I).

We note that in figures 21 and 22, the mode number is given by the number of antinodes. However, in figure 23, mode 1 has two antinodes. In this example and others to follow, in the regime about a critical frequency, the lower order mode will have an extra antinode. With a knowledge of the boundary conditions, the mode number may often be determined from the number of nodes or antinodes. However, near critical frequencies, an extra antinode is formed. Thus, the only fail-safe method is for the mode number to be always one more than the number of zero crossings.

The cross-duct propagation between mode 1 and 2 is enhanced by placing the source at the antinode in the upper layer and the receiver at the bottom of the lower layer. However, in this configuration, modes 1 and 2 are of opposite phase and will cancel each other at zero range. The modes will periodically reinforce each other at odd half multiples of the mode interference range and will cancel each other at even half multiples. This is true of the next two examples as well. The difference between the mode phase velocities for this example is 0.08569 m/s. At this frequency this translates to an interference range of 95.2 km as given by eq. 117. Figures 4-7 of reference 4 present examples of the interference patterns associated with a critical frequency.

Figure 24 presents the eigenfunctions for modes 4 and 5 at 758 Hz, as associated with critical frequency III. The source depth is 35.4 m. The dashed line is the result of folding over the mode 5 curve below the fourth node. Here, the match between the amplitudes of modes 4 and 5 is somewhat better than the match of figure 23.

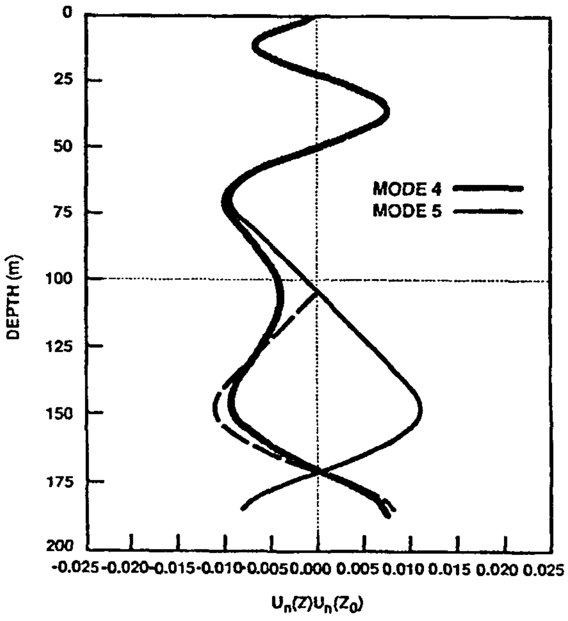

Figure 24. Eigenfunctions at 758 Hz (critical frequency III).

Optimum cross-duct propagation is obtained by placing the source at the third antinode in the upper duct and the receiver at the fourth antinode of mode 5 in the lower duct. Again, the modes are out of phase below the duct. The modes will again reinforce or cancel each other. The difference between the mode phase velocities is 0.02026 m/s, corresponding to an interference range of 143.0 km.

Figure 25 presents the eigenvalues for modes 2 and 3 near 799 Hz, as associated with critical frequency II. The source depth is 45.4 m. The dashed line is the result of folding over the mode 3 curve below the third node. Here, there is almost a perfect match between the eigenvalues because the phase velocities lie so close to each other. Orthogonality between the modes is preserved by the fact that the modes have opposite phase below the third node of mode 3.

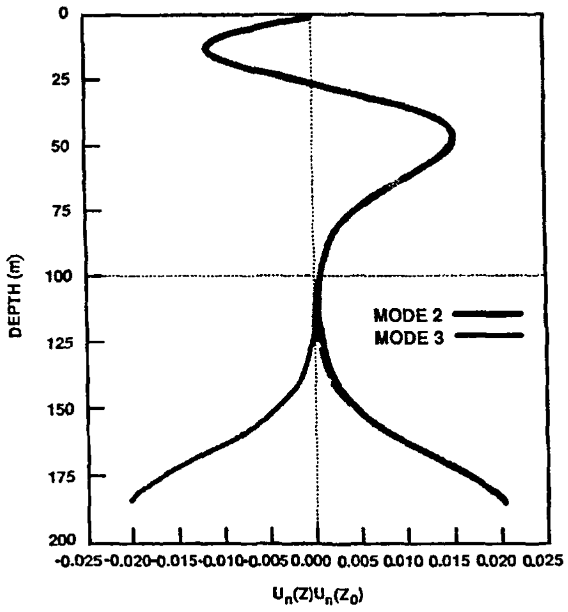

Figure 25. Eigenfunctions at 798.921 Hz (critical frequency II).

Optimum cross-duct propagation is obtained by placing the source at the second antinode in the upper duct and the receiver at the bottom of the lower layer. The difference between mode phase velocities is only 0.00012 m/s. This results in a whopping interference range of 2.3 x 104 km. Such closely coupled modes have been assessed in reference 4. When properly summed up, the two modes do not make a significant contribution to the propagation between the upper and lower ducts.

## C. FREE-FREE BOUNDARY, $\rho = 1, S = 0$

This section as well as the next three sections treat the case of $\rho = 0$, which occurs when the sound speed is the same at the upper and lower boundaries. This case is of particular interest because of past problems with the phase integral approach discussed in connection with eq. 68 and its free-free and rigid-rigid boundary counterparts. For the free-free boundary eq. 68 becomes

$$\rho^2 = a_m/a_n \ .$$

This section treats the case of $\rho = 1$, i.e., $m = n$. This is the case of all two-layer profiles symmetric about the interface between layers 1 and 2 and having both a free-surface and free-bottom condition. Figure 26 presents the canonical eigenvalues for this case. The method of designating modes and asymptotes has been changed from that of figure 2 and most other figures and the number of modes shown has been increased from 1 to 5 to 1 to 10. These changes are made to facilitate the analysis of section 3E for variable ρ. Rather than have a distinctive curve for modes 1 to 5 as in most figures, figure 26 displays the curves for odd modes by a long dash separated by a shorter dash. The even modes are shown by the curves with short dashes.

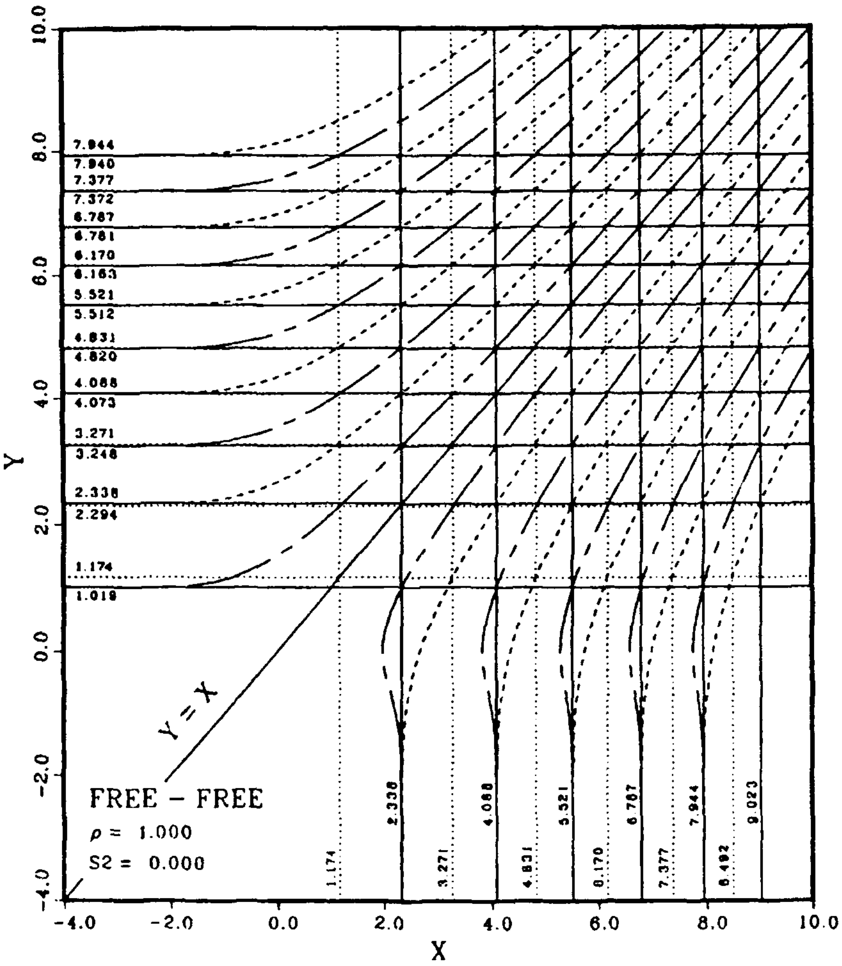

Figure 26. Eigenvalues for S = 0, ρ =1, free-free boundary.

There are three major differences from the free-rigid counterpart of figure 2. The most significant difference is that the two sets of vertical asymptotes of figure 3 collapse to one set in figure 26, given by the solid vertical lines. Thus, the modes do not go to separate asymptotes as in figure 2, but pairs of modes go to a common asymptote. The odd modes approach the asymptotes from the left, whereas the even modes approach from the right. Thus, the eigenvalues of modes 1 and 2, modes 3 and 4, etc.

have common values of $x = a_1, a_2$, etc. and $y = -\infty$. Physically, this means the eigenvalues converge at infinite frequency.

Another significant difference is that in figure 26, the line $y = x$ is a solution to the eigenvalue equation, whereas in figure 2, this line is not. Note that for values of x and y greater than about 1, the eigenvalue curves have almost uniform spacing. For example, the spacing between modes 1A and 2A is comparable to the spacing between mode 1A and $y = x$ or between modes 1B and 2B or between mode 1B and $y = x$. In contrast, in figure 2 the line $y = x$ is not a solution and the spacing between modes 1A and 1B is comparable to that between modes 1A and 2A and 1B and 2B. Thus, the status of the line $y = x$ explains the general location of the eigenvalues for mode 1. This explanation is not available in the conventional eigenvalue approach, where the A and B modes are treated as independent problems and the solution $y = x$ has no counterpart at all.

A third difference is the fact that the curves of figure 26 go through two sets of lattice points. One of these sets is given by the intersection of the solid grid lines, i.e., the solutions given by eq. 47. The other set is given by the intersection of the dotted grid lines, i.e., the solutions given by eq. 48. The points at $x = -\infty$ or $y = -\infty$, corresponding to the asymptotes, are lattice points for the solid grid, but not for the dotted grid. Notice that each lattice point lies on one of the modal curves or on the line $y = x$. Only one curve goes through each lattice point except for the solutions at $y = -\infty$.

There are no such lattice points in figure 2. This difference has no particular significance. In the case of the one-layer ducts of reference 2, all boundary conditions lead to eigenvalue curves with this lattice point property. In the case of two-layer ducts, only the case of figure 26 and the corresponding case with rigid-rigid boundary conditions (presented in section 3D) have lattice points.

We now proceed to evaluate the case A modes for the standard profile parameters used in Section 2A. The sound-speed profile is identical to case A of figure 3 except with a free rather than rigid bottom. Figures 27 to 32 are the free-free counterparts of figures 4 to 9. These modes are designated by the general identification scheme and do not follow the special scheme of figure 26. The curves of figures 27, 28, 30, and 31 merge together in pairs at high frequencies in contrast to their free-rigid counterparts in which all modes are well separated. The curves of figure 29 connect together in pairs in contrast to figure 6 where they remain distinct. We note that $D_n$ in figure 31 does not become very large as is the case for the odd modes of figure 8. This problem disappears when the boundary conditions are the same at the surface as at the bottom.

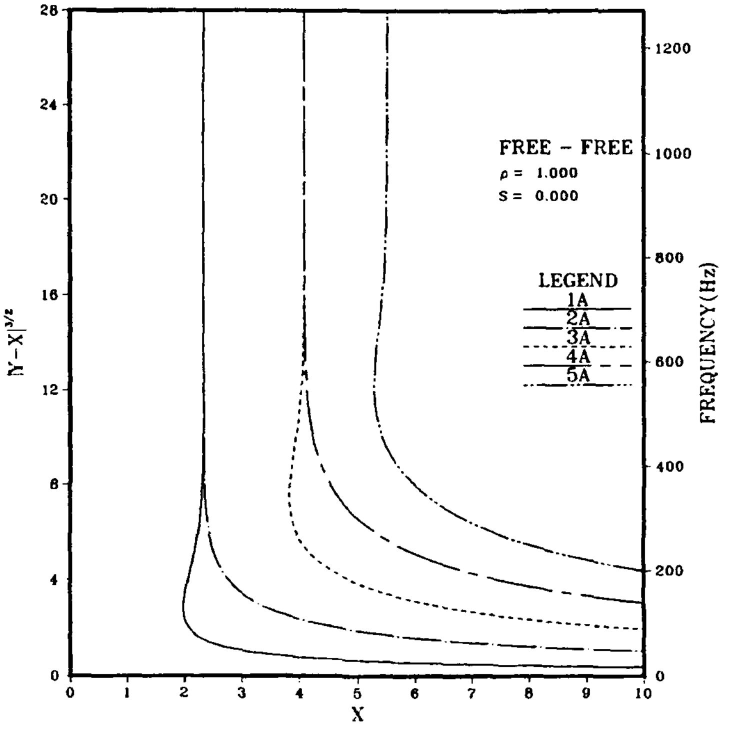

Figure 27. Canonical or acoustic frequencies for the A modes of figure 26.

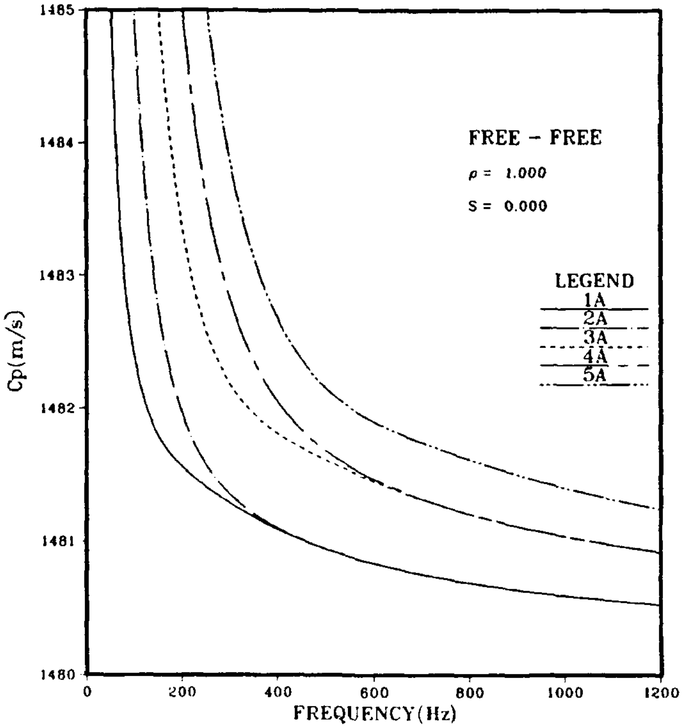

Figure 28. Phase velocities for the A modes of figure 26.

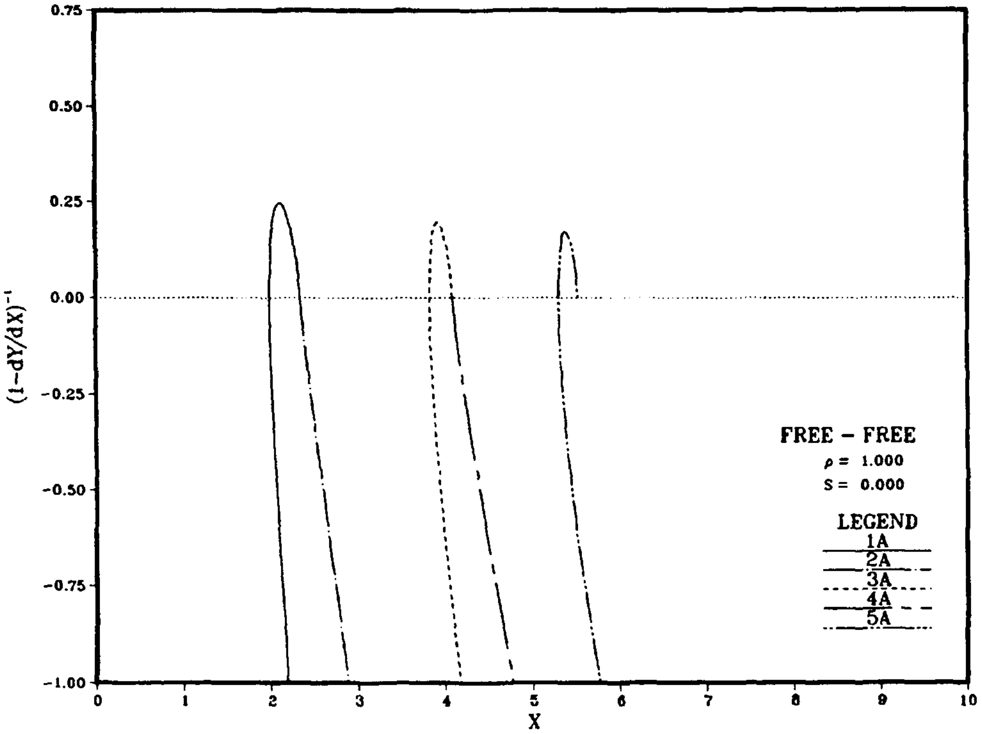

Figure 29. Group velocity factor for the A modes of figure 26.

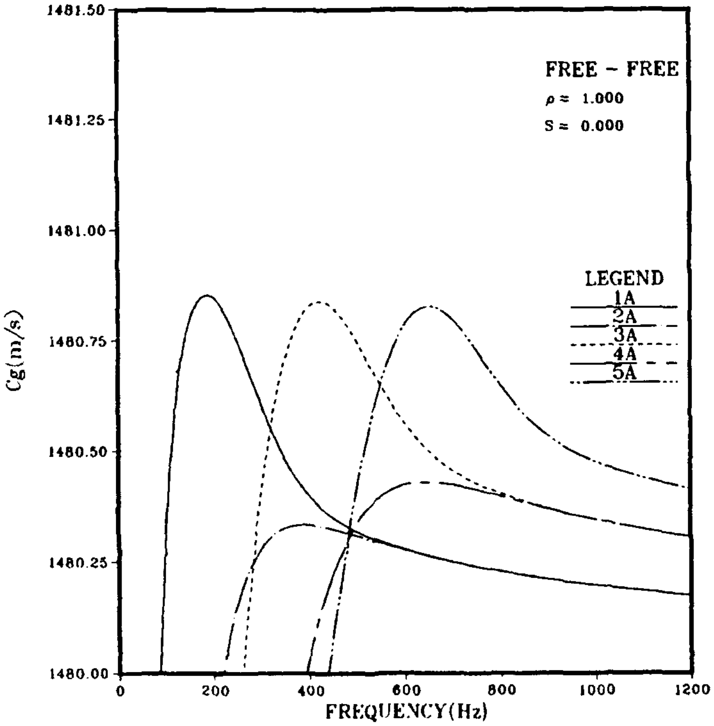

Figure 30. Group velocities for the A modes of figure 26.

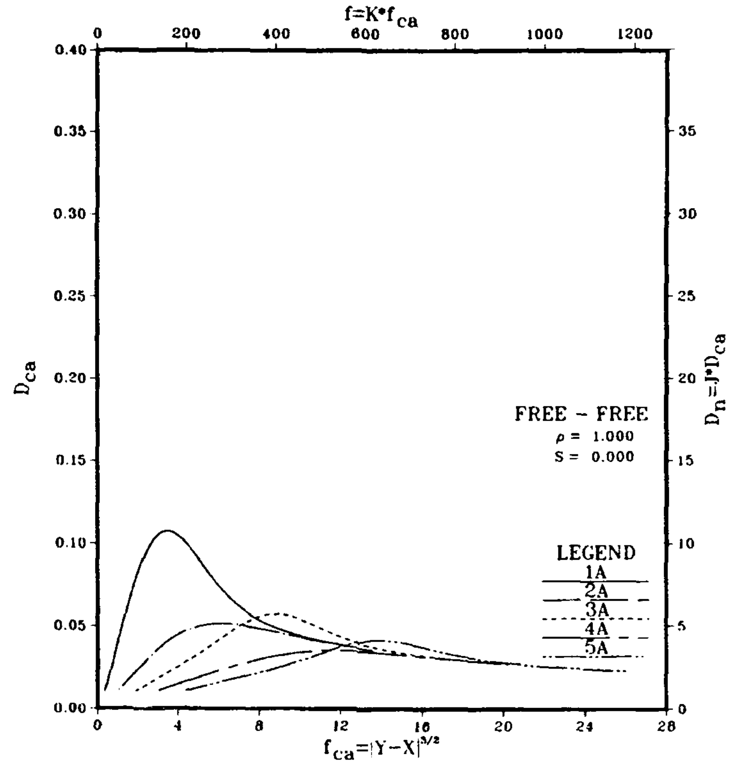

Figure 31. Canonical or customary eigenvalue normalization coefficients for the A modes of figure 26.

Figure 32 presents the eigenfunctions for modes 1 to 5 at a frequency of 500 Hz. The source depth is 25, 25, 60, 135, and 100 for modes 1 to 5 respectively. Again, the mode number is one more than the number of zero crossings. Here, the number of modes is n + 1 where n is the mode number. The number of antinodes is equal to the mode number for even modes and is equal to n + 1 for odd modes. We note that the eigenfunctions are symmetric about the interface between layers for odd modes and antisymmetric for even modes.

As can be seen in figure 32, there is a strong resemblance between the eigenfunctions for mode 1 and 2. As discussed in a later section, the coupling between the upper and lower duct at this frequency appears to be in line with other examples of critical frequency. While this example has coupling features in common with those of critical frequencies for $S \neq 0$, there are significant differences. When $S \neq 0$, there are critical frequencies for a given mode when paired with all other modes. In this case of $S = 0$, each odd mode is paired with the next higher even mode. There are no discrete critical frequencies as for $S \neq 0$. For each pair of odd-even modes the modes become coupled at sufficiently high frequency with the coupling increasing as the frequency is increased. At infinite frequency, the eigenvalues become identical for each pair of odd-even modes. An important feature is that these pairs have different eigenvalues for all finite frequencies. This is in marked contrast to the phase-integral method which predicts pairs with identical eigenvalues (degenerate modes) for all frequencies.

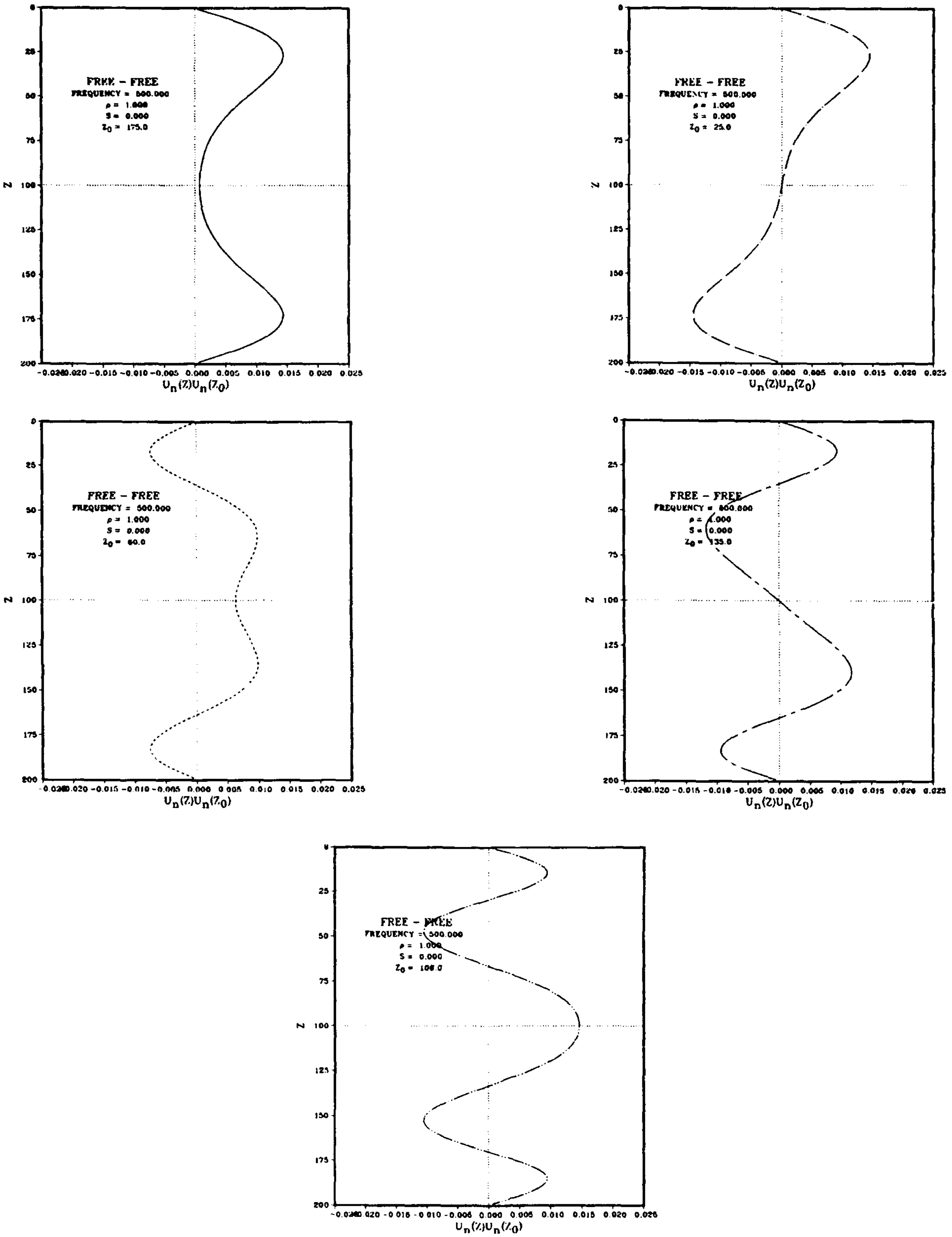

Figure 32. Eigenfunctions at 500 Hz for the A modes of figure 26.

## D. RIGID-RIGID BOUNDARY, ρ = 1, S = 0

This case is the rigid-rigid counterpart of the profile of section 3C and has many similar features. Figure 33 presents the eigenvalues. The special format is that discussed for figure 26. In this case, the common pair of vertical asymptotes are given by $x = a'_1$, $a'_2$, etc., rather than the $a_1$, $a_2$, etc. of figure 26. The line $y = x$ is a solution as in figure 26. The curves of figure 33 go through the lattices points of eq. 49 (solid lines) or 50 (dotted lines) rather than those of eqs. 47 or 48 in figure 26.

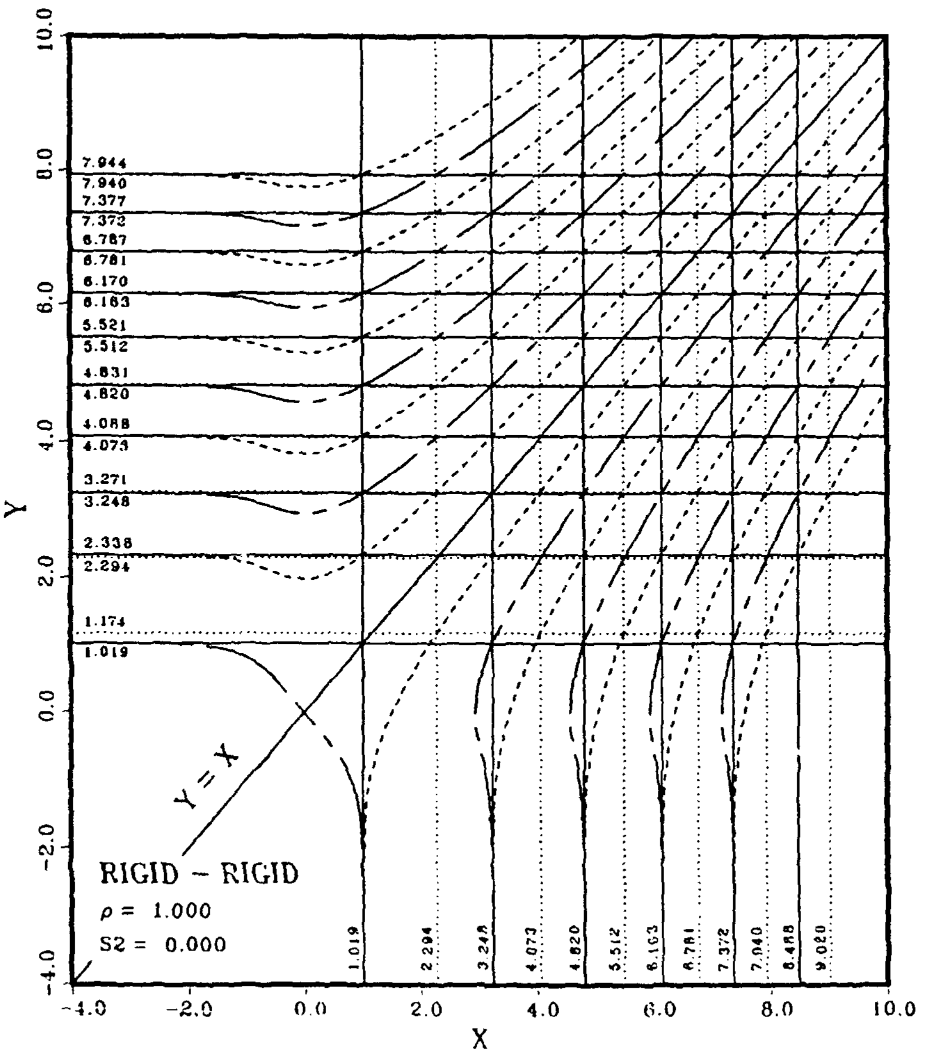

Figure 33. Eigenvalues for S = 0, ρ = 1, rigid-rigid boundary.

The most significant difference between figure 33 and figure 26 is the peculiar behavior of mode 1 in figure 33. Here, mode 1A connects with mode 1B at x = 0, y = 0. This behavior occurs for all profiles with rigid-rigid boundary conditions. This case is analyzed in detail in the discussion of figure 4 of reference 3, which treats the single layer case. The chief characteristic is that mode 1A or 1B for the rigid-rigid boundary condition only exists for refracted rays. This condition does not exist for rays reflecting from both boundaries.

Figure 34 presents the canonical or acoustic frequency plot. The distinctive difference from figure 27 is that mode 1 in figure 34 has no lower cutoff frequency as do the other modes. The chief difference between the phase velocities of figure 35 and those of figure 28 is that the phase velocity of mode 1 in figure 35 does not go to infinity for low frequencies by approaches a constant value as f goes to zero. This constant value is given by eq. 36 of reference 3 and is the square root of the harmonic mean of the square of $C_1$ and $C_2$. This is very slightly less than the mean of $C_1$ and $C_2$, which in this case is 1481 m/s.

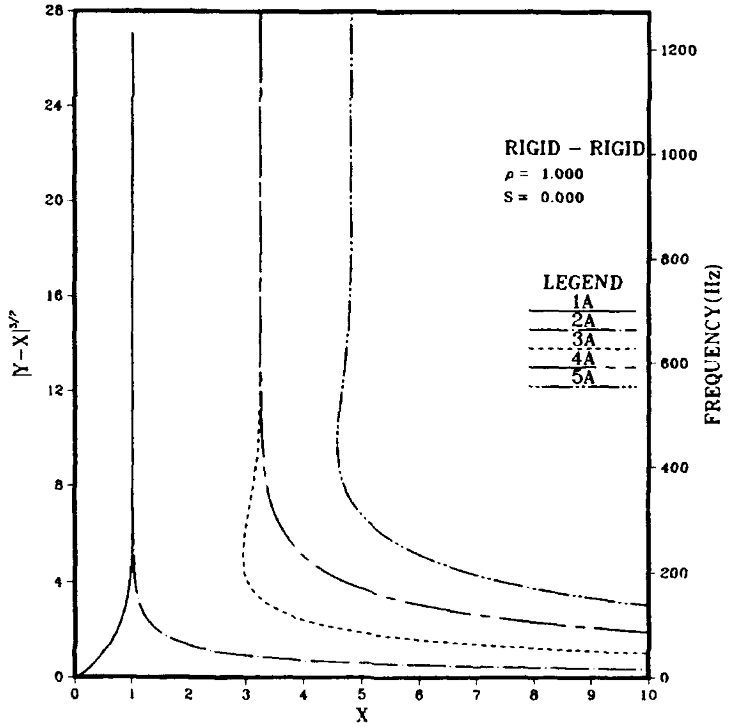

Figure 34. Canonical or acoustic frequencies for the A modes of figure 33.

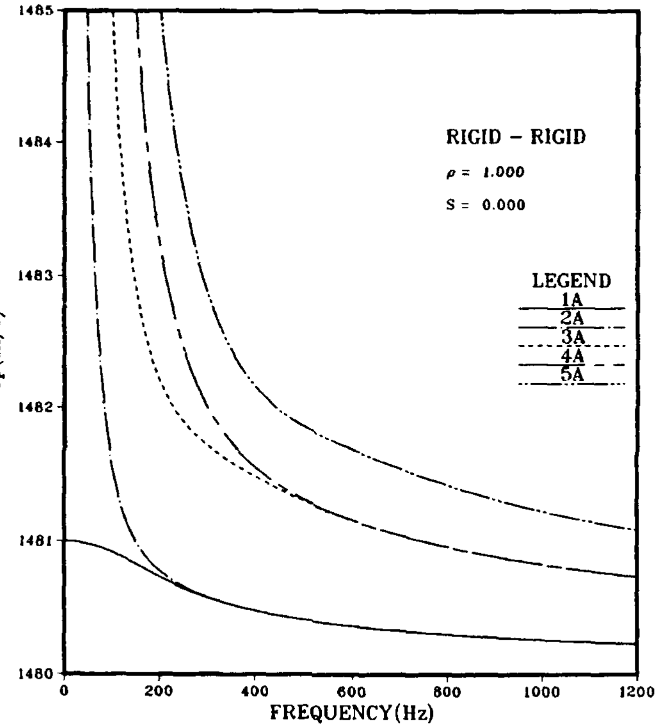

Figure 35. Phase velocities for the A modes of figure 33.

Figure 36 for the canonical group velocity factor is similar to figure 29 with the exception of mode 1. It does not go to large negative values for small x but goes to 0.5 as x goes to zero. The analyses of reference 3 notes that the slope of mode 1 at the origin in figure 33 is -1. This makes the group velocity factor equal to $2^{-1}$.

Figure 37 for the group velocity is similar to figure 30 with the exception of mode 1. As f goes to zero the group velocity does not go to zero as for other modes, but goes to a constant that is the same as the limit of phase velocity of figure 35.

Figure 38 for the eigenvalue normalization coefficient is quite different from figure 31. In figure 31 the coefficient goes to zero at low frequencies and that for all modes merges at the higher frequencies. In figure 38, mode 1 goes to one constant at zero frequency while all other modes go to another constant. This same behavior is observed for the A modes in figure 22 of reference 3. Indeed reference 3 demonstrates that the limits for mode 1 are $\pi^{-2} = 0.101$ and $2\pi^{-2} = 0.202$. In figure 38 the modes merge in pairs at higher frequencies. However, the pairs do not also merge as in figure 31. This is similar to the case of figure 22 of reference 3 in which none of the A modes have merged, at least for the frequency range shown.

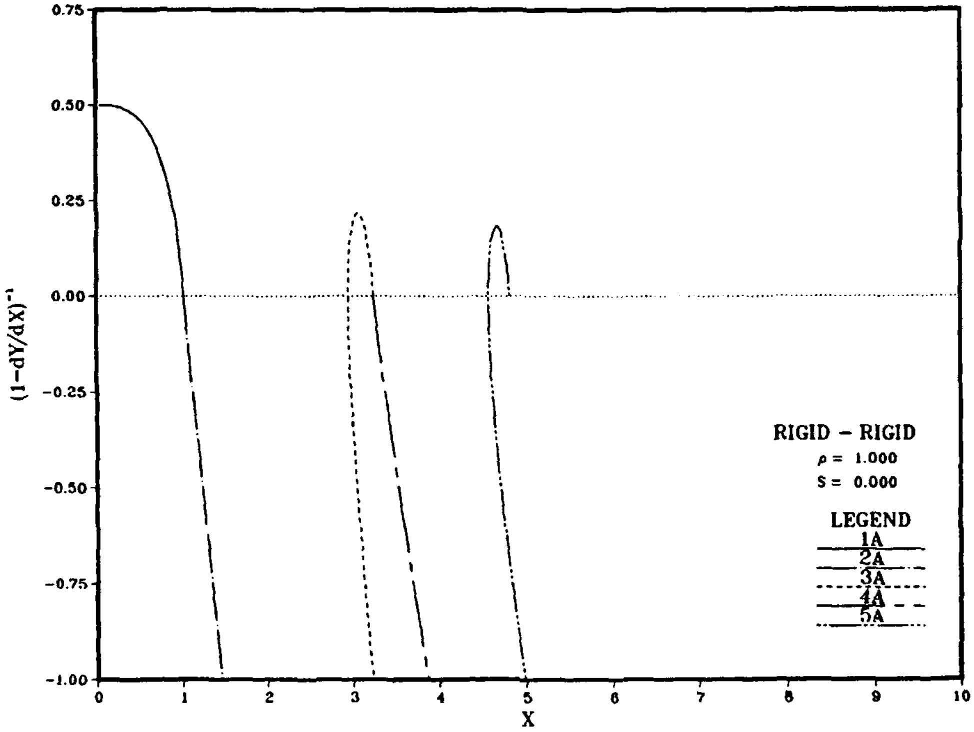

Figure 36. Group velocity factor for the A modes of figure 33.

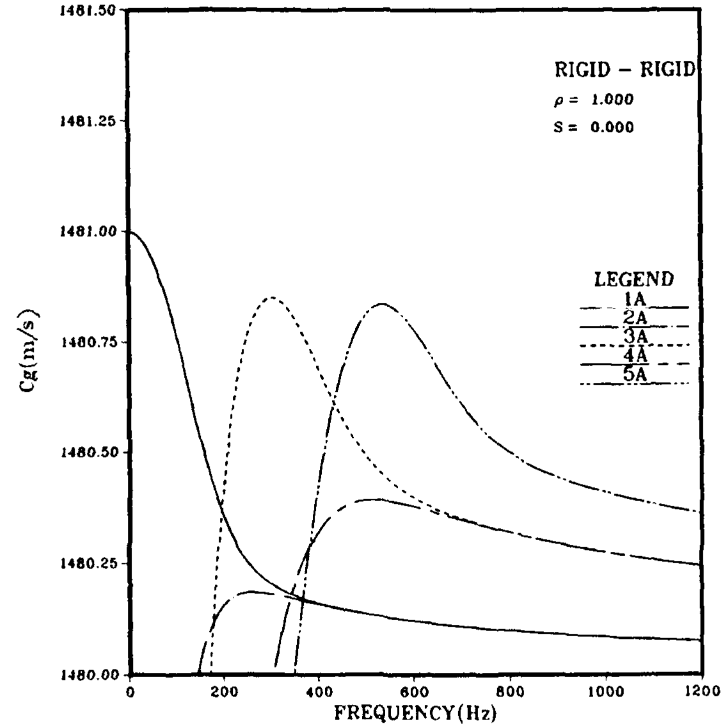

Figure 37. Group velocities for the A modes of figure 33.

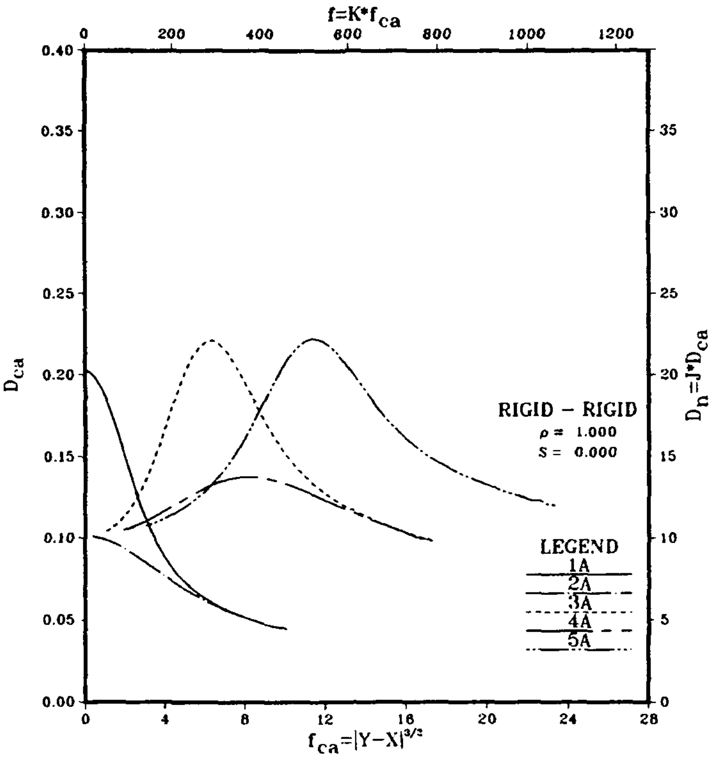

Figure 38. Canonical or customary eigenvalue normalization coefficient for the A modes of figure 33.

Figure 39 presents the eigenfunctions for modes 1 to 5 at a frequency of 400 Hz. The source depth is 5, 5, 50, 50, and 100 for modes 1 to 5 respectively. Again, the mode number is one more than the number of zero crossing. The number of nodes is one less than the mode number. The number of antinodes is n + 1 for odd modes and is equal to n for even modes. As was the case of figure 32, the eigenfunction are symmetric about the interface between layers for odd modes and antisymmetric for even modes.

The general characteristics are essentially the same as those discussed in the last paragraph of section 3C.

## E. EIGENVALUES FOR FREE-FREE BOUNDARY, VARIABLE $\rho$, S = 0

In this section, we determine the behavior of the eigenvalue curves for $S = 0$ as we let $\rho$ decrease or increase from $\rho = 1$. We chose the free-free boundary condition for illustrative purposes as once this is available, the situation for other boundary conditions can be easily inferred.

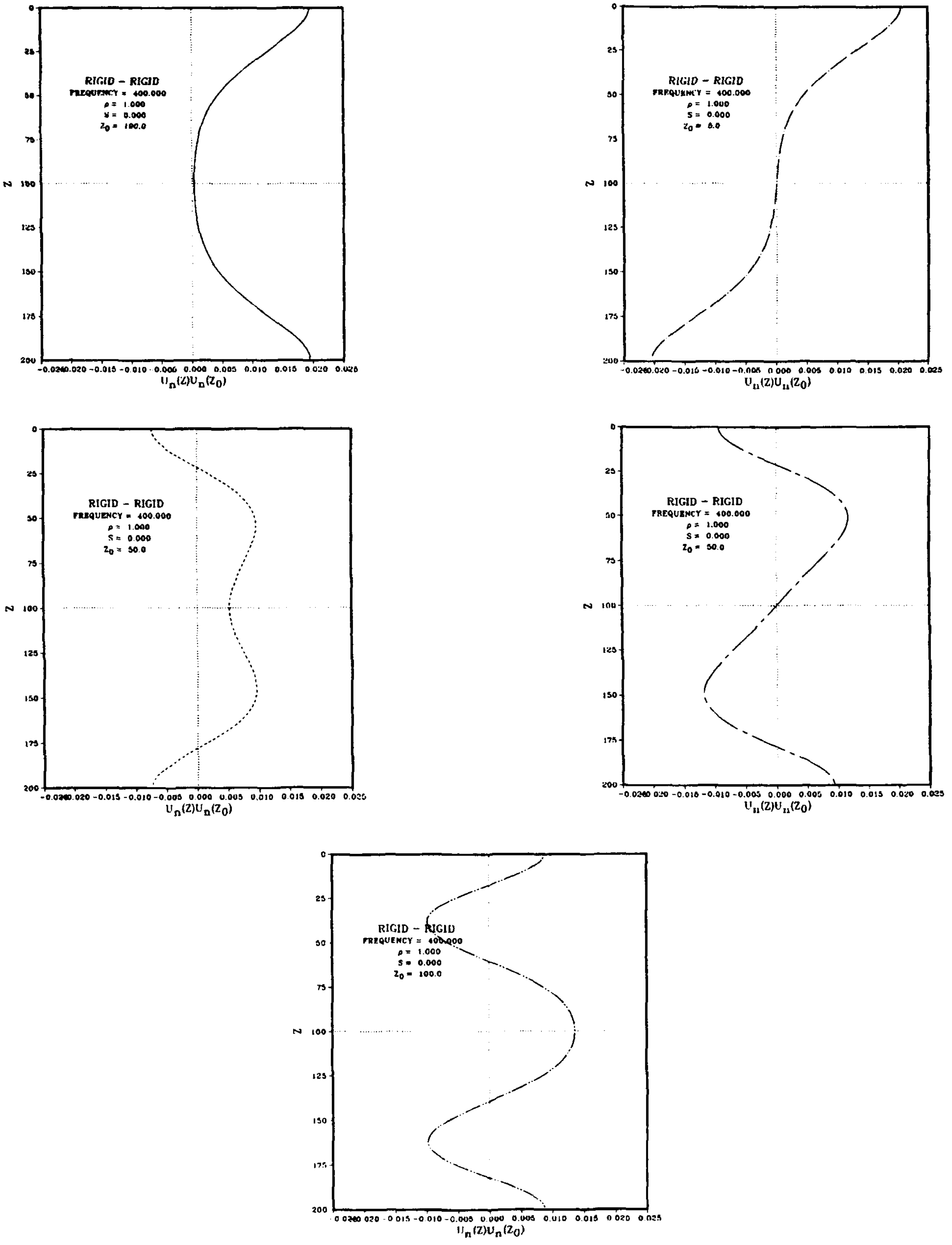

Figure 39. Eigenfunctions at 400 Hz for the A modes of figure 33.

Figure 40 presents the eigenvalues for $\rho = 0.99$. The format is similar to that of figure 26. The dotted grid lines of figure 26 are deleted because there are no lattice point solutions for $\rho \neq 1$. There are two sets of vertical asymptotes in figure 40 as compared to the one set of figure 26. The solid vertical asymptotes are the same as those of figure 25, i.e., $x = a_n$. The eigenvalues for the odd-order modes of figure 40 are almost the same as those of figure 26 because the vertical asymptotes for the odd modes remains unchanged for different ρ. The vertical asymptotes for the even-order modes of figure 40 are shown by the dotted vertical lines as given by $x = a_n/\rho^2$. The displacement between the sets of asymptotes for odd and even modes is given by $\Delta x = a_n(1 - \rho^{-2})$. Thus, for a given value of $\rho^2$ this displacement increases with increasing mode number since an increases with mode number. If ρ is decreased further below 1, the even modes will march further to the right than illustrated in figure 40.

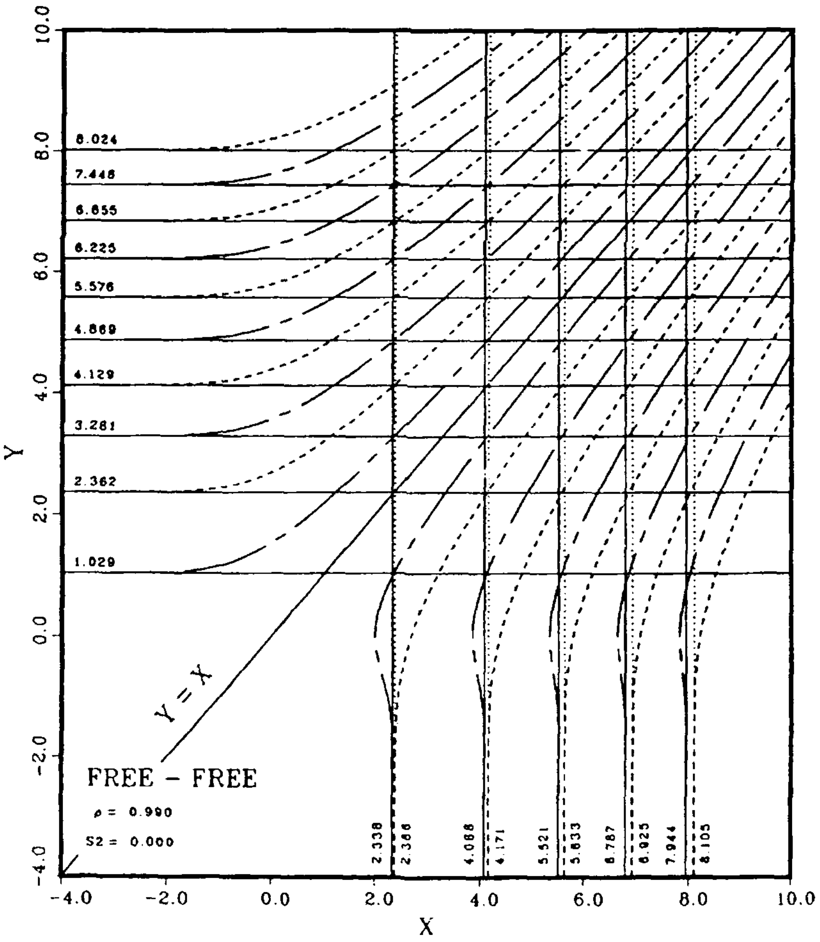

Figure 40. Eigenvalues for S = 0, ρ = 0.99, free-free boundary.

Next, we examined a value of $\rho = 1.01$. On the basis of figure 40 and other smaller values of $\rho$ we assumed that the odd modes would still remain fixed and that the even modes would march to the left. We were looking forward to the possibility of the even mode eigenvalue crossing the odd mode eigenvalues and producing degenerate eigenvalues. However, as shown in figure 41, this does not occur. In figure 41, the roles of even and odd modes reversed at $\rho = 1$ and as $\rho$ is increased above one the even mode asymptotes remain fixed at $x = a_n$, whereas the odd mode asymptotes march to the left according to $x = a_n/\rho^2$.

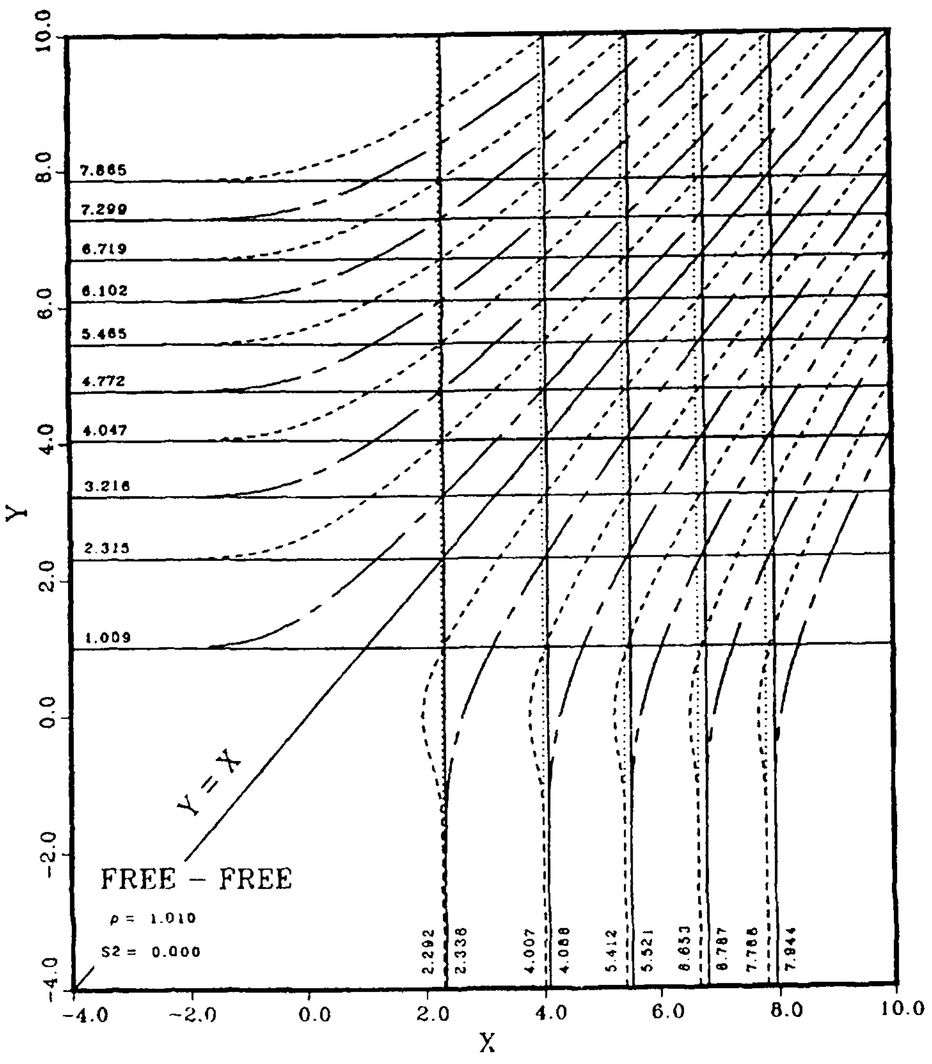

Figure 41. Eigenvalues for $S = 0$, $\rho = 1.01$, free-free boundary.

Next, consider what happens for even larger values of ρ. Figure 42 presents the eigenvalues for $\rho = 1.515$. Here, the dashed lines correspond to the variable symptotes, where the long dashed lines correspond to the fixed asymptotes. The salient feature here is that the fixed vertical asymptotes of $x = a_1$ and $x = a_2$ are occupied by modes 3 and 8 respectively, whereas modes 1, 2, 4 to 7, 9, and 10 have asymptotes at $x = a_n/\rho^2$ for n = 1 to 8 respectively. To explain the results of figure 42, we first examine where the asymptotes of mode 2n + 1 in figure 41 first encounter mode 2n as ρ is increased above 1.01. This solution is given by $\rho^2 = a_{n+1}/a_n$. Thus, modes 3 and 2 will have a common asymptote at $x = 2.338$ when $\rho = 1.3222712$.

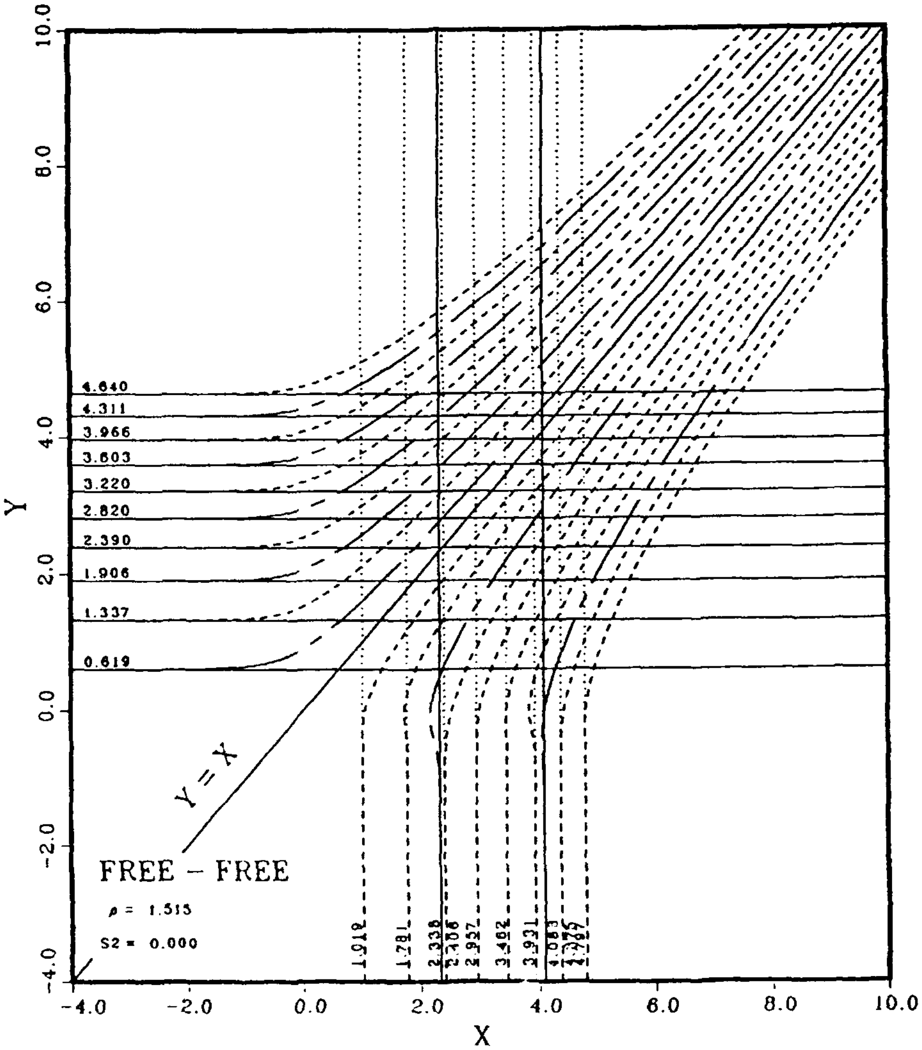

Figure 42. Eigenvalues for $S = 0$, $\rho = 1.515$, free-free boundary.

As $\rho$ is increased above 1.01, i.e., the case of figure 41, mode 2 remains fixed at 2.338 and mode 3 moves to the left until $\rho = 1.3222712$. As $\rho$ is further increased, mode 3 now remains fixed at 2.338 while mode 2 continues to move to the left as in the case of $\rho = 1.515$ in figure 42. When $\rho^2 = 5.521/2.338$ or $\rho = 1.537$, modes 3 and 4 will have a common asymptote at 2.338 and as $\rho$ increases beyond 1.537, mode 4 will remain fixed at 2.338 while mode 3 moves to the left.

In figure 42, we see that mode 8 corresponds to the fixed asymptote at 4.088. Mode 8 took over this asymptote when $\rho^2 = a_6/a_2$ or $\rho = 1.486$. Mode 9 will take over this asymptote when $\rho^2 = a_7/a_2$ or $\rho = 1.567$.

A similar situation occurs when $\rho$ is decreased further from the value of 0.990 in figure 40. The asymptotes of mode 2n first encounters mode 2n + 1 when $\rho^2 = a_n/a_{n+1}$. Thus, mode 2 will have a common asymptote at $x = 4.088$ when $\rho^2 = 2.338/4.088$ or $\rho = 0.756$. This is the reciprocal of the value of $\rho$ for which mode 3 moves to mode 2 in figure 41. The salient feature is that the mode eigenvalues never cross each other. For special values of $\rho$ they have a common asymptote, i.e., they touch each other at $y = -\infty$ corresponding to infinite frequency. As the value of $\rho$ is increased from these special values, one asymptote remains fixed while the other moves to the left. As the value of $\rho$ is decreased from these special values, one asymptote remains fixed while the other moves to the right.

A similar type of behavior occurs for the rigid-rigid boundary condition. The only difference is that the asymptotes are associated with $a_n'$ rather than $a_n$.

The behavior for variable $\rho$ for the free-rigid boundary conditions is similar to that of the free-free and rigid-rigid boundary conditions. As $\rho$ is increased from the special values given by eq. 71, one asymptote remains fixed while the other moves to the right. The significant difference for the free-rigid condition is that $\rho = 1$ is not a special value as for the free-free and rigid-rigid conditions. Indeed, the maximum separation for mode eigenvalues occur for $\rho = 1$ as illustrated by figure 2.

It is of interest to examine what happens as $\rho$ goes to its limiting values. The same behavior applies to all three boundary conditions. We have no interest in negative $\rho$ because this does not represent a double-duct case. As $\rho$ decreases from 1 to zero as a limit, the variable asymptotes correspond to the higher order modes and all march out toward $x = \infty$, leaving the fixed asymptotes to the lower order modes. As $\rho$ is increased from 1 to $\infty$ as a limit, the variable asymptotes correspond to the low-order modes and all march toward $x = 0$, leaving the fixed asymptotes to the high-order modes.

### F. FREE-RIGID BOUNDARY, $\rho = 0.6601015$, S = 0.

For this example, $\rho$ satisfies eq. 68 with m and n = 1. This is a case where modes 1 and 2 have a common vertical asymptote of $x = 2.338$.

This example was prompted by an earlier investigation of a positive-gradient surface duct overlaying a symmetric refractive duct where the surface and axial sound speeds were the same. This investigation has already been introduced in the discussion of eq. 69, which gives the relationship between gradients designed to superimpose the eigenvalues for mode 1 of the two ducts. The unpublished results of this investigation displayed an unexpected result. At 400 Hz, the phase velocities for modes 1 and 2 differed by only 2.9 x $10^{-6}$ m/s. However, there were large differences in the eigenfunctions. The mode 2 peak in the upper duct had 45 dB less loss than the mode 1 peak. Similarly, the mode 1 peak in the lower duct had 47 dB less loss than the mode 2 peak.

The motivation here is to examine a case where modes 1 and 2 have a common asymptote. The cases of sections 3C and 3D have this property. However, modes 1 and 2 strongly resemble each other in figures 32 and 39. Thus, we turn to the case where modes 1 and 2 have a common asymptote for the free-rigid boundary.

Figure 43 presents the canonical eigenvalues. Figure 44 gives the sound-speed profile. Figures 45 to 49 give the results for frequency, phase and group velocity, and normalization coefficients. The mode 1 and 2 results of figures 43, 45, 46, 47, and 48 are in general qualitative agreement with the results of figures 26 to 30 respectively for the free-free profile. Moreover, the results of figures 46 and 48 are in general agreement with the phase and group velocity plots of reference 6, i.e., the results of the earlier investigation under question.

The first clue that there is a significant difference is figure 49. Whereas modes 1 and 2 merge at high frequencies in figure 31, they do not do so in figure 49. Indeed, computer printouts for the higher frequencies in figure 49 indicate that the mode 1 values continue to get larger with increasing frequency until computer roundoff problems set in. Thus, we are not certain that $D_{ca}$ for mode 1 remains bounded let alone that is merges with the relatively small values for mode 2.

Figure 50 presents the eigenfunctions for modes 1 and 2 at 800 Hz. The source depth is 25 m . The difference in the phase velocity of modes 1 and 2 is 0.0061 m/s. We see that at this frequency mode 1 is trapped in the upper duct and mode 2 is trapped in the lower duct.

We next upped the frequency to bring the phase velocities differences closer with the idea of bringing the eigenfunctions into better agreement. Figure 51 presents the eigenfunction for 1000 Hz. Here the difference in the phase velocity is 0.00012 m/s. However the amplitude of mode 1 in the upper layer is even smaller than in figure 50. Detailed computer printouts indicate that the mode 1 antinode in the upper layer has a value of 0.299 x $10^{-4}$. This is 62 dB below the mode 2 antinode in the upper layer.

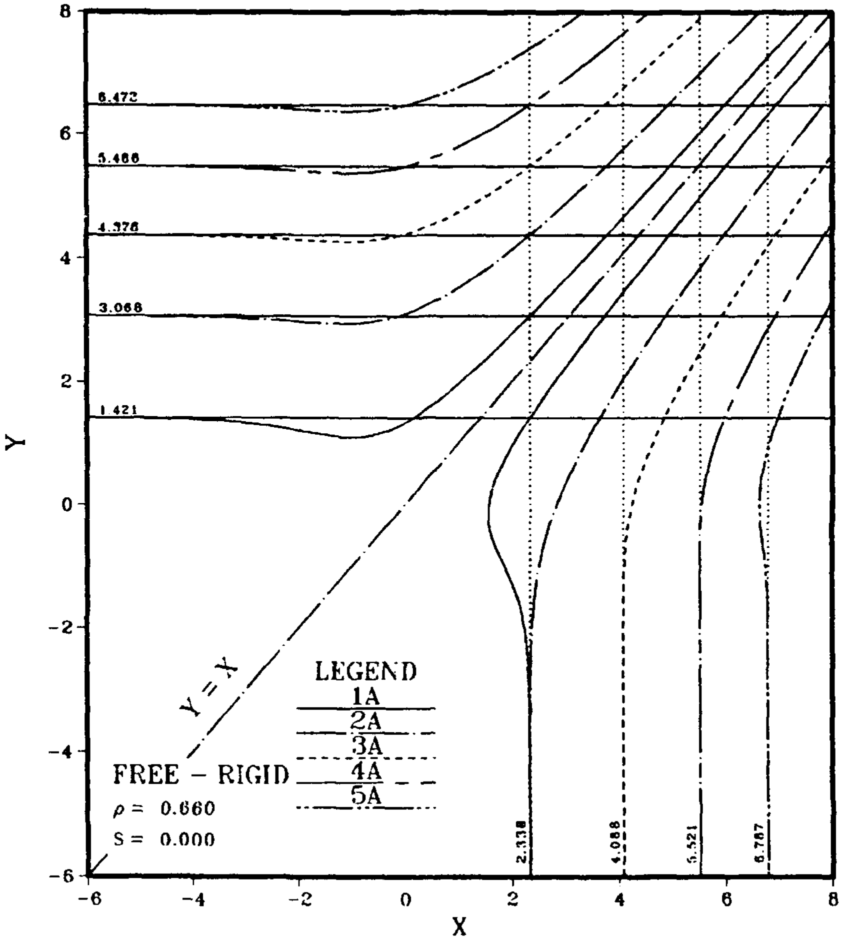

Figure 43. Eigenvalues for S = 0, ρ = 0.6601015, free-rigid boundary.

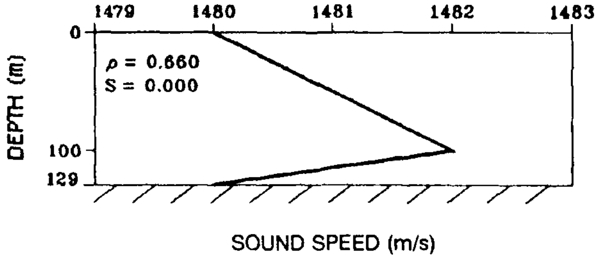

Figure 44. Sound-speed profile used for the analysis of the A modes of figure 43.

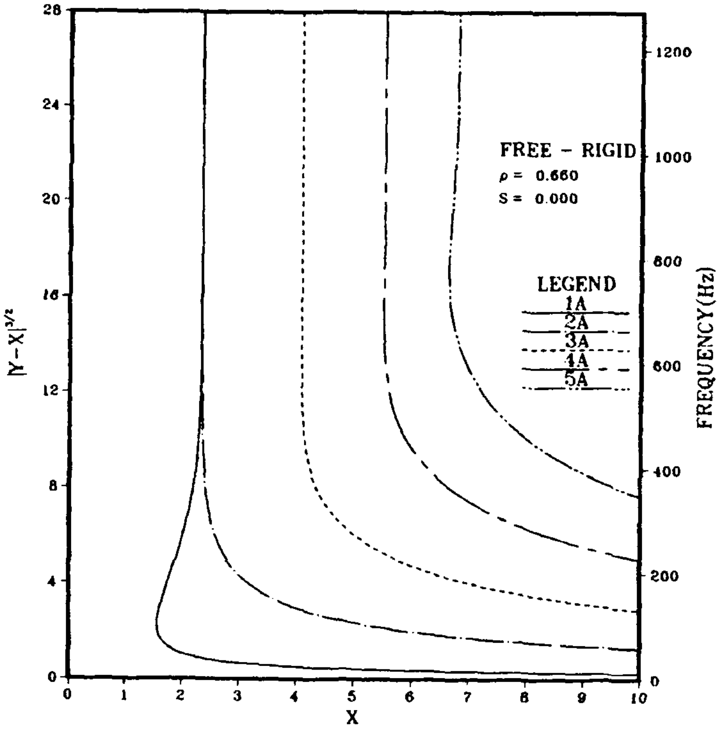

Figure 45. Canonical or acoustic frequencies for the A modes of figure 43.

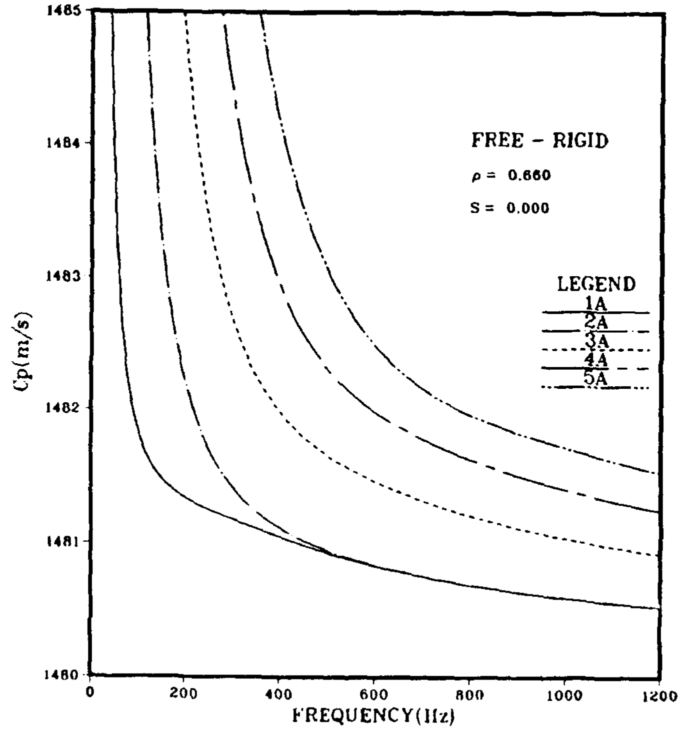

Figure 46. Phase velocities for A modes of figure 43.

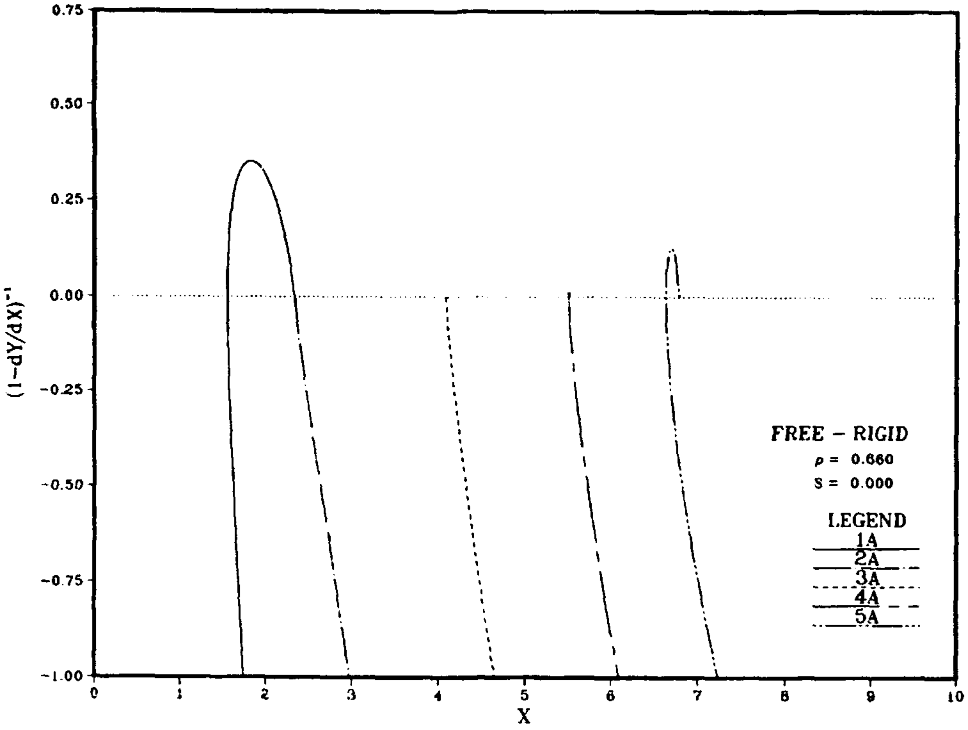

Figure 47. Group velocity factor for the A modes of figure 43.

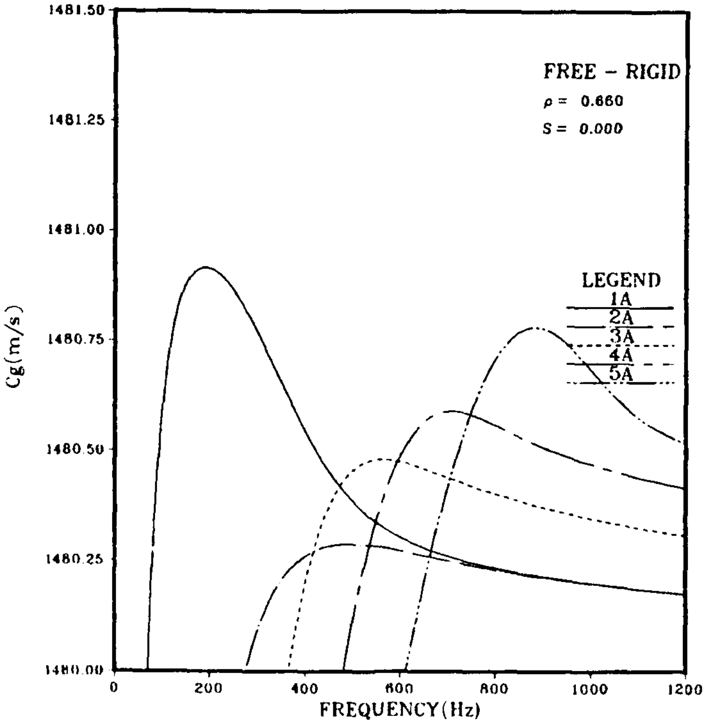

Figure 48. Group velocities for the A modes of figure 43.

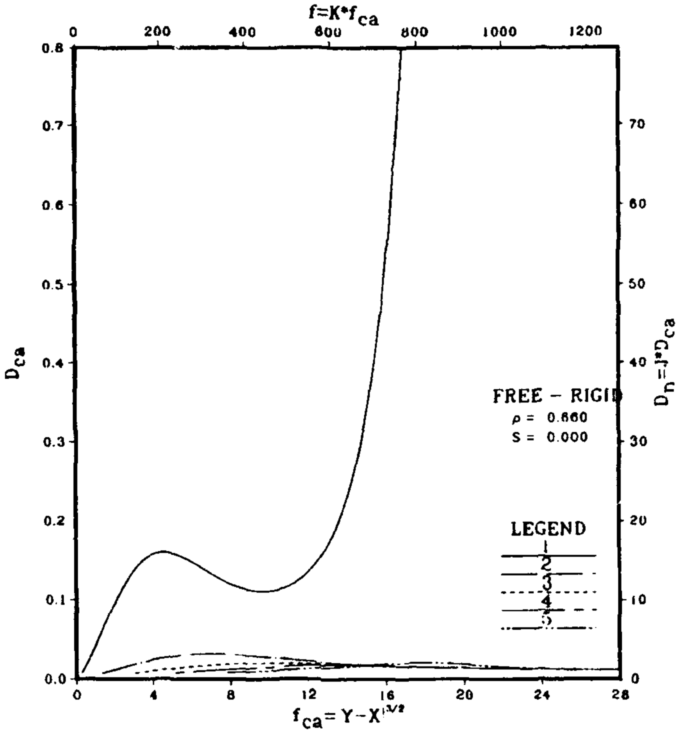

Figure 49. Canonical or customary eigenvalue normalization coefficient for the A modes of figure 43.

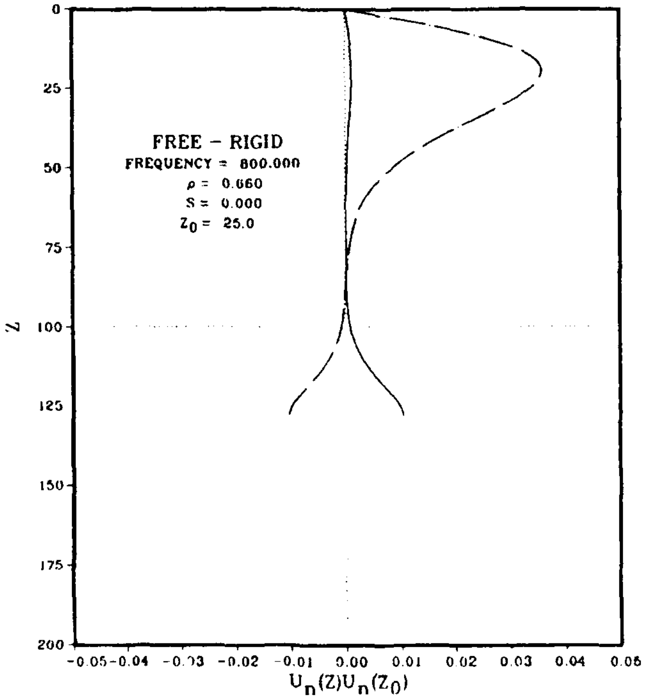

Figure 50. Eigenfunctions at 800 Hz for modes 1 and 2 for the A modes of figure 43.

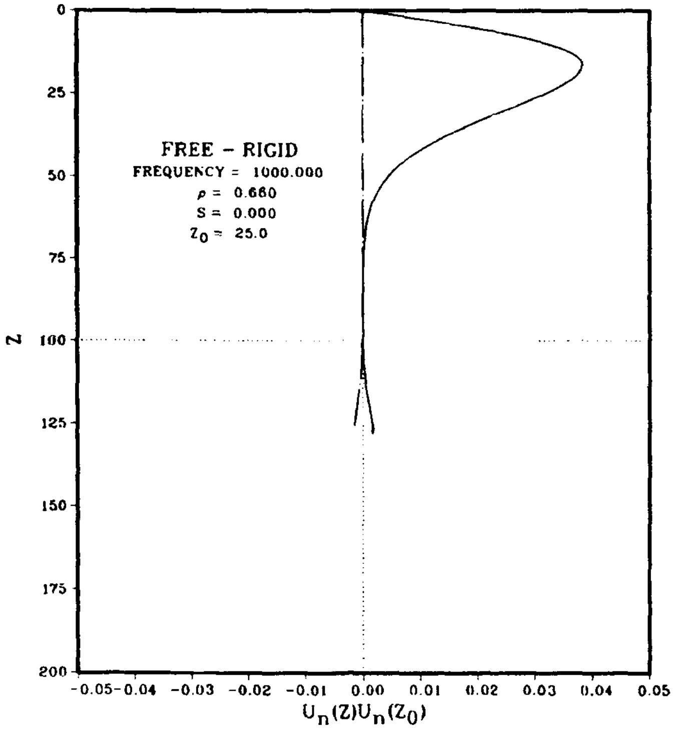

Figure 51. Counterpart of figure 50 at 1000 Hz.

Thus, this case exhibits the same type of behavior encountered in the earlier investigation, i.e., very similar eigenvalues but radically different eigenfunctions in the upper duct. We conclude then that the peculiar results of the earlier investigation are correct and not due to computer roundoff or other errors or artifacts.

Both figures 50 and 51 exhibit a very intriguing result in that the amplitudes for mode 1 and 2 are almost identical in the lower duct, but with a 180-degree change in phase. This same property is exhibited in all our examples of critical frequencies and in figures 32 and 39 as well. Thus, there appears to be some "method in madness." This gives us confidence that the results of figures 50 and 51 are correct and not the results of errors or artifacts.

We note that comparable eigenfunctions in the lower duct was not the case for the earlier investigation that obtained radically different eigenfunctions in both the upper and lower ducts. However, this result should not be surprising because of the different natures of the lower duct. In the present investigation, the lower duct is a negative gradient layer over a rigid boundary. In the earlier investigation, the lower duct was a refractive duct lying over a negative gradient half space.

Since we have no physical concept that explains the results of figures 50 and 51, we turn to a mathematical analysis. The analysis of the eigenvalues itself is different because it involves not only an analysis of $D_n$ but also of the unnormalized eigenvalues. We decided to determine the mathematical circumstances, which lead to the divergence of $D_{ca}$ between modes 1 and 2 in figure 49 and compare this to the convergence between modes 1 and 2 in figure 38. The rationale for this comparison is the convergence of $D_{ca}$ between modes 1 and 2 in figures 31 and 38 and the fact that $D_{ca}$ crosses for the adjacent modes associated with the critical frequency in figure 19. These results are also associated with the critical frequency in figure 19. These results are associated with eigenfunctions which strongly resemble each other. On the other hand, the divergence in figure 49 between $D_{ca}$ for modes 1 and 2 is clearly related to the fact that the eigenfunctions of modes 1 and 2 do not resemble each other.

The dominant term of eq. 88 may be written as

$$Ai^2(-x)\,[y\,Bi^2(-y) + Bi'^2(-y)]\ .$$

For large negative y, the quantity in brackets becomes very large. However, Ai(-x) is near zero and this tends to keep the bracketed term in check.

In the case of 1,000 Hz, $-x_1 = 2.3377657$ and $-x_2 = 2.381100$, while the zero of Ai(-x) is $-x_0 = 2.3381074$. Thus, $-x_2 - (-x_1) = 0.0003443$. This value determines the difference in phase velocity, i.e., the closeness of the eigenvalues. However, $-x_0 - (-x_1) = 0.0003417$ and $-x_0 - (-x_2) = -0.0000026$. Thus, mode 2 lies very close to the zero, whereas mode 1 is much further removed. Indeed $[Ai(-x_1)/Ai(-x_2)]^2 = 2.16 \times 10^6$. In the case of 800 Hz, this ratio $= 5.98 \times 10^3$. Thus, although $x_1$ is closer to $x_2$ and to $x_0$ at the higher frequency, the ifference between mode 1 and 2 in the normalization term continues to increase.

Next, we do a similar analysis for the case of figure 38 at 400 Hz. Here, the coefficient of the bracketed term just discussed is Ai′(-x). Here, $-x_1 = 1.018556$, $-x_2 = 1.019010$, and $-x_0 = 1.018793$. Thus $-x_2 - (-x_1) = 0.000454$, $-x_0 - (x_1) = 0.000237$, and $-x_0 - (-x_2) = 0.000217$. In contrast to our first example, modes 1 and 2 are about equidistant from the zero. Here, $[Ai'(-x_1)/Ai'(-x_2)]^2 = 1.19$. Thus, not surprisingly, the modes 1 and 2 values in figure 38 are close together at 400 Hz.

Our final investigation was to make certain that the type of behavior exhibited in figure 49 was not exclusive to the free-rigid boundary condition. Thus, we examined the free-free boundary condition for $S = 0$ and $\rho = 1.322$. This value of $\rho$ superimposes the vertical asymptotes of modes 2 and 3. The counterpart of figure 49 for $\rho = 1.322$ demonstrated that the $D_{ca}$ for mode 2 was well behaved while that of mode 3 diverged in a manner similar to that of mode 1 in figure 49. We conclude then that the behavior encountered here for the free-rigid boundary condition and for modes 1 and 2 occurs whenever a $\rho$ is chosen to superimpose vertical asymptotes for any two modes and for any boundary condition.

## G. NEW MEASURES OF MODE COUPLING

Reference 4 introduced the cross-duct coupling function as a measure of mode coupling. This is a useful measure of more coupling as a function of frequency for a given profile configuration. However, it does not appear to be as useful in comparing different profile configurations as two other measures of mode coupling to be discussed here. The chief purpose for introducing these other measures is to determine if the coupling exhibited in figurs 32, 39, 50, and 51 for S = 0 is similar to or different from that for critical frequencies such as exhibited in figures 23, 24, and 25.

The first measure of coupling that comes to mind is the difference in phase velocity between the adjacent modes, because in general, the smaller this difference the closer the modes are coupled. However, this does not take into account the frequency dependence. A measure which takes this into account is the difference in wavelength or $\Delta_n = \omega C_{pn} C_{pn+1}(\Delta C_m)^{-1}$. However, a related measure is the mode interference range as given by $R_{n+1} = 2\pi\Delta\lambda_n$. Here, the closer the mode coupling, the larger the interference range.

We now define a new measure of mode coupling. For our examples of closely coupled modes, the mode amplitude of the lower order mode formed a relative minimum whereas the higher order mode had a zero crossing. We observed that the amplitude at the relative minimum was smaller for the more highly coupled modes. Our new measure then was the amplitude of this relative minimum divided by the largest amplitude for this mode. We note that this measure is independent of source depth, because the source depth factor scales both amplitudes by the same amount.

We now examine the correlation between our new measure of mode coupling and the mode interference range. This correlation is shown in figure 52 on a log-log scale. The points are labeled by the figure number corresponding to the evaluation. We see that the points for figures 32 and 39 exhibit the same general relationship as that of figures 23, 24, and 25. We conclude then that the coupling exhibited in figures 32 and 39 is essentially the same as that for critical frequencies as exhibited in figures 23 to 25. The evaluation for figure 50 is given by the cross. The corresponding evaluation for figure 51 lies off scale at a ratio of $2.6 \times 10^{-5}$ and an interference range of $1.8 \times 10^{4}$ km. This evaluation as well as that for figure 50 bears little resemblance to the other evaluations. This result reinforces our previous conclusion that the coupling characteristics for S = 0, in which $\rho$ is designed to superimpose a pair of vertical asymptotes, are radically different from those for critical frequencies. In contrast, the coupling characteristics for S = 0 and $\rho = 1$ for the free-free and rigid-rigid boundary conditions are rather similar to those for critical frequencies.

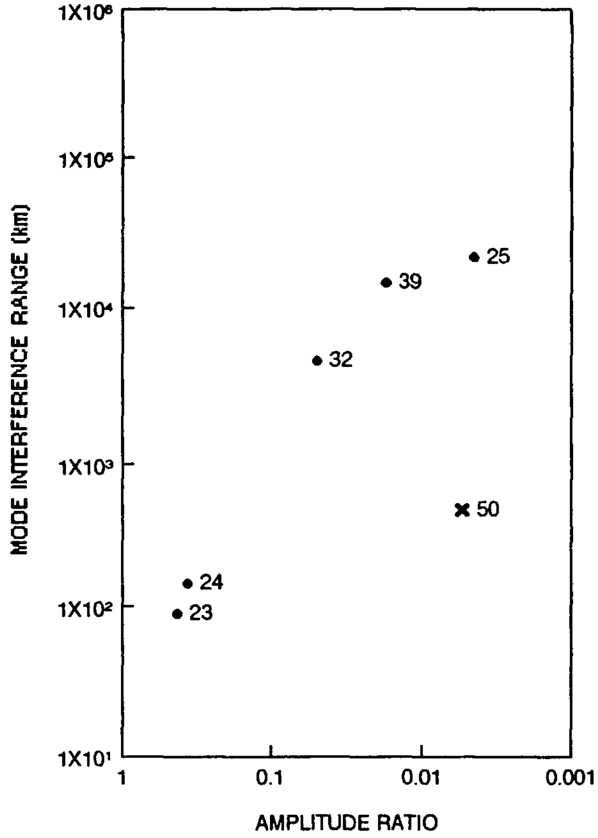

Figure 52. Correlation between the mode interference range and the ratio of minimum to maximum amplitude of the lower order mode.

## H. EIGENVALUE DIFFERENCES AT ESTIMATES OF CRITICAL FREQUENCY

This section presents numerical results that follow from section 2J. In the early stages of this report, we examined various cases of ρ and S in a somewhat haphazard manner. These cases indicated that the value of y at the critical frequency was a more important parameter than either the parameters ρ or S from which y is derived. Our initial impression was that when y was greater than about -1, there was no significant coupling and that when y was more negative than about -2, the modes were too closely coupled to be of interest. Thus, it initially appeared that the cases of most interest fell roughly between y = -1 and y = -2. Figure 14 is a good example of this situation. Section 2J was developed as a analysis tool to determine if this impression was correct.

Figure 53 presents the results of the analysis for the free-rigid boundary condition. The results only apply to modes 1 and 2. The vertical scale is the estimate of the difference between eigenvalues as given by the discriminate of eq. A-6. The horizontal scale is ρ. Each curve corresponds to a fixed value of y ranging from -0.1 to -10. The procedure for generating a curve is to solve eq. 107 for S in terms of y and ρ for m and n = 1. We take the fixed value of y and evaluate S for some choice of ρ. For each set of y, ρ, and S we evaluate the discriminate using eqs. 101 and 102. Each curve is generated by stepping through the desired range of ρ.

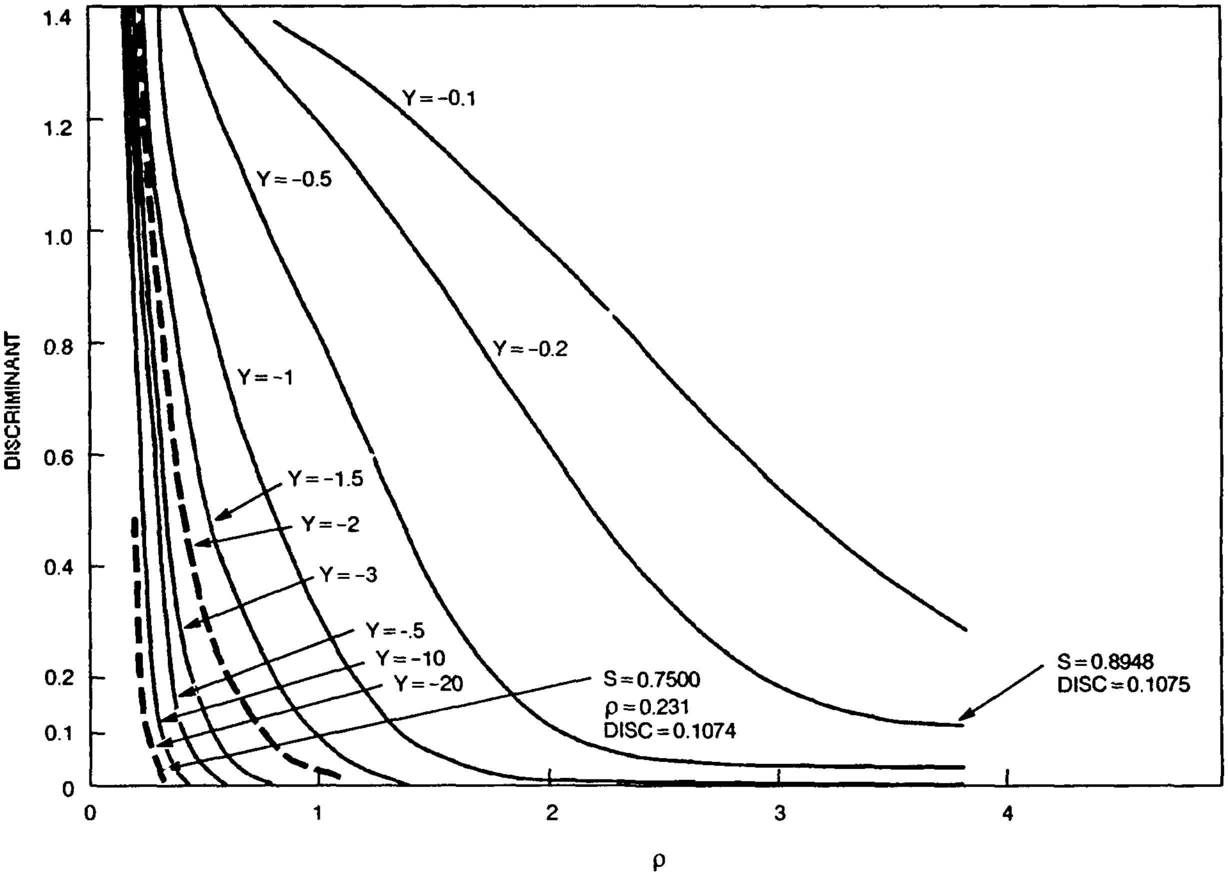

Figure 53. Estimate of eigenvalue separation as a function of ρ for various values of y for the estimated critical frequency for the free-rigid boundary.

Figures 54 and 55 are the respective counterparts of figure 53 for the free-free and rigid-rigid boundary conditions. Here, we use eqs. 110 or 114 to solve for S and evaluate the discriminant using eqs. 101 or 102.

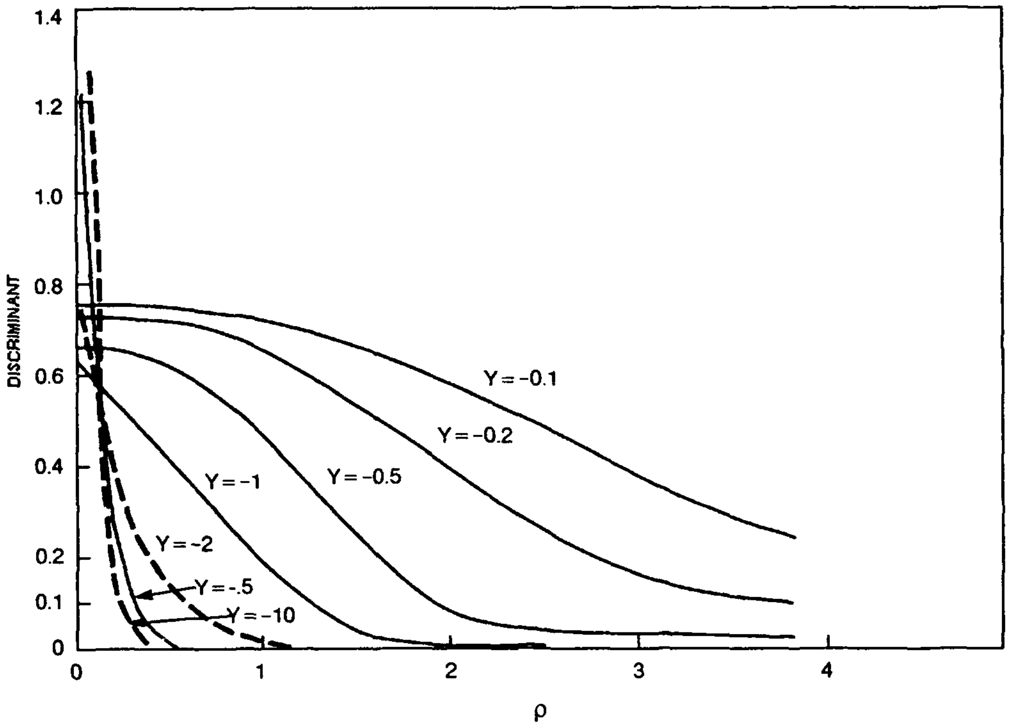

Figure 54. Counterpart of figure 53 for the free-free boundary.

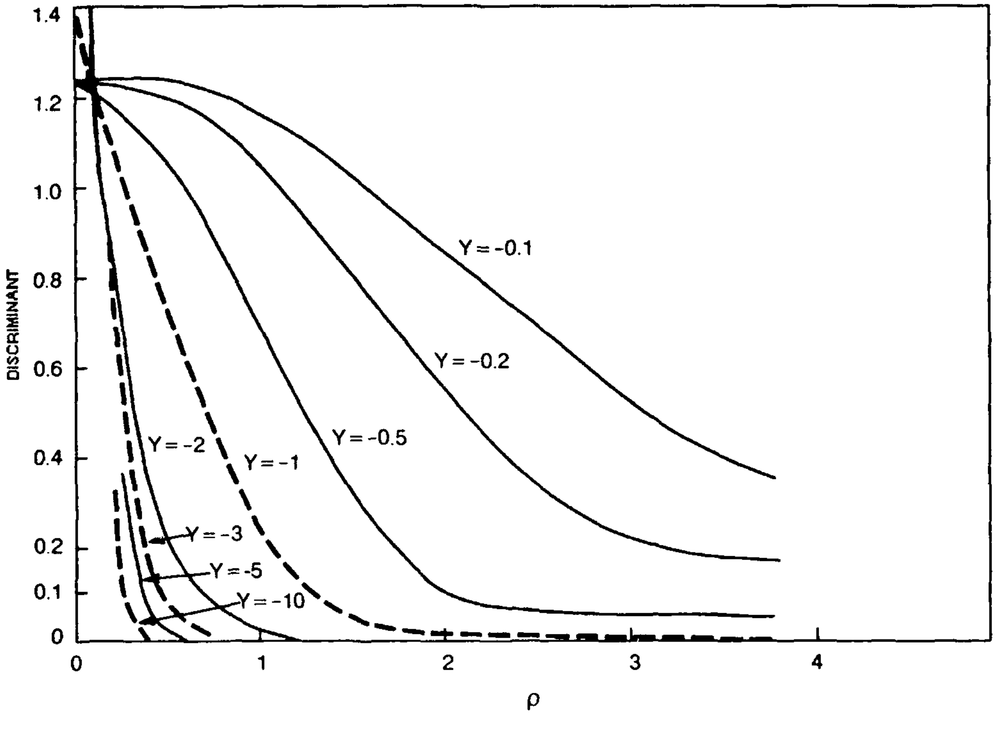

Figure 55. Counterpart of figure 53 for the rigid-rigid boundary.

We note that the parameters S is not shown in figures 53 to 55. In the case of figures 54 and 55, $\rho = 1$ corresponds to $S = 0$. Thus, for $\rho > 1$, S is positive and increases with increasing $\rho$. For $\rho < 1$, S is negative and becomes more negative as $\rho$ goes to zero. In the case of figure 53, $\rho = 0.6601015$ corresponds to $S = 0$ and S is positive for $\rho > 0.6601015$ and negative for $\rho < 0.6602015$.

We note that for values of $\rho$ greater than about 0.2 or 0.3 the discriminant decreases as y becomes more negative. This supports our original impression that y is the important parameter and that the mode separation increases as y becomes less negative. For values of $\rho$ below 0.2 or 0.3 the curves of y are no longer nested but cross over each other. However the evaluations in figures 53 to 55 in this area are incomplete and need further work beyond the scope of this report. The chief purpose of figures 53 to 55 is to serve as a guide in selecting the choices $\rho$ of and S to be used as examples of the various patterns the eigenvalue solutions take on as presented in the next section.

## I. EIGENVALUES FOR VARIOUS COMBINATIONS OF $\rho$ AND S

This section presents canonical eigenvalues and associated sound-speed profiles for various combinations of $\rho$ and S. This is not a thorough investigation, but rather a sampling to give a feel for the eigenvalue patterns for a variety of choices of $\rho$ and S.

We start the analysis with an examination of small negative values of y to determine if it is possible to have close coupling for critical points close to $y = 0$. Figure 56 presents the eigenvalues for $S = 0.8948$ and $\rho = 3.9$ for the free-rigid boundary. These parameters correspond to the last point evaluated on the $y = -0.2$ curve in figure 53. The value of the discriminate is 0.1075.

We see that the separation between mode eigenvalues can indeed be very small for critical points with small negative values of y. This not only occurs for the critical points for modes 1 and 2 but also for modes 4 and 5 at a value of y even closer to zero than $y = -0.2$. This separation is also small for the critical points for modes 2 and 3 and 3 and 4 for which y is closer to zero than $y = -0.5$.

Figure 57 presents the eigenvalues for $S = 0.8574$ and $\rho = 3.8$ for the free-free boundary. These parameters correspond to the last point evaluated on the $y = -0.2$ curve in figure 54. The value of the discriminate is 0.108. Small differences occur for modes 1 and 2 at $y = -0.2$ and for modes 2 and 3, 3 and 4, and 4 and 5 for y closer to zero than -0.5.

Figure 58 presents the eigenvalues for $S = 0.519$ and $\rho = 2.1$ for the rigid-rigid boundary. In this case, we did not take the endpoint of the $y = -0.2$ curve in figure 55 because the discriminate was significantly larger than 0.1. Here, we selected $\rho = 2.1$ as the point where the $y = -0.5$ curve leads to a discriminate of 0.104. Here the small differences occur for modes 1 and 2 for $y = -0.5$ and for modes 2 and 3, 3 and 4, and 4 and 5 for values of y between about -1 and -2.5.

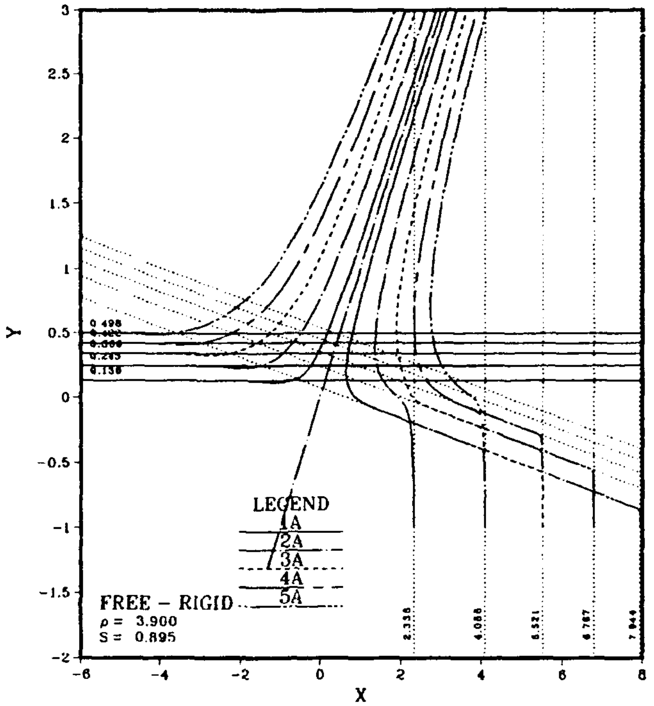

Figure 56. Eigenvalues for S = 0.895, ρ = 3.9, free-rigid boundary.

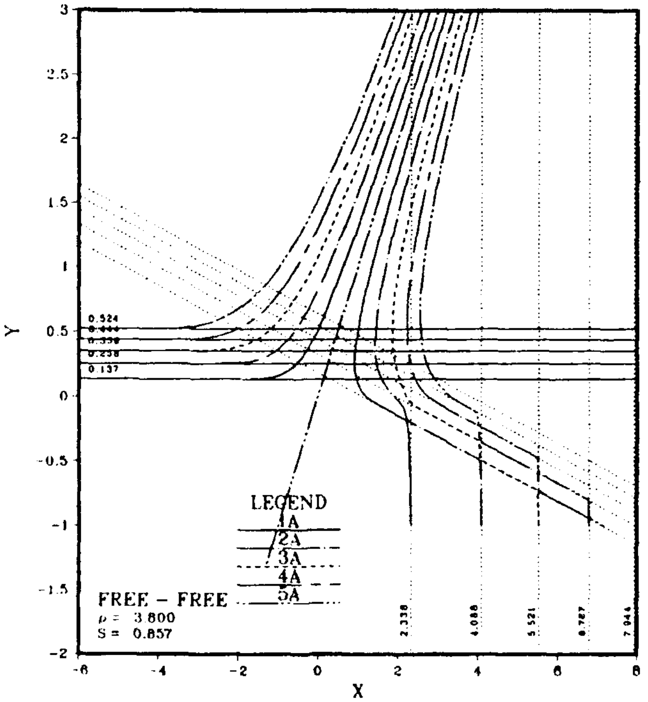

Figure 57. Eigenvalues for S = 0.857, ρ = 3.8, free-free boundary.

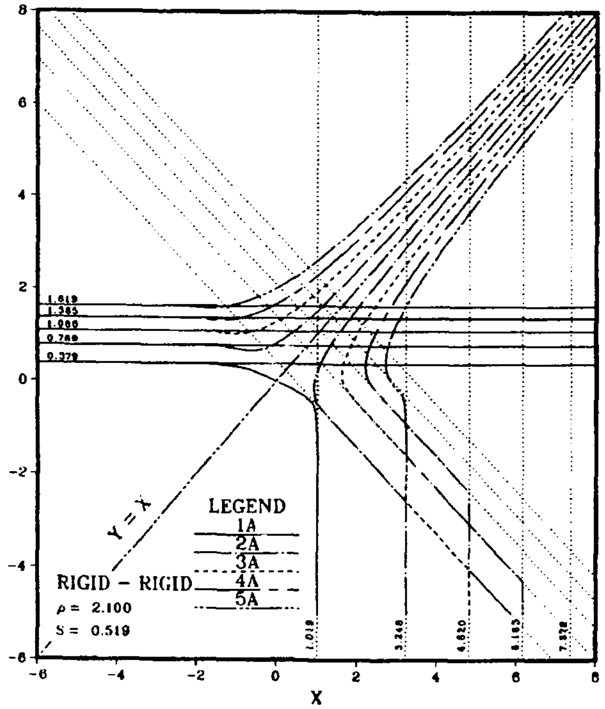

Figure 58. Eigenvalues for S = 0.519, ρ = 2.1, rigid-rigid boundary.

Figures 59 a to c present the sound-speed profiles associated with the parameters of figures 56 to 58 respectively. As usual, the standard parameters for the surface layer were used. These profiles are examples approaching the limiting case of a positive-gradient layer overlapping an isospeed layer. In this limit, S goes to 1 and ρ goes to infinity. In this limit, eqs. 42 or 44 reduce to y = 0. Thus, in the limit the slant asymptotes of figures 56 to 58 collapse to a horizontal line at y = 0. This result suggests that close coupling between modes can occur for very small negative values of y. This is done by letting S approach closer to 1 and ρ approach large positive values.

Our next six examples, were chosen to determine if relatively large negative values of y always lead to extremely close coupling between modes or if modest mode coupling can occur. The parameters ρ and S for all six examples where chosen so that y = -5 for the intersection between the asymptotes associated with modes 1 and 2. For the first three examples, ρ was chosen in figures 53 to 55 so that the discriminant would be about 0.1. Figure 60 is for S = -0.549 and ρ = 0.4 for the free-rigid boundary. Figure 61 is for S = -2.793, ρ = 0.32 for the free-free boundary. Figure 62 is for S = -1.003, ρ = 0.38 for the rigid-rigid boundary. Only the A mode eigenvalues are shown here as will be the case for other examples to be presented later. In all three figures, modes 1 and 2 have extremely close coupling, which is not comensurate with our discriminate value of 0.1. More will be said of this later. However, a fortuitous result in figure 61 shows a significant displacement between modes 2 and 3 at the point of closest approach for a value of y somewhat more negative that -2.

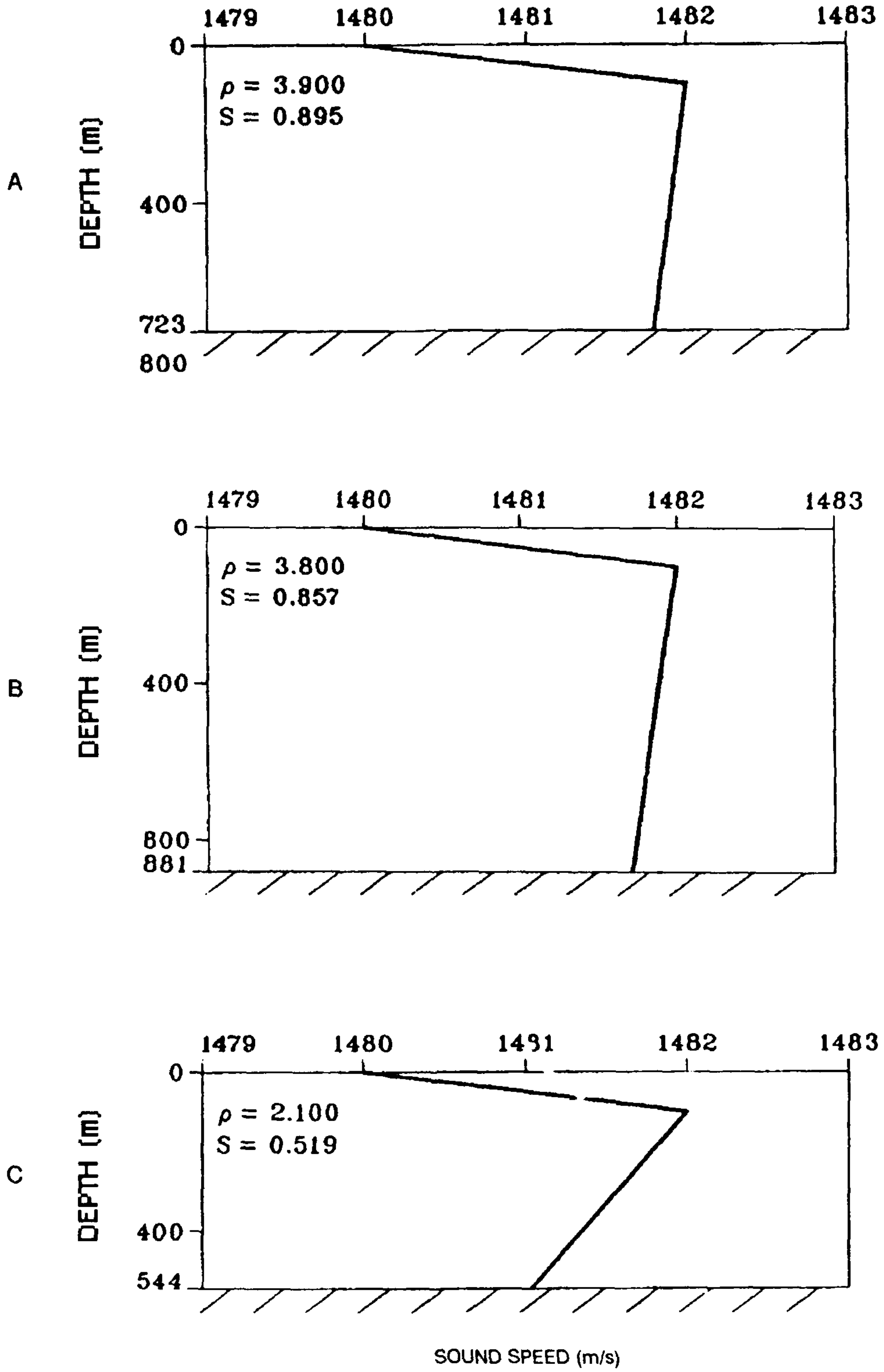

Figure 59. Sound-speed profiles associated with figures 56 to 58 respectively.

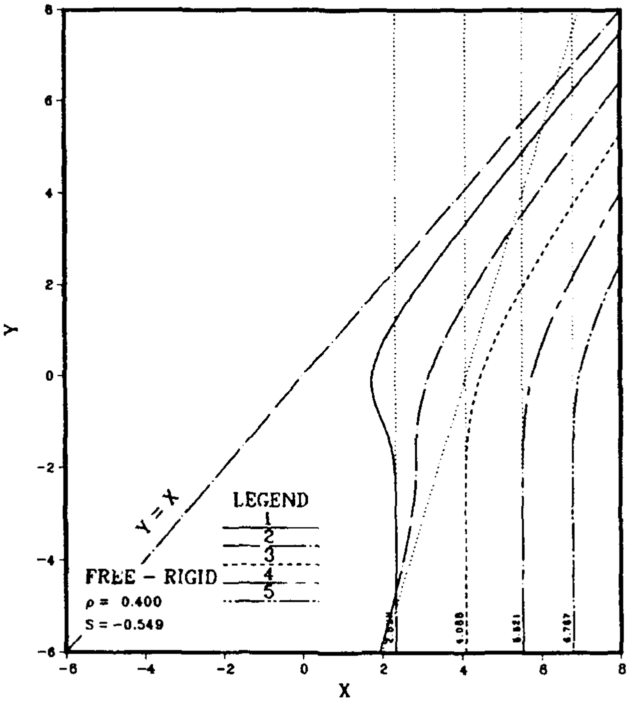

Figure 60. Eigenvalues for S = –0.549, ρ = 0.4, free-rigid boundary.

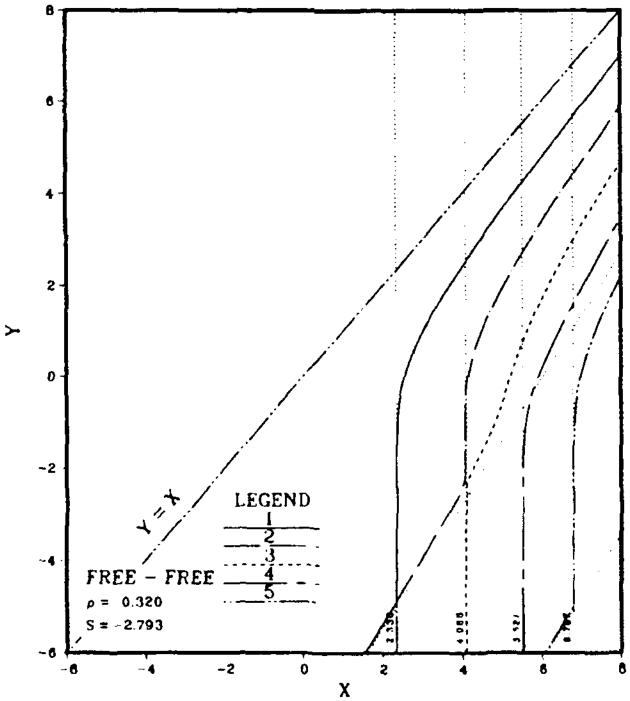

Figure 61. Eigenvalues for S = –2.793, ρ = 0.320, free-free boundary.

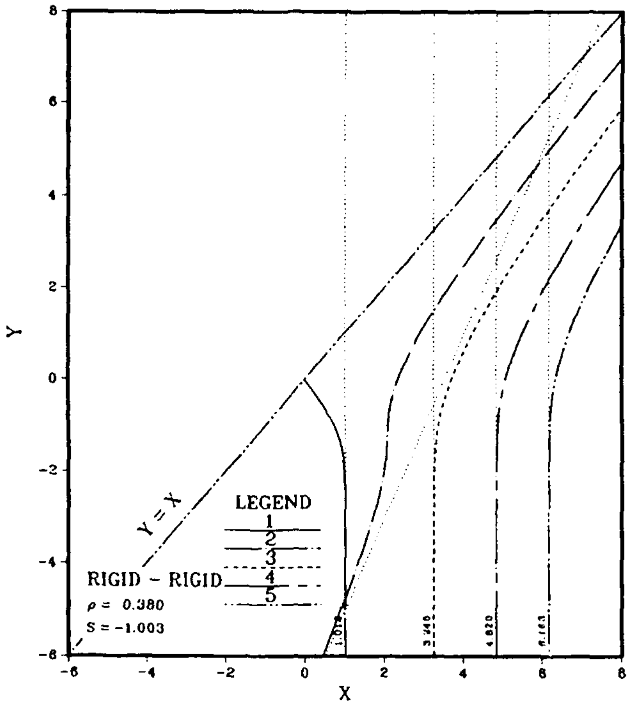

Figure 62. Eigenvalues for S = -1.003, ρ = 0.380, rigid-rigid boundary.

This latter example suggests that significant displacements can occur for modest values of negative y. For the next three examples, ρ was chosen from figures 53 to 55 to yield large values of the discriminate, viz, 0.8, 0.6, and about 0.6. The idea here was to determine if we could separate modes 1 and 2 at the critical frequency by increasing the discriminant of our approximation. Figure 63 is for S = -2.991, ρ = 0.2 for the free-rigid boundary. Figure 64 is for S = -29.93, ρ = 0.1, for the free-free boundary. Figure 65 is for S = -4.062, ρ = 0.2 for the rigid-rigid boundary. Figure 63 displays a significant displacement between modes 1 and 2 for y between -3 and -4. Figure 64 displays extremely close coupling between modes 1 and 2. However, there is a relatively large displacement between modes 3 and 4 for y between -3 and -4. Figure 65 displays a small but definite displacement between modes 1 and 2 for y between -3 and -4.

Figures 63 to 65 clearly indicate why the approximation for the displacement between modes at the critical frequencies fail. The main problem is that the estimates of critical frequencies of section 2F given by the intersections of the asymptotes are not good. The critical frequencies of figures 63 , 65, and 64 lie well above the intersection at $y = -5$. This is also true to a somewhat lesser extent for figures 60 to 63. Indeed, there are some good indications that the expansions of Section 2J are reasonably good if we examine the mode displacements at y = -5 rather than at the critical frequency.

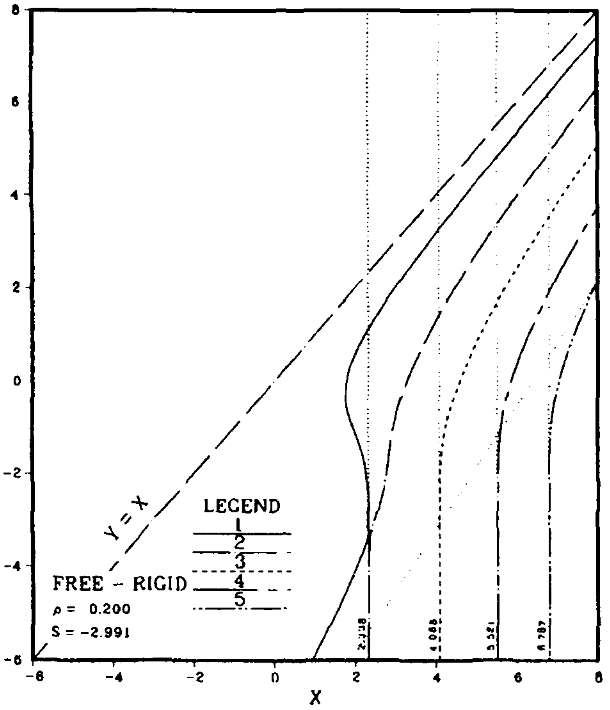

Figure 63. Eigenvalues for S = –2.991, ρ = 0.2, free-rigid boundary.

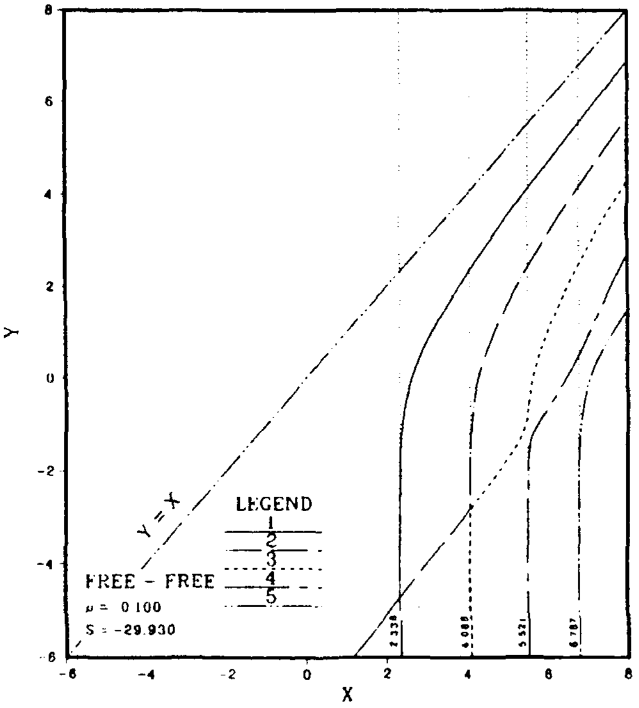

Figure 64. Eigenvalues for S = –29.93, ρ = 0.1, free-free boundary.

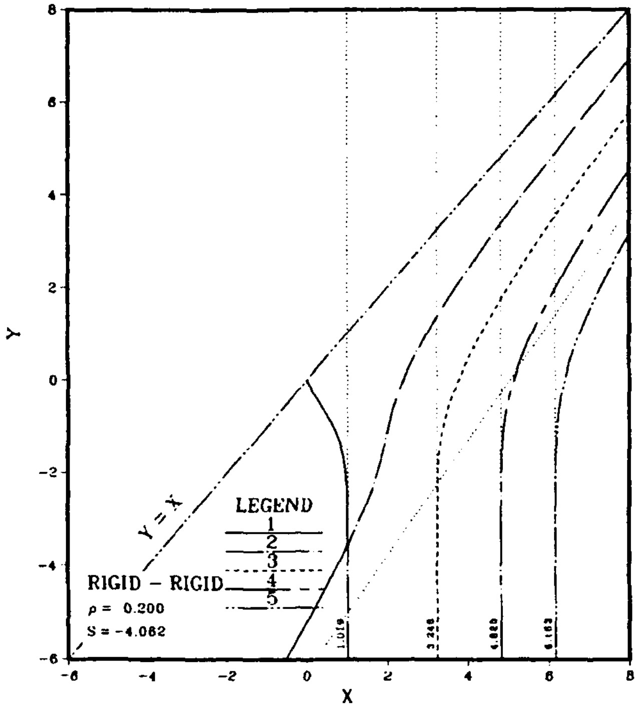

Figure 65. Eigenvalues for S = –4.062, ρ = 0.2, rigid-rigid boundary.

For example, in figure 63 this displacement is about 0.8 as was originally determined from figure 53. Similarly the mode displacements at y = –5 are large for figures 64 and 65 and significantly smaller for figures 60 to 62 in line with our original choice of displacement.

The sound-speed profiles associated with figures 60 to 65 are presented in figures 66 and 67. These are the first examples of negative values of S. Negative S means that the bottom boundary sound speed is smaller than the surface sound speed. The more negative the value of S, the lower the bottom sound speed. Figure 67b for S = –29.930 is the most extreme case shown here with bottom sound speeds some 50 odd m/s below the surface sound speed. These negative values of S give positive slopes on the slant asymptotes of figures 60 to 65 as given by eqs. 42 or 43. As the bottom sound speed goes to zero as a limit S goes to – ∞, and the slope of the slant asymptotes goes to 1 as a limit. This limit is probably related to the unity slope for the line y = x. Asymptotes with slopes between +∞ and one intersect the line y = x for positive values of y. These have no significance as this is beyond the regime of mode coupling. However, suppose the slope of the slant asymptotes could be less than one. These slant asymptotes would intersect the line y = x for large negative values of y. This intersection would represent an impossible physical situation because y = x represents zero frequency, whereas large negative y represents the large end of the frequency spectrum.

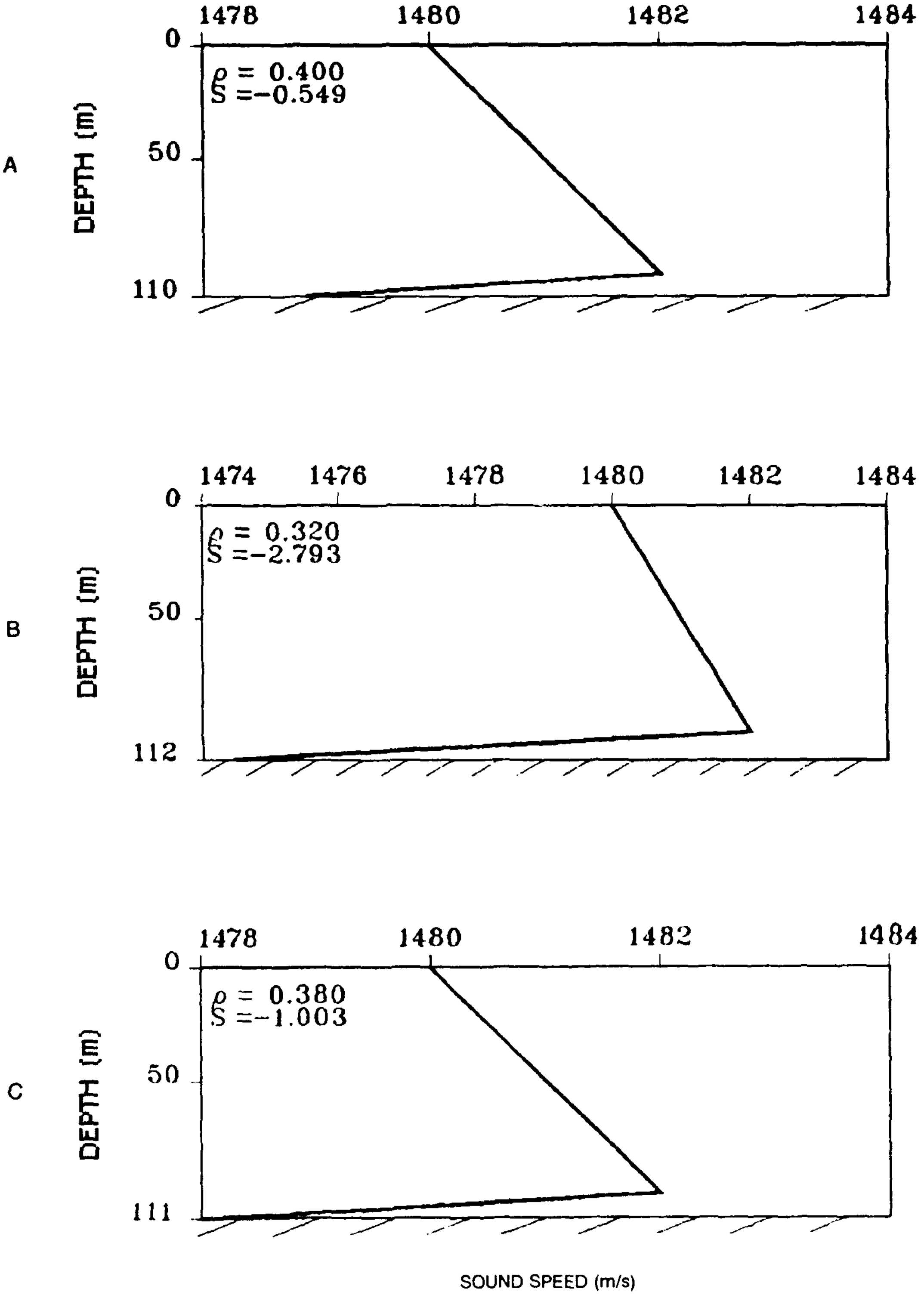

Figure 66. Sound-speed profiles associated with figures 60 to 62 respectively.

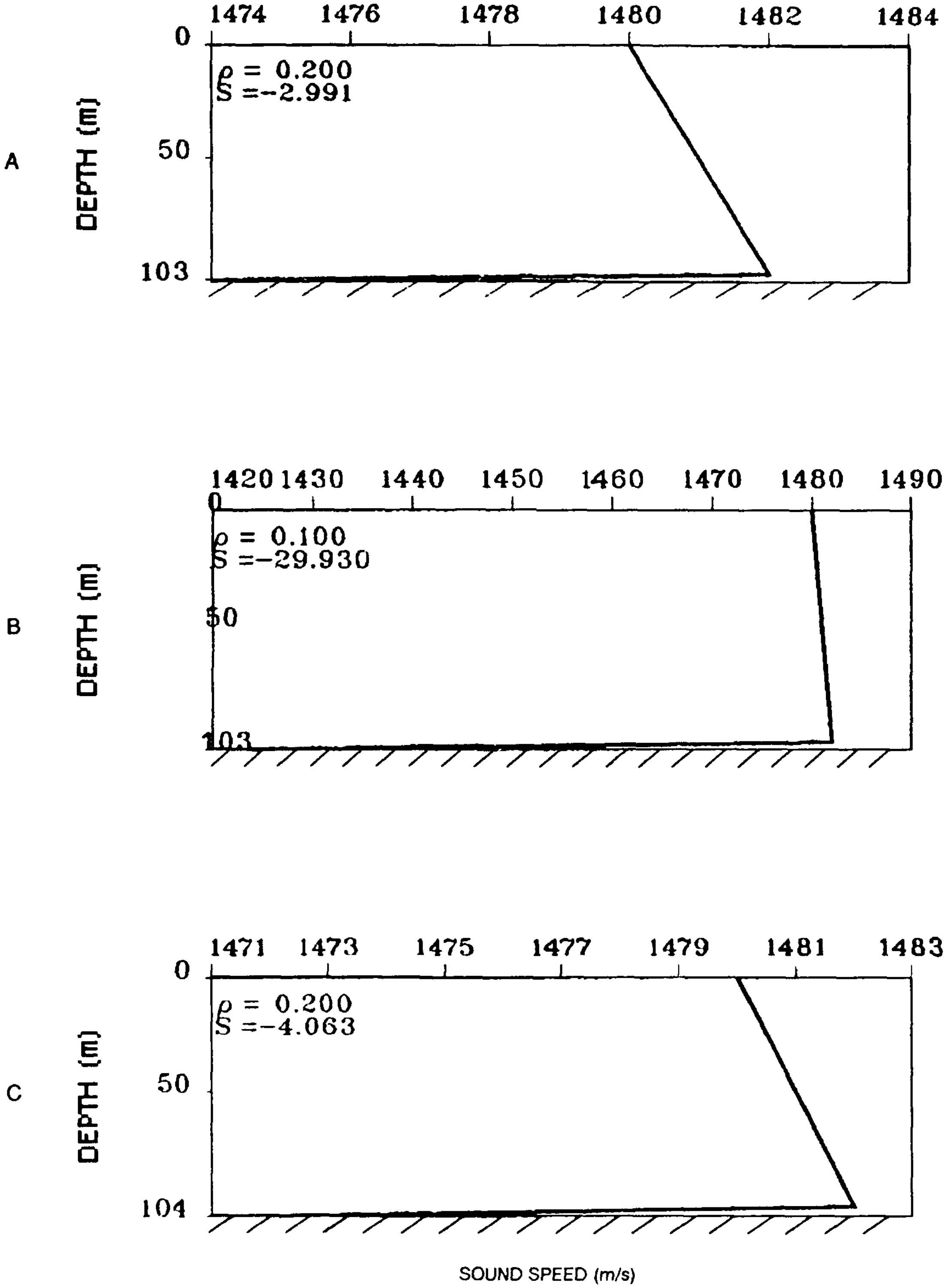

Figure 67. Sound-speed profiles associated with figures 63 to 65 respectively.

We note another consequence of negative S. At sufficiently large frequencies, the low-order modes will be associated with the slant asymptotes. (This is just the opposite of the case of positive S where at high frequencies, the low-order modes are associated with the vertical asymptotes). The reason is that for negative S the modes are initially trapped in the lower duct, because the sound speed at the bottom boundary is smaller than that at the surface.

For our next six examples, we chose a more modest value of $y = -2$ with values of S slightly positive in figures 68 to 70 and slightly negative in figures 71 to 73. In figure 68 the value of $\rho = 0.73$ was chosen from figure 53 for a discriminant of 0.1. In figure 69 $\rho = 1.05$ was chosen from figure 54 for a discriminant of 0.015. In figure 70 $\rho = 1.05$ was chosen from figure 55 for a discriminant of 0.025. The values of S for these three cases is positive. We see that modes 1 and 2 are strongly coupled in figures 69 and 70 corresponding to small values of the discriminant, whereas figure 68 displays a separation comensurate with a larger discriminant of 0.1. In figure 71 the value of $\rho = 0.57$ was chosen from figure 53 for a discriminant of 0.2. In figure 72 $\rho = 0.56$ was chosen from figure 54 for a discriminant of 0.1. In figure 73 $\rho = 0.73$ was chosen from figure 55 for a discriminant of 0.1. The values of S for these 3 cases is negative. Here, we see the most separation between modes 1 and 2 in figure 71 with about one-half this amount of separation in figures 72 and 73. Figures 72 and 73 contain fortuitous results in the relatively large separation between modes 4 and 5 for $y = -1$.

The sound-speed profiles associated with figures 68 to 73 are presented in figures 74 and 75. These profiles are characterized by surface and bottom sound speeds reasonably close to each other. They are not nearly as extreme as the profiles of figures 66 and 67.

In closing this section, we believe that the results of figures 71 to 73 answer our original speculation about large separations between modes for relatively large negative values of y. The key is to pick small negative values of S together with values of $\rho$ leading to the desired y. It would be interesting to see if this approach will lead to large separations for even more negative values of y. However, this would entail more extensive and careful evaluation in figures 53 to 55, which is beyond the scope of the present report.

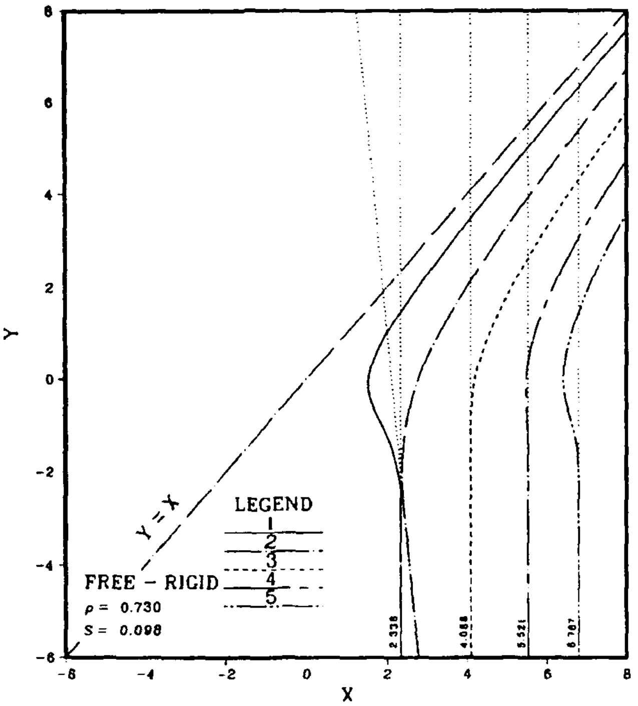

Figure 68. Eigenvalues for S = 0.0983, ρ = 0.73, free-rigid boundary.

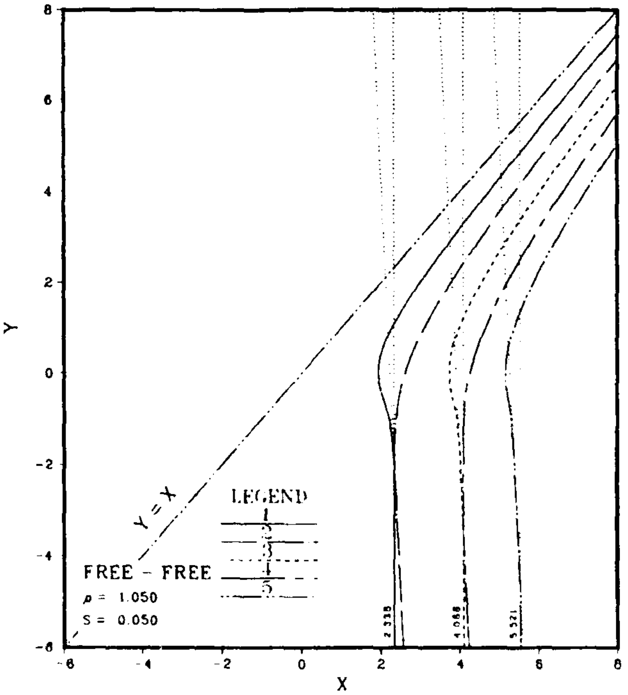

Figure 69. Eigenvalues for S = 0.0501, ρ = 1.05, free-free boundary.

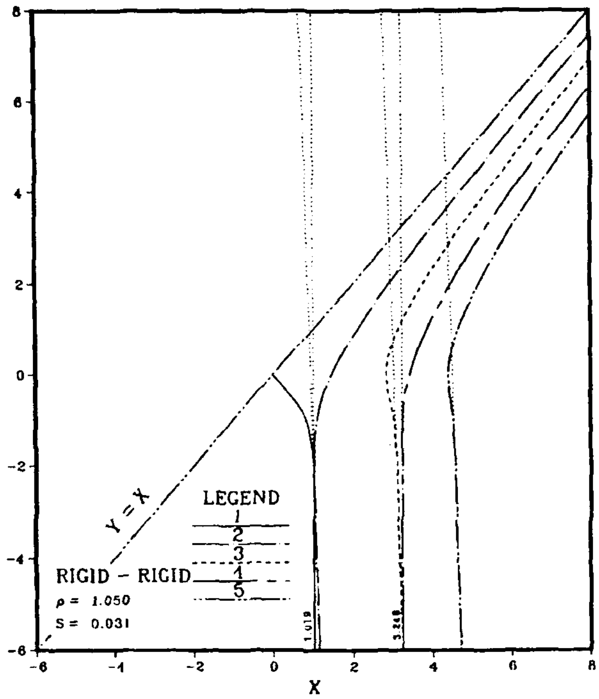

Figure 70. Eigenvalues for S = 0.0314, ρ = 1.05, rigid-rigid boundary.

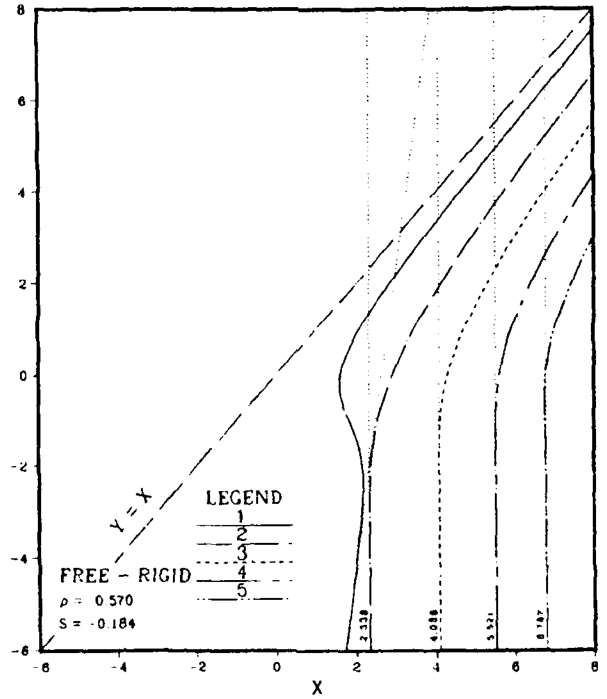

Figure 71. Eigenvalues for S = −0.184, ρ = 0.57, free-rigid boundary.

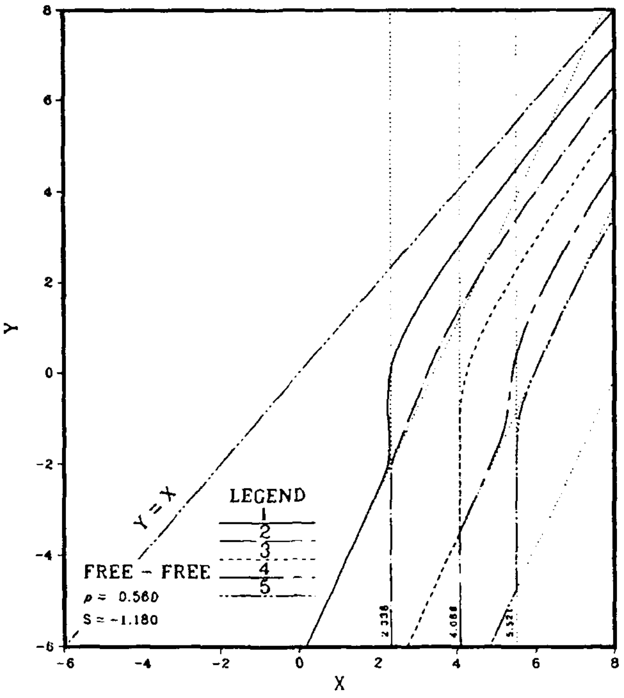

Figure 72. Eigenvalues for S = −1.18, ρ = 0.56, free-free boundary.

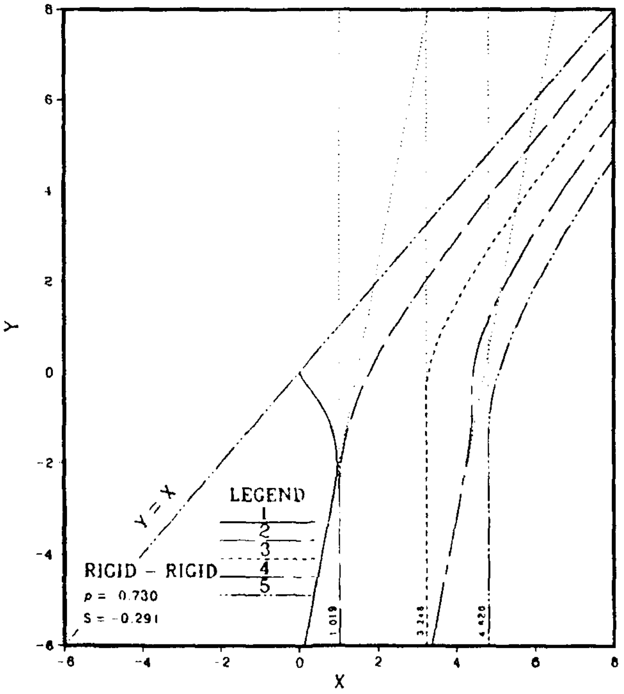

Figure 73. Eigenvalues for S = −0.291, ρ = 073, rigid-rigid boundary.

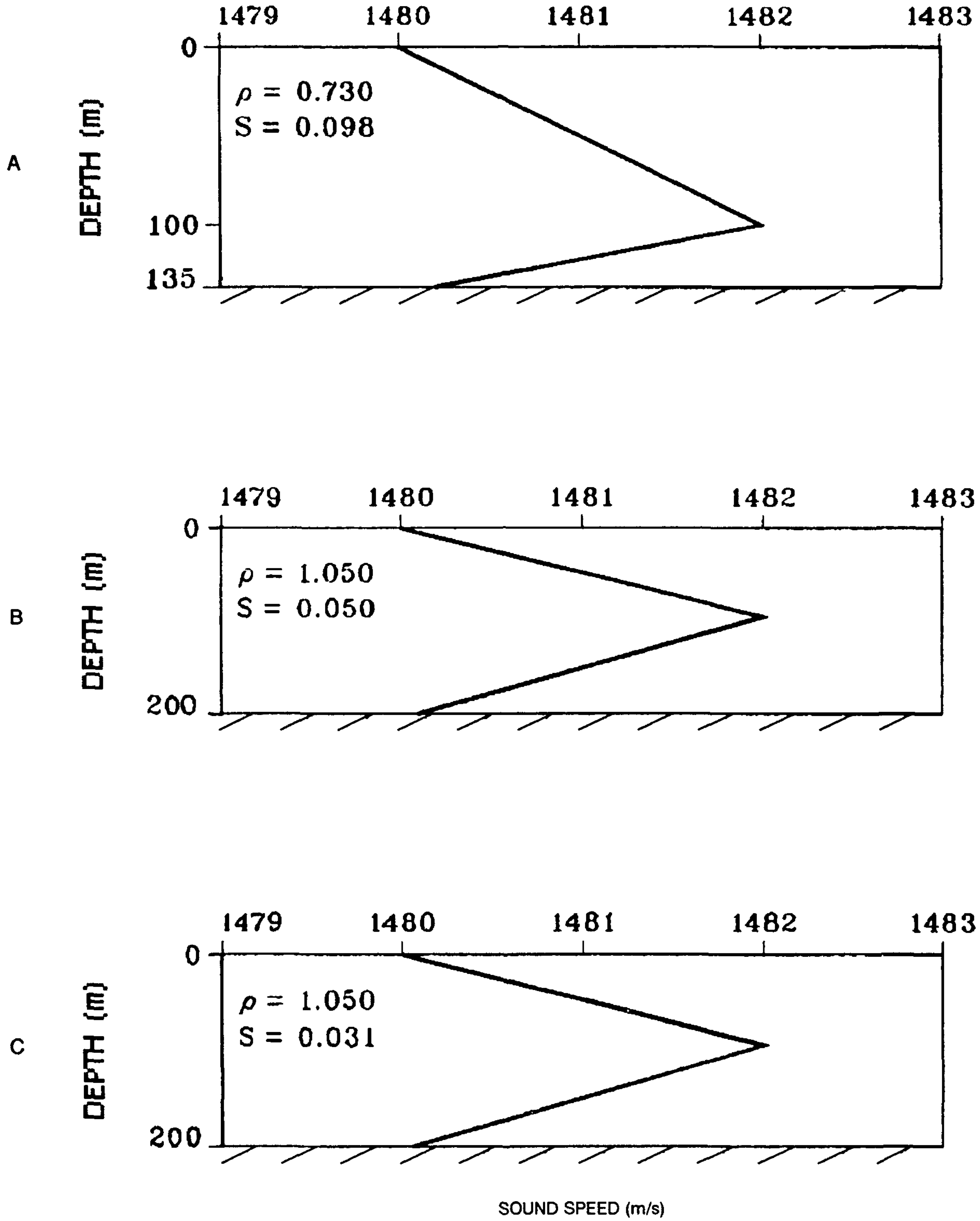

Figure 74. Sound-speed profiles associated with figures 68 to 70 respectively.

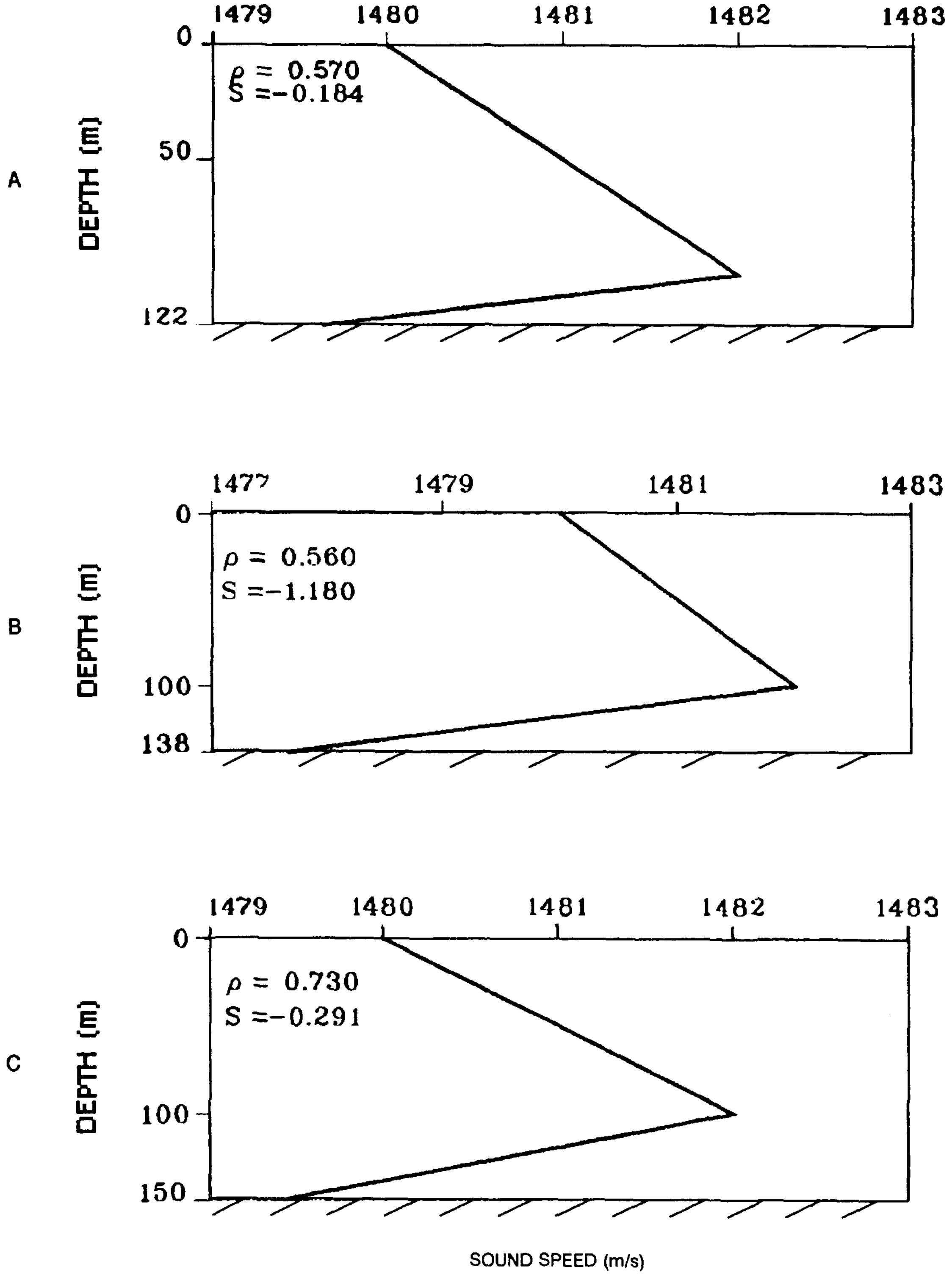

Figure 75. Sound-speed profiles associated with figures 71 to 73 respectively.

# 4. AREAS FOR FURTHER INVESTIGATION

This brief section points up some of the areas requiring additional investigation.

One of the primary areas of interest is the treatment of the normalization process. Although the present approach is correct, it is not satisfactory to have to deal with $D_n$ that ranges from small to huge or even divergent values. An investigation of alternative methods of defining the unnormalized eigenfunctions so that $D_n$ is well behaved is recommended. Some of these alternative methods are suggested in section 3A.

Another area of interest is to determine the common curve $D_{ca}$ approaches for all modes at high frequencies in figure 31 and also with some additional complication in figure 20. A related investigation is why $D_{ca}$, for the rigid-rigid boundary condition in figure 38, does not approach a common curve for large frequencies as is the case for other boundary conditions.

Some aspects of the example of section 3F still pose an interesting enigma in that some features associated with coupled modes are present such as almost identical amplitudes in the lower duct but radically different amplitudes in the upper duct. Although a detailed investigation of the mathematics of this example indicate that the results are correct, we have no rationale from a physical perspective as to why this differs from other coupled mode configurations. It would also be of interest to determine if there is some other approach to eigenvalues that would not lead to the divergent values of $D_n$ encountered for this special case.

It would be interesting to make a thorough investigation of the accuracy of the mode displacement at the critical frequencies as given by the approximations of section J. The present work suggests that accuracy may be quite good for positive values of S and slightly negative values of S. The chief problem is with large negative values of S, where the critical frequencies do not lie close to the approximation given by the intersection of asymptotes. It would be desirable to formulate a new approach for predicting critical frequencies for large negative values of S, although it is not obvious how to proceed in the formulation.

It would also be desirable to clean up the curves of figures 53 to 55 for large negative values of y. This would be a first step in evaluating our premise that large displacements may be found for large negative y with the use of small negative values of S and appropriate values of $\rho$.

In the early stages of this report, we spent some time investigating the mathematical principle involved in section 3E in which the eigenvalues for one mode remains almost stationary, whereas those of the other mode move rapidly as $\rho$ is moved above or below the values leading to common vertical asymptotes. Here, the physical principle is related to an abhorrence of degenerate eigenvalues. However, the detailed mathematical whys and wherefores remain of interest. We did not complete this investigation. However, the preliminary results appeared promising and should be pursued further. Our approach was to investigate the quadratic expression for coincident roots. Here, the discriminant goes to zero leaving only one value no matter which sign is picked for the square root of the discriminant. However, when we differentiate the expression with respect to the parameter ρ, the derivative was different for the choice of signs on the square root of the discriminant. Here, one choice of signs leads to a rate of change with respect to ρ of zero whereas the other choice leads to a rate of change equal to twice that of a simple zero.

In closing this report, we note that we have achieved our original goal in formulating the canonical eigenvalue approach. This goal was to reduce the number of parameters (in this case from six to two) so that the salient features of double-duct propagation could be analyzed. However, even this simplification leaves a somewhat formidable problem in that the investigation still involves the behavior of eigenvalues in the two-dimensional space of S and ρ. We attempted to solve this problem by introducing the parameter y for the intersection of the asymptotes for S, ρ, and the boundary conditions. We found that y does indeed appear to provide more information about the nature of the eigenvalues than does ρ or S alone. The introduction of the discriminant in the representation of figures 53 to 55 also helped in the analysis. However, these approaches are not adequate, particularly for large negative values of S. We have come a long way, but there is a long way to go before a satisfactory understanding is available for this most simple of double ducts to say nothing of more complicated double-duct configurations.

# 5. REFERENCES

1. Pedersen, M. A., D. F. Gordon, and F. Hosmer. 1990. "Canonical Eigenvalues, Part I: General Theory." NOSC TR 1332 (Feb). Naval Ocean Systems Center, San Diego, CA.

2. Pedersen, M. A., D. F. Gordon, and F. Hosmer. 1990. "Normal-Mode and Phase-Integral Methods for Determining Phase and Group Velocities in Simple Underwater Acoustic Ducts." NOSC TR 1331 (Feb). Naval Ocean Systems Center, San Diego, CA.

3. Pedersen, M. A., D. F. Gordon, and F. Hosmer. 1990. "Canonical Eigenvalues, Part II: Application to One-Layer, Bounded Underwater Acoustic Ducts." NOSC TR 1333 (Jun). Naval Ocean Systems Center, San Diego, CA.

4. Pedersen, M. A., D. F. Gordon, and S. Edwards. 1990. "Frequency Spectrum Characteristics: Underwater Acoustic Propagation in Double Ducts." NOSC TR 1330 (Feb). Naval Ocean Systems Center, San Diego, CA.

5. Miller, J. C. P. 1946. *The Airy Integral.* British Association for the Advancement of Science, Match Table Pt., Cambridge University Press, Cambridge, England, Vol. B.

6. Gordon, D. F., and M. A. Pedersen. 1986. "Comparison of Mode and Ray Theory Using Phase and Group Velocity." *Proceedings 12th International Congress on Acoustics*, Toronto, Canada, Vol. III H 3-6.

7. Pedersen, M. A., D. F. Gordon, and F. Hosmer. 1990. "Application of the Canonical Eigenvalue Method to an Underwater Acoustic Double Duct, Parts I and II." *J. Acoust. Soc. Am.* 885, 57(A).

# APPENDIX A: TAYLOR SERIES EXPRESSIONS ABOUT THE ASYMPTOTE INTERSECTIONS

In this appendix, we estimate the horizontal separation between mode eigenvalues at the point where the asymptotes intersect. This separation is of interest because it indicates the amount of coupling between the modes at the critical frequencies.

Let the eigenvalue equation be given as

$$G\,(x, y) = 0\;. \tag{A-1}$$

We expand G in a Taylor series about the intersection point $(x_o, y_o)$. We shall expand eq. A-1 for the case of $y = y_o$ so as to deal with a one-dimensional rather than a two-dimensional expansion. Equation A-1 is also a function of S, ρ, mode numbers, and boundary conditions, all of which are considered fixed and enter into the expansions as parameters. The first three terms of the expansion of eq. A-1 may be written as

$$G(x, y_o) = G(x_o, y_o) + (x - x_o)\ \delta G/\delta x + (x - x_o)^2 2^{-1} \delta^2 G/\delta x^2\;. \tag{A-2}$$

The roots of this quadratic expression set to zero may be written as

$$(x - x_o) = [-b \pm (b^2 - 4c)^{1/2}]/2 \tag{A-3}$$

where

$$b = 2(\delta G/\delta x)/(\delta^2 G/\delta x^2) \tag{A-4}$$

and

$$c = 2G(x_o, y_o)/(\delta^2 G/\delta x^2)\;. \tag{A-5}$$

The displacement between the roots is

$$x_2 - x_1 = (b^2 - 4c)^{1/2}\;. \tag{A-6}$$

Equation A-6 then is an approximation to the horizontal separation between the eigenvalues.

The next step is to derive expressions for $\delta^2 G/\delta x^2$. We differentiate eq. 29 for the free-rigid boundary with respect to x and with the use of Eqs. 35 nd 32 obtain

$$\delta^2 G_{15}/\delta x^2 = -\,[x + \zeta_{20}\rho^4(1-S)^2]G_{15} - 2\zeta_{20}\rho^2(1-S)G_{18} + \rho^4(1-S)^2 G_{17}\,. \tag{A-7}$$

To obtain the counterparts of eq. A-7 for other boundary conditions, we need the expression

$$\delta G_{18}/\delta x = xG_{17} - \rho^2(1-S)G_{16}\,. \tag{A-8}$$

We differentiate eq. 32 for the free-free boundary condition with respect to x and with the use of eqs. A-8 and 29 obtain

$$\delta^2 G_{17}/\delta x^2 = -\,[x + \zeta_{20}\rho^4(1-S)^2]G_{17} + 2\rho^2(1-S)G_{16}\,. \tag{A-9}$$

We differentiate eq. 35 for the rigid-rigid boundary condition with respect to x and with the use of eqs. 29 and A-8 obtain

$$\delta^2 G_{16}/\delta x^2 = G_{15} - [x + \zeta_{20}\rho^4(1-S)^2]G_{16} + 2x\zeta_{20}\rho^2(1-S)\,G_{17} + x\rho^4(1-S)^2 G_{18}\,. \tag{A-10}$$

We now evaluate the dominant term of the factors entering into the expansions of the eigenvalue equation. The largest term for large negative y is $G_4$. The smallest term is $G_1$. The terms $G_2$ and $G_3$ fall between and are of equal importance.

In the case of the free-rigid boundary condition $Ai(-xo) = 0$ and $Ai'(-S_{20}) = 0$. The dominant terms then become

$$G_{15}(x_o, y_o) = -\,Bi(-x)\,Bi'(-\zeta_{20})G_1 \tag{A-11}$$

$$\delta G_{15}/\delta x = -\,Ai'(-x)Bi'(-\zeta_{20})G_2 + \zeta_{20}\rho^2(1-S)Bi(-x)Ai(-\zeta_{20})G_3 \tag{A-12}$$

$$\delta^2 G_{15}/\delta x^2 = 2\zeta_{20}\rho^2(1-S)\,Ai'(-x)\,Ai(-\zeta_{20})\,G_4\,. \tag{A-13}$$

The counterparts of eqs. A-11 to A-13 for the free-free boundary conditions are:

$$G_{17}(x_o, y_o) = -\,Bi(-x)\,Bi(-\zeta_{10})\,G_1 \tag{A-14}$$

$$\delta G_{17}/\delta x = -\,Ai'(-x)Bi(-\zeta_{20})G_2 - \rho^2(1-S)Bi(-x)Ai'(-\zeta_{20})G_3 \tag{A-15}$$

and

$$\delta^2 G_{17}/\delta x^2 = -\,2\rho^2(1-S)\,Ai'(-x)\,Ai'(-\zeta_{20})G_4\,. \tag{A-16}$$

The counterparts of eqs. A-11 to A-13 for the rigid-rigid boundary conditions are

$$G_{16}(x_o, y_o) = -Bi'(-x)\ Bi'(-\zeta_{20})G_1 \tag{A-17}$$

$$\delta G_{16}/\delta x = xAi(-x)Bi'(-\zeta_{20})G_2 + \zeta_{20}\rho^2(1-S)Bi'(-x)Ai(-\zeta_{20})G_3 \tag{A-18}$$

and

$$\delta G_{16}/\delta x^2 = -2x\zeta_{20}\rho^2(1-S)\ Ai(-x)\ Ai(-\zeta_{20})G_4\ . \tag{A-19}$$

Next, consider the evaluation of eqs. A-4 and A-5 for the free-rigid boundary condition. The substitution of eqs. A-11 to A-13 leads to

$$b = -Bi'(-\zeta_{20})(G_2/G_4)/\zeta_{20}\rho^2(1-S)\ Ai(-\zeta_{20}) + Bi(-x)(G_3/G_4)Ai'(-x) \tag{A-20}$$

and

$$c = -Bi(-x)Bi'(-\zeta_{20})(G_1/G_4)/\zeta_{20}\rho^2(1-S)Ai'(-x)Ai(-\zeta_{20})\ . \tag{A-21}$$

We may eliminate the Bi and Bi′ functions in eqs. A-20 and A-21 by means of

$$Bi(-x) = -[\pi\, Ai'(-x)]^{-1} \tag{A-22}$$

and

$$Bi'(-\zeta_{20}) = -[\pi\, Ai(-\zeta_{20})]^{-1} \tag{A-23}$$

Equation A-22 and A-23 follow from the Wronskian evaluated at various zeros of the Airy functions. Equations 101 to 105 of the main text then follow from eq. A-20 to A-33.

For the free-free boundary condition, eqs. A-14 to A-16 lead to

$$b = -Bi'(-\zeta_{20})(G_2/G_4)/\rho^2(1-S)\ Ai'(-\zeta_{20}) + Bi(-x)(G_3/G_4)Ai'(-x) \tag{A-24}$$

and

$$c = -Bi(-x)Bi(-\zeta_{20})(G_1/G_4)/\rho^2(1-S)Ai'(-x)Ai(-\zeta_{20})\ . \tag{A-25}$$

Equations 118 and 109 of the main text then follow from eqs. A-22 to A-25.

For the rigid-rigid boundary condition eq. A-17 to A-19 lead to

$$b = -Bi'(-\zeta_{20})(G_2/G_4)/\zeta_{20}\rho^2(1-S)\ Ai(-\zeta_{20}) - Bi'(-x)(G_3/G_4)/xAi'(-x) \tag{A-26}$$

and

$$c = Bi'(-x)\, Bi'(-\zeta_{20})(G_1/G_4)/x\zeta_{20}\rho^2(1 - S)\, Ai'(-x)\, Ai(-\zeta_{20}) \,. \qquad \text{(A-27)}$$

Equations 111 and 112 of the main text then follow from eqs. A-26, A-27, A-22, and A-23.

# APPENDIX B: EXTENSION OF THE CANONICAL EIGENVALUE METHOD TO INCLUDE DISCONTINUITIES OF SOUND SPEED AND TO INCLUDE THE EFFECTS OF LAYERS WITH DIFFERENT CONSTANT DENSITIES

Reference B1 presents some recent work by Computer Sciences Corporation (CSC) under contract to NOSC, Code 541. Portions of this work deal with updating the canonical eigenvalue method so as to be able to treat models of bottom interaction which involve sound-speed discontinuities, layers with different densities, and the use of complex parameters to model attenuation in bottom sediments. Since there is no immediate plan to publish reference B1, it seemed advisable to include the new work on the canonical eigenvalue method here in the form of this appendix. Some of the models of bottom interaction involve double-duct propagation. However, the numerical evaluation of these cases will not be carried out.

## 1. MODIFICATIONS TO THE CANONICAL EIGENVALUE METHOD FOR SOUND-SPEED DISCONTINUITIES

To use the canonical eigenvalue method in the preparation of controls for subbottom propagation, it is necessary to modify the treatment of reference 1 to include discontinuities in the sound speed at layer interfaces. Let the sound speed at the bottom of layer i be given by $C_{i+10}$ and at the top of layer i+1 be given by $C_{i+1,1}$. When the sound speed is continuous at the interface between layer i and i+1,

$$C_{i+1,0} = C_{i+1,1} \ . \tag{B-1}$$

Our interest here is in the case where eq. B-1 does not apply. Each interface with a sound-speed discontinuity introduces one more parameter into the profile representation.

From eq. 4 of reference 1, we determine that

$$-a_i/a_{i+1} = (-\gamma_{i0}/\gamma_{i+1})^{1/3} C_{i+1,1}/C_{i+1,0} = \bar{\rho}_i \ . \tag{B-2}$$

The first of our new canonical profile parameters is $\bar{\rho}_i$ defined by eq. B-2. We note that when eq. B-1 holds,

$$\bar{\rho}_i = \rho_1 \ . \tag{B-3}$$

Our next step is to determine $\overline{M}_{i+1}$ and $\overline{N}_{i+1}$ in the counterpart of eq. 18 of reference 1. This counterpart is

$$\zeta_{1+1,0} = \overline{M}_{i+1}\,\zeta_{i1} + \overline{N}_{i+1}\,\zeta_{i0}\ . \tag{B-4}$$

We proceed in a similar manner to the development of eqs. 18 to 31 of reference 1. The counterparts of eqs. 30 and 31 become

$$\overline{N}_{i+1} = \overline{\rho}_i^{\,2}\,\overline{S}_{i+1} \tag{B-5}$$

and

$$\overline{M}_{i+1} = \rho_i^{\,2}\,(1 - \overline{S}_{i+1}) \tag{B-6}$$

where

$$\overline{S}_{i+1} = [(C_{i1}/C_{i+2,0})^2 - 1]/[(C_{i1}/C_{i+1,0})^2 - 1] \tag{B-7}$$

Equation B-7 is the counterpart of eq. 29 of reference 1 and represents the second of our new canonical profile parameters. When eq. B-1 applies, $\overline{N}_{i+1}$, $\overline{M}_{i+1}$, and $\overline{S}_{i+1}$ reduce respectively to $N_{i+1}$, $M_{i+1}$, and $S_{i+1}$, of reference 1. We note that eq. B-7 involves the sound speeds at the top and bottom of layer i and at the bottom of layer i+1.

Next, we must develop an expression for a third canonical profile parameter, which is necessary to account for the extra third profile parameter for a layer with sound-speed discontinuity. We assume that the Airy function argument at the top of layer i+1 may be written an a linear combination of the arguments at the top and bottom of layer i. Thus,

$$\zeta_{i+1,1} = \hat{M}_{i+1}\,\zeta_{i1} + N_{i+1}\,\zeta_{i0}\ . \tag{B-8}$$

Our task is to determine $\hat{M}_{i+1}$ and $\hat{N}_{i+1}$. We proceed in a manner similar to that of eqs. 18 to 31 of reference 1. It is straightforward to determine expressions for $\hat{M}_{i+1}$ and $\hat{N}_{i+1}$. However, an appropriate third canonical parameter was not all apparent from these original expressions. By analogy with eqs. B-5 and B-6 we assumed that the third parameter was $\hat{S}_{i+1}$ and that

$$\hat{N}_{i+1} = \overline{\rho}_i^{\,2}\,\hat{S}_{i+1} \tag{B-9}$$

and

$$\hat{M}_{i+1} = \rho_i^{\,2}\,(1 - \hat{S}_{i+1}) \tag{B-10}$$

We then used our original expressions for $\hat{N}_{i+1}$ or $\hat{M}_{i+1}$ to solve for $\hat{S}_{i+1}$ to obtain

$$\hat{S}_{i+1} = [(C_{i+1,0}/C_{i+1,1})^2[(C_{i+1,1}/C_{i+1})^2 - 1]/[C_{i+1,0}/C_{i1})^2 - 1] \ . \qquad \text{(B-11)}$$

This then is the third canonical profile parameter. When eq. B-1 applies, $\hat{S}_{i+1} = 1$, $\hat{M}_{i+1} = 0$, and $\hat{N}_{i+1} = i2$. Thus, eq. B-8 reduces to

$$\zeta_{i+1,1} = \rho_i{}^2 \zeta_{i0} \ ,$$

which is the result of eq. 10 of reference 1 for the continuous profile. We note that eq. B-11 involves the sound speeds at the top and bottom of layer i and at the top of layer i+1.

We note that the original expressions for $\hat{N}_{i+1}$ or $\hat{M}_{i+1}$ contained $\rho_i{}^2$, but not $\bar{\rho}_i{}^2$. The $(C_{i+1,0}/C_{1+1,1})^2$ factor was inserted in eq. B-11 so that $\bar{\rho}_i^2$ rather than $\rho_i^2$ appears in eqs. B-9 and B-10. This allowed us to define $\hat{S}_{i+1}$ such that $\hat{N}_{i+1}$ and $\hat{M}_{i+1}$ can be expressed as simple functions of the canonical parameters.

Equations B-4 and B-8 or their continuous counterparts allow us to determine all Airy function arguments as a linear function of x and y by a recursive process similar to that discussed in eqs. 32 to 39 of reference 1.

Consider a profile consisting of m boundaries, $n_1$ interfaces without discontinuity and $n_2$ interfaces with sound speed discontinuity. The total number of profile parameters is $2n_1 + 3n_2 + m + 1$ parameters. Here, we specify $n_1$ values of $\rho_i$, $n_1 + m - 2$ values of $S_{i+1}$, $n_2$ values of $\bar{\rho}_i{}^2$ and $n_2$ values each of $\bar{S}_{i+1}$ and $\hat{S}_{i+1}$ for a total of $2n_1 + 3n_2 + m - 2$ canonical parameters. If we then select $C_1$, $C_{20}$, and $\gamma_1$ we have the requisite number of parameters. These three profile parameters plus the set of canonical parameters can be used to generate the sound-speed profile.

Assume that the first interface with a discontinuous sound speed is at the bottom of layer i and that all parameters for layer 1 to the bottom of layer i have been generated by the recursive method of reference 1. The first step is to use the given value of $\hat{S}_{i+1}$, the known values of and $C_{i1}$ and $C_{i+1,0}$ to generate $C_{i+1,1}$ from eq. B-11. The second step is to use the given values of $\bar{\rho}_i$ and the known values of $\gamma_{10}$, $C_{i+1,1}$, and $C_{i+1,0}$ to generate $\gamma_{i+1}$ from eq. B-2. The third step is to use the given value of $\bar{S}_{i+1}$ and the known values of $C_{i1}$ and $C_{i+1,0}$ to generate $C_{i+2,0}$ from eq. B-7. The fourth step is to evaluate

$$\gamma_{i+1,0} = \gamma_{i+1} (C_{i+2,0}/C_{i+1,1})^3 \ . \qquad \text{(B-12)}$$

We now know all the requisite profile parameters down to the bottom of layer i+1. The four-step process is then repeated for each of the remaining profile layers to define the entire profile.

Thus far, our concern has been with the generation of the Airy functions arguments and the characterization of the sound-speed profile in terms of canonical parameters. Next, we examine how the eigenvalue equation and normalization process are affected by the sound-speed discontinuities. This is relatively simple. In most cases we only have to replace $\rho_i$ by $\bar{\rho}_i$. However, we do not replace $\rho_i^2$ by $\bar{\rho}_i^2$ in the Airy function arguments because we have already noted how these arguments change. For example, the eigenvalue equation is modified by replacing $\rho_i$ in eq. 22 of reference 2 with $\bar{\rho}_i$ at any interface where there are sound-speed discontinuities.

Before we examine the normalization process of reference 1, we correct several critical typographical errors in reference 1. The most important of these corrections is to replace $a_i^{-1}$ by $a_1^{-1}$ on the right side of eq. 92 and on the left side of eq. 96. In addition, the 6 in eq. 33 should be deleted.

A check of the normalization process of reference 1 demonstrates that we may replace $\rho_i$ by $\bar{\rho}_i$ in eqs. 78 to 80, and 91. We may also replace $\rho_j$ by $\bar{\rho}_j$ in eq. 93 and $\rho_i^2$by $\bar{\rho}_i^2$in eq. 96. However, since eq. 10 no longer applies we must replace eq. 97 by

$$D_{ni} = D\pi \left[(1 + \bar{\rho}_i^3)Fi'^2(-\zeta_{i0}) + (\zeta_{i0} + \bar{\rho}_i\zeta_{i+1})Fi^2(-\zeta_{i0})\right] . \qquad \text{(B-13)}$$

Equation B-13 differs from the $D_{ni}$ of eq. 97 of reference 1 in that eq. B-8 now holds and $\hat{S}_{i+1}$ cannot be expressed as a simple multiple of $\zeta_{i0}$. Similarly, in eqs. 79 and 90 of reference 1 the Airy function argument of $-\rho_i^2\,\zeta_{i0}$ must be replaced by $-\zeta_{i+1,1}$.

## 2. MODIFICATIONS TO THE CANONICAL EIGENVALUE METHOD FOR LAYERS WITH DIFFERENT CONSTANT DENSITIES

It is necessary to modify the treatment of reference 1 and the extensions of section 1 of this appendix to include the effect of a variable density. Let the density in layer i be given by $\hat{\rho}_i$. As discussed in reference B1, the treatment of variable density consists of three relatively simple statements. First, it is necessary that $\hat{\rho}\,U$ be continuous. Second, the normalization integrand of eq. 83 of reference 1 must include $\hat{\rho}$ as a multiplicative factor. Third, the propagation loss expression, i.e., eq. 2 of reference B2, contains an additional multiplicative factor of $\hat{\rho}_s\,\hat{\rho}_h$, where $\hat{\rho}_s$ and $\hat{\rho}_h$ is the density at the source and receiver respectively.

The treatment is facilitated by introducing the canonical parameter $\mu_i$ defined by

$$\mu_i = \hat{\rho}_i/\hat{\rho}_{i+1} . \qquad \text{(B-14)}$$

The introduction of density into the problem has no effect at all on the arguments of the Airy functions. Thus, the arguments remain those values given in reference 1 with the modifications for sound-speed discontinuities as discussed in section 1.

The eigenvalue formulation is modified by multiplying the top line of eq. 18 of reference 2 by $\mu_i$. Similarly, the right side of eq. 77 of reference 1 is multiplied by $\mu_i$. We note the continuity of dU/dZ remains unchanged as a boundary condition. Thus, eq. 22 of reference 2 and eq. 78 of reference 1 remain unchanged. As a consequence, the first product within the brackets of eqs. 79 and 80 of reference 1 are multiplied by $\mu_i$.

The treatment of the normalization, $D_n$, is somewhat more complicated. Equation 89 of reference 1 is replaced by

$$D_n = a_1{}^{-1} \mu_1 D_c \ . \tag{B-15}$$

Equation 93 of reference 1 is replaced by

$$D_{pi} = \prod_{j=1}^{i-1} \bar{\rho}_j \mu_j{}^{-1} ; \ D_{p1} = 1 \ . \tag{B-16}$$

Equations 94, 95, 98, and 99 of reference 1 apply without change with the understanding that $D_{pI}$ is evaluated from eq. B-16. The replacement for eq. B-13 or its reference 2 counterpart, eq. 97, is complicated by the change in the boundary condition in eq. 77 of reference 1. The end result is given by

$$D_{ni} = D_{pi}[(1 + \mu_i^{-1} \bar{\rho}_i{}^3) Fi'^2(-\zeta_{i0}) + (\zeta_{10} + \mu \bar{\rho}_i \zeta_{i+1,1}) Fi^2(-\zeta_{10})] \ . \tag{B-17}$$

We note that at interfaces with no sound-speed discontinuity eqs. B-16 and B-17 apply with $\bar{\rho}_i$ replaced by $\rho_i$.

## 3. COMMENTS ON COMPLEX EIGENVALUES

Pages 10 and 11 of reference 1 discuss some properties of the complex component of the Airy function arguments, which are of further interest. With more exposure to the profile layers with complex arguments, we conclude that the statements in the paragraph commencing near the bottom of page 10 are incorrect. In the case of a single-layer, positive-gradient half space with complex parameters and bounded above by a free or rigid surface the eigenvalues are real. However, this is not the case for multilayer profiles even with only one layer with complex parameters. If we define x and y as the top and bottom values for the layer with complex parameters, the major contribution to Im Cp may indeed be introduced by the complex parameters in eq. 17 of reference 1. However, complex profile parameters in one layer lead to complex canonical profile parameters which will, in turn, lead to complex eigenvalue solutions. Thus, the attenuation associated with unbounded profiles cannot be completely separated from that associated with complex profile parameters as was stated in reference 1.

Equations 59 to 62 of reference 1 present an analysis of the imaginary components of the Airy function arguments for real profile parameters. Next, we extend this analysis to profiles with discontinuities in the sound speed.

Consider that x and y are associated with a layer with real parameters. Then, from eq. 14 of reference 1 it follows that the requirement for a real frequency leads to

$$\mathrm{Im}\ x = \mathrm{Im}\ y. \tag{B-18}$$

Indeed, if the parameters involved in eqs. 7 and 8 of reference 1 are real, then Cp is the only complex term on the right side of eqs. 7 and 8 and it follows that

$$\mathrm{Im}\ \zeta_{i1} = \mathrm{Im}\,\zeta_{i0}\ . \tag{B-19}$$

Indeed, eq. B-19 holds for any layer with real parameters. This means that the imaginary part of the Airy function argument is the same at the upper and lower nterfaces of each layer.

From eqs. B-4 to B-6 and eq. B-19, it follows that

$$\mathrm{Im}\,\zeta_{i+1,0} = (\bar{M}_{i+1} + \bar{N}_{i+1})\ \mathrm{Im}\,\zeta_{i0} = \bar{\rho}_i{}^2\,\mathrm{Im}\,\zeta_{i0}\ . \tag{B-20}$$

Similarly, from eq. 97 to 99 and eq. B-19, it follows that

$$\mathrm{Im}\,\zeta_{i+1,1} = (\bar{M}_{i+1} + \bar{N}_{i+1})\ \mathrm{Im}\,\zeta_{i0} = \bar{\rho}_i{}^2\,\mathrm{Im}\,\zeta_{i0}\ . \tag{B-21}$$

Thus, as was the case for the continuous profile the imaginary component of the Airy function arguments only involves Im x and the set of $\bar{\rho}_i{}^2$.

Assume now that the parameters in layer 1 are real, but are complex in layer 2. Equations 93 and 97 may be written respectively as

$$\zeta_{20} = \bar{M}_2\ \mathrm{Re}\ x + \bar{N}_2\ \mathrm{Re}\ y + i\,\bar{\rho}_i{}^2\,\mathrm{Im}\ y\ . \tag{B-22}$$

and

$$\zeta_{21} = \bar{M}_2\ \mathrm{Re}\ x + \bar{N}_2\ \mathrm{Re}\ y + i\,\bar{\rho}_i{}^2\,\mathrm{Im}\ y\ . \tag{B-23}$$

In general, $\mathrm{Im}\,\bar{M}_2 \neq \mathrm{Im}\,\hat{M}_2$ and $\mathrm{Im}\,\bar{N}_2 \neq \mathrm{Im}\,\hat{N}_2$. Thus, $\mathrm{Im}\,\zeta_{20} \neq \mathrm{Im}\,\zeta_{21}$ and the complex component of the Airy function arguments will differ at the top and bottom of the layer. However, for the case of real sound speeds but complex gradients, $\bar{M}_2$, $\bar{N}_2$, $\hat{M}_2$, and $\hat{N}_2$ are all real and $\mathrm{Im}\,\zeta_{20} = \mathrm{Im}\,\zeta_{21}$.

## 4. SPECIFIC CANONICAL EXPRESSIONS FOR TWO-LAYER MODELS

This section gives the explicit expressions that are required to be evaluated for the canonical normal mode solution for two-layer models of bottom propagation. Figure B-1 is a schematic indicating the eight-profile parameters that define the environments. These are the four sound speeds, two gradients, and two constant values of density. The top boundary is a free surface and the lower boundary is a rigid surface. The parameter $C_{21}$, $C_{30}$, and $\gamma_2$ may be complex so as to model a lossy bottom layer.

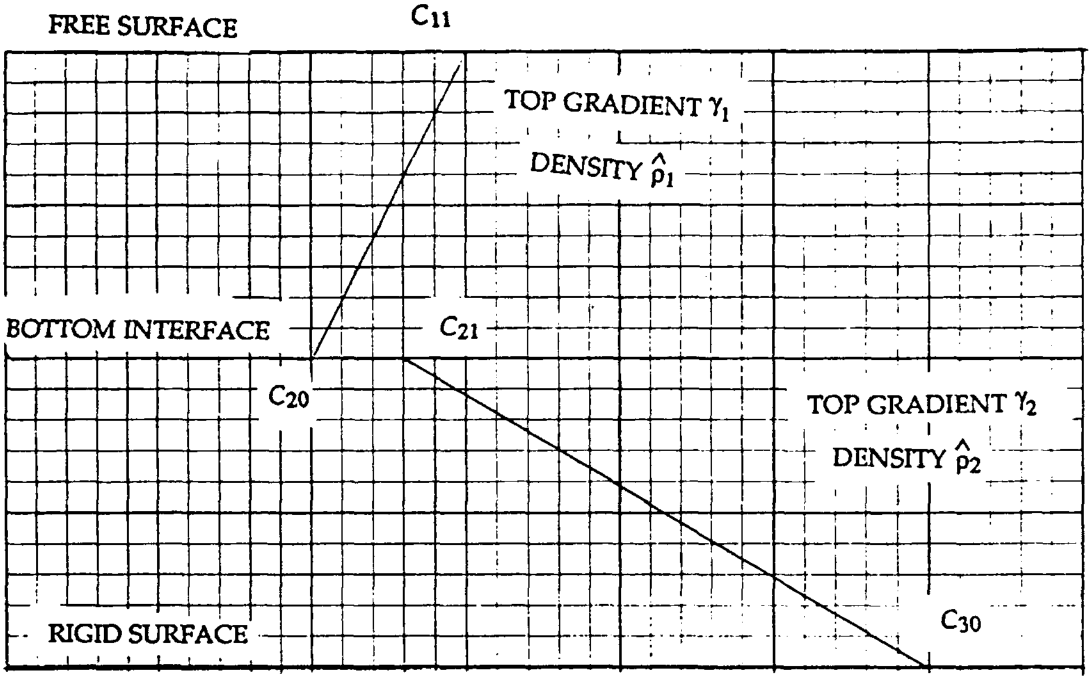

Figure B-1. Schematic of the generic two-layer profile model with a sound-speed discontinuity and piecewise constant densities.

The canonical parameters for this profile class are given by

$$\bar{\rho} = (-\gamma_1)/\gamma_2)^{1/3} C_{21}/C_{11} \tag{B-24}$$

$$\bar{S} = [(C_{11}/C_{30})^2 - 1]/(C_{11}/C_{20})^2 - 1 \tag{B-25}$$

$$\dot{S} = (C_{20}/C_{21})^2[(C_{21}/C_{11})^2 - 1]/[(C_{20}/C_{11})^2 - 1] \tag{B-26}$$

and

$$\mu = \bar{\rho}_1/\dot{\rho}_2 \, . \tag{B-27}$$

Since there is only one value each for these canonical parameters, we have deleted subscripts on the parameters to simplify the notation. Note that the eight-profile parameters reduce to four canonical parameters.

The eigenvalue equation is given by

$$\begin{vmatrix} \mathrm{Ai}(-x) & \mathrm{Bi}(-x) & 0 & 0 \\ \mu\,\mathrm{Ai}(-y) & \mu\,\mathrm{Bi}(-y) & -\mathrm{Ai}(-\zeta_{21}) & -\mathrm{Bi}(-\zeta_{21}) \\ \bar{\rho}\,\mathrm{Ai}(-y) & \bar{\rho}\,\mathrm{Bi}'(-y) & \mathrm{Ai}'(-\zeta_{21}) & \mathrm{Bi}'(-\zeta_{21}) \\ 0 & 0 & \mathrm{Ai}'(-\zeta_{20}) & \mathrm{Bi}'(-\zeta_{20}) \end{vmatrix} = 0 \qquad \text{(B-28)}$$

where

$$\zeta_{21} = \bar{\rho}^{\,2}(1 - \hat{S})x + \bar{\rho}^{\,2}\,\hat{S}\,y \qquad \text{(B-29)}$$

and

$$\zeta_{20} = \bar{\rho}^{\,2}(1 - \bar{S})x + \bar{\rho}^{\,2}\,\bar{S}\,y \qquad \text{(B-30)}$$

Equation B-28 follows from the boundary and interface condition of eqs. 18 to 24 of reference 2 with appropriate changes as previously discussed.

Now, the canonical expressions are already available here for a two-layer bounded profile with no sound-speed discontinuity and no treatment of density. Equation 8 may be obtained from eq. B-28 by the following simplifications

$$\bar{\rho} = \rho \qquad \text{(B-31)}$$

$$\mu = 1 \qquad \text{(B-32)}$$

and

$$\zeta_{21} = \rho^2\,y\,. \qquad \text{(B-33)}$$

Because of this similarity we were able to use the results of section 2B by updating to replace $\rho^2$ y by $\zeta_{21}$, by $\rho$, and $\bar{\rho}$ inserting $\mu$ where appropriate.

Following the treatment of section 2B for continuous profile, we introduce various sets of equations which facilitate the expansion of the matrix of eq. B-28 and its solution by Newton's method. The counterparts of eqs. 12 to 15 become

$$G_1 = \mu\, Ai(-y)Ai'(-\zeta_{21}) + \bar{\rho}\, Ai'(-y)Ai(-\zeta_{21}) \tag{B-34}$$

$$G_2 = \mu\, Bi(-y)Ai'(-\zeta_{21}) + \bar{\rho}\, Bi'(-y)Ai(-\zeta_{21}) \tag{B-35}$$

$$G_3 = \mu\, Ai(-y)Bi'(-\zeta_{21}) + \bar{\rho}\, Ai'(-y)Bi(-\zeta_{21}) \tag{B-36}$$

and

$$G_4 = \mu\, Bi(-y)Bi'(-\zeta_{21}) + \bar{\rho}\, Bi'(-y)Bi(-\zeta_{21} \,. \tag{B-37}$$

The counterparts of eqs. 20 to 23 are given by

$$G_{11} = Bi'(-\zeta_{20})\, G_2 - Ai'(-\zeta_{20})\, G_4 \tag{B-38}$$

$$G_{12} = Bi'(-\zeta_{20})\, G_1 - Ai'(-\zeta_{20})\, G_3 \tag{B-39}$$

$$G_{13} = Bi(-\zeta_{20})\, G_2 - Ai(-\zeta_{20})\, G_4 \tag{B-40}$$

and

$$G_{14} = Bi(\zeta_{20})\, G_1 - Ai(-\zeta_{20})\, G_3 \,. \tag{B-41}$$

The counterparts of eqs. 24 to 26 are given by

$$G_{15} = Ai(-x)\, G_{11} - Bi(-x)\, G_{12} \tag{B-42}$$

$$G_{16} = Ai'(-x)\, G_{11} - Bi'(-x)\, G_{12} \tag{B-43}$$

$$G_{17} = Ai(-x)\, G_{13} - Bi(-x)\, G_{14} \tag{B-44}$$

The eigenvalue equation for the free-rigid boundary of figure B-1 is given by eq. 28, i.e.,

$$G_{15} = 0 \,. \tag{B-45}$$

To solve eq. B-45 by Newton's method we need the partial derivatives with respect to y and with respect to x.

The first step in evaluating these partial derivatives is to evaluate the partial derivatives of eqs. B-34 to B-37. These derivatives are the counterparts of eqs. 16 to 19 and are given by

$$G_1' = -(\mu + \bar{\rho}^3 \hat{S})Ai'(-y)\, Ai'(-\zeta_{21}) + (\mu \bar{\rho}^2 \hat{S}\, \zeta_{21} + \bar{\rho}\, y)\, Ai(-y)\, Ai(-\zeta_{21}) \tag{B-46}$$

$$G_2' = -(\mu + \bar{\rho}^3 \hat{S})Bi'(-y)\, Ai'(-\zeta_{21}) + (\mu \bar{\rho}^2 \hat{S}\, \zeta_{21} + \bar{\rho}\, y)\, Bi(-y)\, Ai(-\zeta_{21}) \tag{B-47}$$

$$G_3 = -(\mu + \bar{\rho}^3 \hat{S})Ai'(-y)\, Bi'(-\zeta_{21}) + (\mu \bar{\rho}^2 \hat{S}\, \zeta_{21} + \bar{\rho}\, y)\, Ai(-y)\, Bi(-\zeta_{21}) \tag{B-48}$$

and

$$G_4' = -(\mu + \bar{\rho}^3 \hat{S}) Bi'(-y)\, Bi'(-\zeta_{21}) + (\mu \bar{\rho}^2 \hat{S} \zeta_{21} + \bar{\rho} y)\, Bi(-y)\, Bi(-\zeta_{21}) \tag{B-49}$$

The partial derivative with respect to y is the counterpart of eq. 30 and may be written as

$$\delta G_{15}/\delta y = G_{15'} + \zeta_{20} \bar{\rho}^2 \hat{S} \hat{G}_{17} \tag{B-50}$$

where $G_{15}'$ is $G_{15}$ with $G_1$, $G_2$, $G_3$, and $G_4$ replaced respectively by $G_1'$, $G_2'$, $G_3'$, and $G_4'$.

The partial derivative with respect to x involves the partial derivatives of $G_1$ and $G_4$ with respect to x. Hence, we determine that

$$\delta G_1/\delta x = -\bar{\rho}^2 (1 - \hat{S}) [\mu \zeta_{21}\, Ai(-y)\, Ai(-\zeta_{21}) + Ai'(-y)\, Ai'(-\zeta_{21})] \tag{B-51}$$

$$\delta G_2/\delta x = -\bar{\rho}^2 (1 - \hat{S}) [\mu \zeta_{21}\, Bi(-y)\, Ai(-\zeta_{21}) + Bi'(-y)\, Ai'(-\zeta_{21})] \tag{B-52}$$

$$\delta G_3/\delta x = -\bar{\rho}^2 (1 - \hat{S}) [\mu \zeta_{21}\, Ai(-y)\, Bi(-\zeta_{21}) + Ai'(-y)\, Bi'(-\zeta_{21})] \tag{B-53}$$

$$\delta G_4/\delta x = -\bar{\rho}^2 (1 - \hat{S}) [\mu \zeta_{21}\, Bi(-y)\, Bi(-\zeta_{21}) + Bi'(-y)\, Bi'(-\zeta_{21})] \tag{B-54}$$

The partial derivative with respect to x may be written as

$$\delta G_{15}/\delta y = -G_{16} + \zeta_{20} \bar{\rho}^2 (1 - S)\, G_{17} + \widetilde{G}_{15} \tag{B-55}$$

where $\widetilde{G}_{15}$ is $G_{15}$ with $G_1$, $G_2$, $G_3$, and $G_4$, replaced respectively by $\delta G_1/\delta x$, $\delta G_2/\delta x$, $\delta G_3/\delta x$, and $\delta G_4/\delta x$. We note that $G_{15}$ does not appear in eq. 29, the counterpart of eq. B-55. The reason is that eqs. 12–15 are independent of x and thus, eqs. B-51 to B-54 are all zero.

One may solve eq. B-45 by either selecting a fixed value of y and iterating to determine x by eq. B-55 or by selecting a fixed value of x and iterating to determine y by eq. B-50. Iteration on y or x then works best for the cases A or B modes respectively, as discussed for continuous sound speeds.

Iteration using finite differences rather than derivatives is possible. However, we do not recommend this approach as the eigenvalue curves often have rapid changes of slope. If a comprehensive analysis of many cases is to be made, then programming $\delta G_{15}/\delta x$ and $\delta G_{15}/\delta y$ will pay off in the long run.

We note that Fell Hosmer of NOSC Code 711 has developed a comprehensive computer program to determine eigenvalues for the two-layer continuous sound-speed profile. This program could readily be modified to accommodate the discontinuous sound-speed profile including density effects. For example, eqs. B-38 to B-44 are identical to those of the continuous profile. The only significant modification is to program eqs. B-51 to B-55 which do not appear in the continuous program.

We note also that the forms to be used for other boundary conditions appear in the forms for the free-rigid case. For example, $G_{17} = 0$ and $G_{16} = 0$ give the eigenvalue equation for the free-free and rigid-rigid boundaries and $G_{15}$ appears in some of the partial derivatives of $G_{17} = 0$ and $G_{16} = 0$. We will not give the free-free and rigid-rigid forms for the discontinuous profile, because these conditions are of an academic interest. We note; however, that the Hosmer program treats these boundary cases and could easily be modified to do so for the discontinuous profile model.

Assume now that the eigenvalues have been determined. The normalized mode depth functions are given by

$$U_n\,(Z_o)\,U_n\,(Z) = \hat{\rho}\,(Z_o)\;\hat{\rho}\,(Z)\,F_n\,(Z_o)\,F_n(\,Z)/D_n\;. \tag{B-56}$$

Here, n is the mode number, $Z_o$ is the source depth and Z is the receiver depth. Equation B-56 differs from eq. 20 of reference B2 in that eq. 20 does not include the density. Since the density is the same for all modes, reference B2 introduces the density as a multiplicative factor after the modes have been summed. The reason we chose to include the density in eq. B-56 is so that plots of the depth function will be continuous functions of depth. If the density is excluded in eq. B-56, then the depth functions will have a discontinuous jump at each layer interface.

The unnormalized eigenfunctions are given by

$$F_1(Z) = Bi(-x)\;Ai(-x-a_1\,Z)\;-\;Ai(-x)\;Bi(-x-a_1\,Z) \tag{B-57}$$

and

$$F_2(Z) = C_2\;Ai\;[-\zeta_{21}\;-\;a_2(Z-Z_2)]\;+\;D_2\;Bi\;[-\zeta_{21}\;-\;a_2(Z-Z_2)] \tag{B-58}$$

where

$$a_i = 2\pi^{2/3}\,f^{2/3}\,(-\zeta_i)^{1/3}/C_i\;. \tag{B-59}$$

For source (receiver) in layer 1, eq. B-57 and $\hat{\rho}_1$ are used in eq. B-56. For source (receiver) in layer 2, eq. B-58 and $\hat{\rho}_2$ are used in eq. B-56.

The form of eq. B-57 satisfies the boundary condition that $F_1\,(0) = 0$. Our remaining task is to give explicit computing forms for $C_2$, $D_2$, and $D_n$. Equations 77 to 79 apply without change.

The counterparts of eqs. 80 and 81 lead to

$$D_2 = -\pi\,[\mu\, F_1(-y)\, Bi'(-\zeta_{21}) \;-\; \bar{\rho}\, F_{1'}(-y)\, Bi(-\zeta_{21})] \qquad \text{(B-60)}$$

and

$$E_2 = -\pi\,[\mu\, F_1(-y)\, Ai'(-\zeta_{21}) \;-\; \bar{\rho}\, F_{1'}(-y)\, Bi(-\zeta_{21})] \qquad \text{(B-61)}$$

Equations 87 and 89 apply as is and the counterparts of eqs. 92 and 88 are given by

$$D_b = -\,\bar{\rho}\mu^{-1}\, \zeta_{20} F_2^{\,2}\,(-\zeta_{20}) \qquad \text{(B-62)}$$

and

$$D_{n1} = (1 + \mu^{-1}\,\bar{\rho}^{\,3}) F_i'^{\,2}(-y) \;+\; (y + \mu\,\bar{\rho}\,\zeta_{21})\, F_1^{\,2}\,(-y)\;. \qquad \text{(B-63)}$$

Equation B-63 follows from eq. B-17. Equations 84 and 85 apply with eq. 86 replaced by

$$J = C_1 |C_1^{\,2}\, C_2^{-2} \;-1|\; |2\gamma_1|^{-1}\;. \qquad \text{(B-64)}$$

## 5. EXAMPLES OF DOUBLE DUCT PROFILES

Figure B-2 presents schematics of four bottom-interaction profiles. Profiles 1 and 2 represent shallow water profiles with a negative gradient in the water column. Profiles 3 and 4 represent deep water profiles with a positive gradient in the water column. Profiles 1 and 3 represent a "fast" sand bottom layer. Profiles 2 and 4 represent a "slow" clay bottom.

Our interest here is confined to profiles 2 and 4 which are double ducts. A full treatment of these profiles represent a much more complicated problem than the examples of section 3. The canonical parameters $\rho$ and S are replaced by $\bar{\rho}$ and S, which are complex rather than real. Moreover there are two additional canonical parameters— $\dot{\rho}$ which is complex and $\mu$ which is real. Thus, the number of canonical constants involved in full treatment is seven as compared to two for the profiles of section 3.

We recommend a step wise approach using simpler profiles rather than a full-scale treatment of all seven constants. We would first isolate the effect of discontinuous sound speeds by letting the bottom parameters be real rather than complex and setting $\mu = 1$. This reduces the problem to three real constants $\bar{\rho}$, $\bar{S}$, and $\hat{S}$. A further simplification is to delete the rigid surface at the bottom of layer 2 and allow it to be

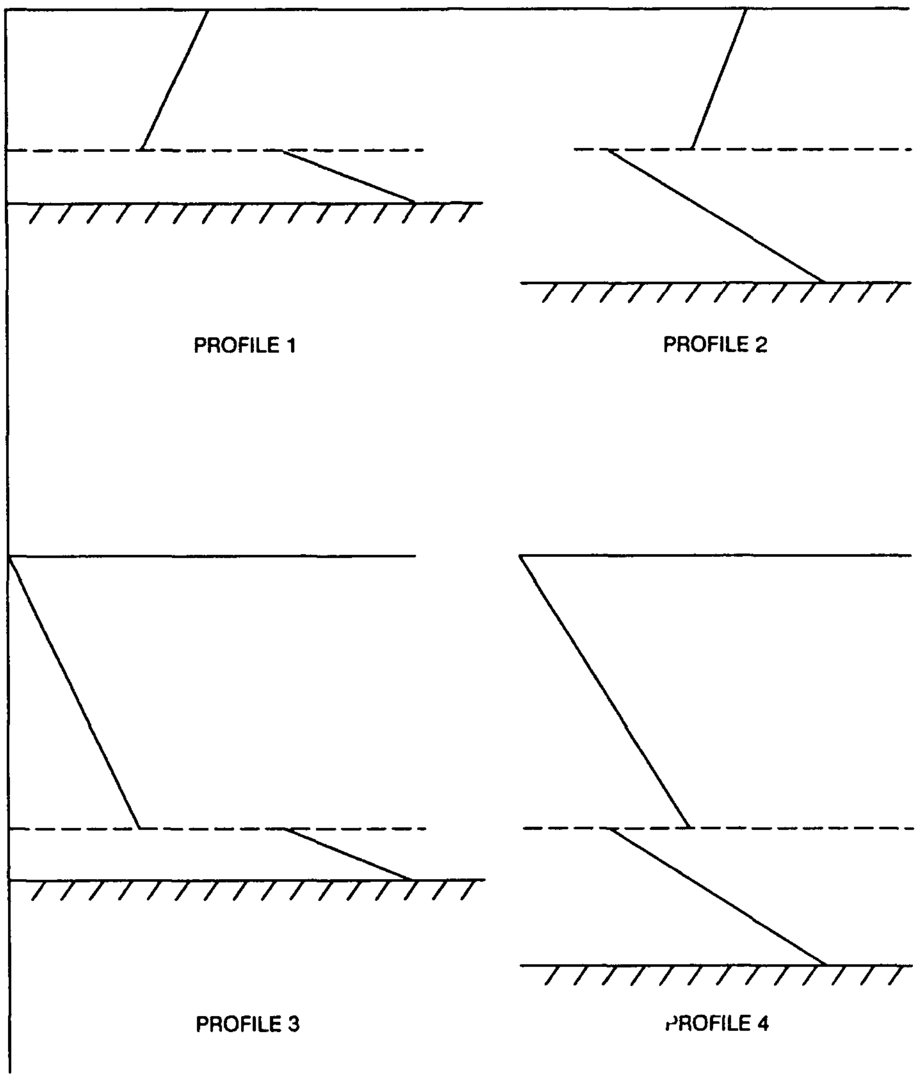

Figure B-2. Schematics of the four bottom-interaction profiles.

an infinite half space. This removes the canonical parameter $\hat{S}$ from the problem. Moreover, this reduces eq. B-28 from a 4×4 to a 3×3 matrix. We originally believed that case A of figure 1 represented the simplest double-duct configuration. However, the afore-mentioned simplifications of profiles 2 or 4 result in a simpler case than figure 1. Both cases contain two canonical parameters. However, the analysis of profiles 2 and 4 is easier because it only involves a 3×3 matrix. Thus, the characteristics of these double ducts may be simpler than presented here in section III.

## 6. ITERATIVE APPROACHES FOR COMPLEX EIGENVALUES

This section discusses an approach to the solution of the eigenvalue equation when the eigenvalues are complex.

In the discussion of eq. 60, reference 1 noted that there must be something about the mathematical form of the eigenvalue equation that leads to Im x = Im y. We determined this property from the physical condition that the frequency be real. Upon further thought we believe that this is not true about the eigenvalue equation, i.e., there are solutions for which Im x ≠ Im y. However, the approach to treating this problem is to impose the condition Im x = Im y as a constraint on the problem.

We arrived at this belief by considering the iteration process used to solve the eigenvalue equation. Suppose, for example, we have a problem that has complex eigenvalues. Suppose further we treat it by the same iterative process that we use for real eigenvlaues, i.e., we select a value of y (real) and use G and $\delta G/\delta x$ to iterate to the complex value of x. However, this solution will not be valid from a physical standpoint because the frequency would be complex. Similarly, if we arbitrarily picked y as a complex number, we would find complex values of x which satisfy the eigenvalue equation but they again would lead to complex frequency.

The trick to resolving this problem is to insert the constraint into the iteration process. Whenever we get a new estimate of Im, x, we always set Im y to this same estimate prior to evaluating G and $\delta G/\delta x$. Suppose that we already have a valid solution for some complex x and complex y and we wish to determine the solution for stepping to a new value of Re y. We estimate the new Re x, and new Im x = Im y based on the previous solution.

We then evaluate G and divide by $\delta G/\delta x$ to obtain the incremented value of Re x and Im x to add to the old estimate and obtain a new estimate of Re x and Im x. At this stage, there are two possible approaches. The simplest is to use this new estimate of Im x and set Im y to this estimate. A second and probably superior approach, is to set Im x = Im y equal to the average value of the last two estimates of Im x. This latter approach takes into account that the new estimate of Im x is predicated on the previous estimate of Im y. This newer estimate cannot be correct if we change Im y. Our guess is that the solution for Im x (and Im y) lies between previous Im x and the estimate of Im x for the current iteration.

We can anticipate this process will take somewhat longer to converge than for real eigenvalues because we are moving Im y at each iteration. However, we think that Re x and Re y are the dominant terms of the solution and that Im x and Im y are relatively small corrections. These assumptions may be wrong in some cases with the process failing to converge.

We are looking forward to a computer implementation for solving canonical eigenvalues when the solutions are complex. There are two outstanding questions to be answered. The first question is whether the iterative technique, which constrains Im x = Im y, will converge under usual circumstances. The second question is the nature of solutions for Im y $\neq$ Im x. For example, if we force Im y = 0, will we find a full suite of curves of real y versus complex x that correspond to modal solutions? Are there physical problems that may be represented by these solutions, or are the solutions merely an exercise in pure mathematics?

In closing, we note that we have illustrated the iteration process for a fixed y and the use of $\delta G/\delta x$ to determine x. A similar process is recommended for a fixed x and the use of $\delta G/\delta y$ to determine y. Here again, the trick is to constrain Im x = Im y during the iteration process regardless of whether we are iterating on x or on y.

# REFERENCES

B1. Pedersen, M. A. 1990. "Corrections to Gaussian-Beam Tracing for Various Boundary and Sub-Bottom Effects." report prepared by CSC for NOSC under Contract N66001-87-D-0074, Task 92 (Nov). San Diego, CA.

B2. Gordon, D. F. 1979. "Underwater Sound Propagation Loss Program," NOSC TR 393 (May). Naval Ocean Systems Center, San Diego, CA.

| | |
|---|---|
| **REPORT DOCUMENTATION PAGE** | *Form Approved*<br>*OMB No. 0704-0188* |

| | | |
|---|---|---|
| 1 AGENCY USE ONLY *(Leave blank)* | 2 REPORT DATE<br>July 1991 | 3 REPORT TYPE AND DATES COVERED<br>Sep 1988 – April 1991 |

| | |
|---|---|
| 4 TITLE AND SUBTITLE<br>THE APPLICATION OF CANONICAL EIGENVALUES TO TWO-LAYER, BOUNDED, UNDERWATER ACOUSTIC DUCTS | 5 FUNDING NUMBERS<br>PE: 0601152N<br>PROJ: R00N0<br>SUBPROJ: 71-ZW0901<br>ACC: DN309029 |
| 6 AUTHOR(S)<br>M. A. Pedersen, D. F. Gordon, F. Hosmer | |
| 7 PERFORMING ORGANIZATION NAME(S) AND ADDRESS(ES)<br>Naval Ocean Systems Center<br>San Diego, CA 92152-5000 | 8 PERFORMING ORGANIZATION REPORT NUMBER<br>NOSC TR 1428 |
| 9 SPONSORING/MONITORING AGENCY NAME(S) AND ADDRESS(ES)<br>Office of the Chief of Naval Research<br>Independent Research Programs (IR)<br>Arlington, VA 22217-5000 | 10 SPONSORING/MONITORING AGENCY REPORT NUMBER |

11 SUPPLEMENTARY NOTES

| | |
|---|---|
| 12a DISTRIBUTION/AVAILABILITY STATEMENT<br>Approved for public release; distribution is unlimited. | 12b DISTRIBUTION CODE |

13 ABSTRACT *(Maximum 200 words)*

This report applies the method of canonical eigenvalues to double-duct propagation of underwater acoustics. The class of all two-layer bounded profiles with free- or rigid-boundary conditions is treated. The canonical eigenvalue equation contains two parameters. (The conventional approach has six parameters.) Eigenvalue solutions are presented for 23 sets of parameters and boundary conditions. These solutions can be applied to any equivalent wave problem in any discipline of physics. Physical results are presented for six sound-speed profiles. These include plots versus frequency of phase velocity, group velocity, and eigenfunction normalization coefficients. Eleven examples of eigenfunctions (standing waves) are presented. At the critical frequencies of maximum coupling between ducts, the phase velocities of adjacent modes are pinched toward each other, the group velocity and eigenvalue normalization curves for adjacent modes cross each other, and the eigenfunction amplitudes of adjacent modes strongly resemble each other. The report develops an unexpected example in which two radically different profiles have identical plots of phase and group velocity as a function of frequency. Special configurations, predicted by ray theory as degenerate, do not lead to degenerate eigenvalues. The theory is extended to treat sound-speed discontinuities and layers of different constant density.

| | |
|---|---|
| 14 SUBJECT TERMS<br>underwater acoustics, sound propagation, eigenvalues, group velocity, duct coupling, normal mode theory | 15 NUMBER OF PAGES<br>125 |
| | 16 PRICE CODE |

| | | | |
|---|---|---|---|
| 17 SECURITY CLASSIFICATION OF REPORT | 18 SECURITY CLASSIFICATION OF THIS PAGE | 19 SECURITY CLASSIFICATION OF ABSTRACT | 20 LIMITATION OF ABSTRACT |
| UNCLASSIFIED | UNCLASSIFIED | UNCLASSIFIED | SAME AS REPORT |

UNCLASSIFIED

| | | |
|---|---|---|
| 21a. NAME OF RESPONSIBLE INDIVIDUAL<br>F. Hosmer | 21b. TELEPHONE *(Include Area Code)*<br>(619) 553-1456 | 21c. OFFICE SYMBOL<br>Code 711 |

NSN 7540-01-280-5500

Standard form 298

UNCLASSIFIED